Engineering Efficient Type-Sorted Carbon Nanotube Photovoltaics

By

Matthew John Shea

A dissertation submitted in partial fulfillment

of the requirements for the degree of

Doctor of Philosophy

(Materials Science)

at the

UNIVERSITY OF WISCONSIN-MADISON

2017

Date of final oral examination: 8 December 2017

The dissertation is approved by the following members of the Final Oral Committee:

Michael Arnold, Professor, Materials Science & Engineering
Padma Gopalan, Professor, Materials Science & Engineering
Dane Morgan, Professor, Materials Science & Engineering
Victor Brar, Assistant Professor, Physics
JR Schmidt, Associate Professor, Chemistry

“Research is what I’m doing when I don’t know what I’m doing.”

-Wernher Von Braun

…

To my parents, for encouraging me never to be satisfied with a poor answer to a big question.

To Mike, for pushing me out of my comfort zone, and into a wider world.

To my labmates at Wisconsin, for accompanying me on this grand journey.

To Erica, for understanding in the bad times, and celebrating in the good.

…

To never knowing exactly what you’re doing

ABSTRACT

Single-walled carbon nanotubes (SWCNTs) are an intriguing photoabsorbing material for photodetectors and photovoltaics due to their strong optical absorptivity, fast charge transport, solution processability, and chemical stability. However, isolating electronically pure semiconducing (s-) SWCNTs from as-synthesized mixtures of metallic (m-) and s-SWCNTs remains a challenge. Over the last decade, a class of polymers known as polyfluorenes has been shown to selectively wrap s-SWCNTs in organic solvents like toluene, allowing them to be isolated in solution at purities exceeding 99.98%. This simple, scalable, and efficient one-step separation has led to breakthroughs in both fundamental physics and the performance of s-SWCNT photovoltaics (PVs). s-SWCNTs are excitonic absorbers, and photoexcited excitons must be dissociated at a type-II heterojunction for efficient energy conversion. While exciton energy transfer along the axis of the nanotube is very fast, diffusion in the radial direction is orders of magnitude slower. Due to the poor out-of-plane exciton diffusion and the strength of their absorption bands, s-SWCNT films for PVs are typically very thin, often less than 10 nm. In this regime, optical interference plays an important role in determining device efficiency. Through modeling, I identify the optical spacing necessary to optimize device efficiency, and fabricate devices with >1% power conversion efficiency for AM1.5G broadband illumination, and >7% for near-infrared laser illumination. By studying s-SWCNT PV device characteristics at low temperature, I obtain information about the recombination in s-SWCNT/C_{60} PVs, and measure the offset energy between the donor s-SWCNT highest occupied molecular orbital and the fullerene-C_{60} acceptor lowest unoccupied molecular orbital, which sets the maximum open circuit voltage in these devices. The outstanding challenge of poor power conversion efficiency in all s-SWCNT PVs to date is attributed to poor exciton energy transfer within s-SWCNT films. I study the role of defects and length on limiting device efficiency, and pairing with modeling, suggest nanotube length and defect concentration regimes for improved device performance. Finally, using less harsh separation techniques, I isolate s-SWCNTs with lower defect density to fabricate PVs with improved photovoltaic efficiency.

TABLE OF CONTENTS

CHAPTER 1: Semiconducting Carbon Nanotubes for Photovoltaics 1

Structure and Electronic Type. 1

van Hove Singularities and s-SWCNT Optical Properties. 3

Metallic Nanotubes and Electronic Type Separations. 5

s-SWCNT Photovoltaic Cells. 6

CHAPTER 2: Binding Configuration and Coverage of PFO on Carbon Nanotubes 9

s-SWCNT Sorting. 9

Energy Transfer and PFO Coverage. 10

Binding Configuration via PL Anisotropy. 18

Supporting Information 22

CHAPTER 3: 1% Solar Cells Derived from Ultrathin Carbon Nanotube Photoabsorbing Films 33

Carbon Nanotube Photovoltaics 33

Device Fabrication and Evaluation 34

Supporting Information 41

CHAPTER 4: Energy Offset and Trap-Limited Recombination at the Carbon Nanotube/C_{60} Heterojunction 47

Measurements at Cryogenic Temperature 47

External QE at Low Temperature 49

Generation, Recombination, and Current-Voltage Curves 52

Ideality Factor and Trap-Limited Recombination 57

Energy Offset at the s-SWCNT/C_{60} Heterointerface 59

Supporting Information 63

CHAPTER 5: The Role of Defects as Exciton Quenching Sites in Carbon Nanotube Photovoltaics 68

Exciton Diffusion and the Limits of Quantum Efficiency 68

Linking Defect Density and Device Performance 70

Diffusion limited contact quenching Monte Carlo model. 77

Supporting Information 80

CHAPTER 6: Improving Photovoltaic Performance by Avoiding Harsh Sonication 86

Sonication Effects on Nanotube Length 86

Length Effects on s-SWCNT EQE 88

Optical Methods to Quantify Defect Density 90

Length Effects on PV Performance 93

Supporting Information 96

APPENDIX A: Monochromator 102

SECTION A1. Hardware *102*

SECTION A2. Software *103*

SECTION A3. Measurement Methods *103*

APPENDIX B: Peak Fitting and Concentration **106**

APPENDIX C: Photoluminescence **107**

APPENDIX D: JV Characteristics and Solar Simulator **109**

SECTION D1. Measuring JV Characteristics *109*

SECTION D2. Solar Simulator *109*

APPENDIX E: Cryostat **110**

APPENDIX F: MATLAB Programs **111**

References **112**

TABLE OF FIGURES

1-1 Physical structure, E(k) dispersion, and density of states of carbon nanotubes **3**

1-2 Optical absorption and photoluminescence **4**

1-3 Photovoltaic cell structure and current-voltage curve **7**

2-1 Absorption, concentration, and photoluminescence as a function of PFO concentration **13**

2-2 Excitation cross section and PFO coverage **14**

2-3 PL anisotropy and wrapping angle **20**

2-S1 PL map and optical absorbance of non-sorted SWCNTs **23**

2-S2 Individual PL intensity for three chiralities of HiPCO s-SWCNT **25**

2-S3 Zoom of PLE map showing emergence of new chiralities at high concentration **25**

2-S4 Energy transfer between chiral species as a function of concentration **26**

2-S5 Calculated PL intensity as a function of bundle size **26**

2-S6 Comparison of PL intensity with calculated S_{33} peak **27**

2-S7 Change in optical density versus time for different chiralities **29**

2-S8 Relative mass loading on (7,5), (7,6) and (8,6) prior to normalization **30**

2-S9 Wrapping angle from PL anisotropy **32**

3-1 Absorption and photoluminescence of nearly monochiral (7,5) s-SWCNTs **35**

3-2 External QE modulated by C_{60} thickness **37**

3-3 External QE and power conversion efficiency **38**

3-S1 External QE compared to optical intensity calculated from model **43**

3-S2 Nanotube-contributed current density for this work **44**

3-S3 Nanotube-contributed current density for other works **45**

3-S4 Comparison of simulated to AM1.5G spectra **46**

4-1 SEM and device structure of cryogenic PVs **49**

4-2 Low temperature EQE and peak shape **50**

4-3 Low temperature JV curves and extracted parameters **57**

4-4 Open-circuit voltage and ΔE_{HL} **61**

4-S1 External QE of ITO/C_{60} PV cell **63**

4-S2 Absorbance of s-SWCNT films at low temperature **64**

4-S3 Fitting of single diode and multiple diode *JV* characteristics **64**

4-S4 SEM and absorbance of thick (>20 nm) s-SWCNT films **65**

4-S5 Fitted *JV* curves compared to shunt resistance **65**

4-S6 *JV* curves of ITO/C_{60} devices in the dark **66**

4-S7 *JV* curves from ITO/C_{60}, thick, and thin s-SWCNT/C_{60} devices in the dark **66**

4-S8 Open-circuit voltage of three device stacks under illumination **67**

4-S9 Open-circuit voltage as a function of current density for thick and thin s-SWCNTs **67**

5-1 Length distribution and defect adding model **70**

5-2 Raman as a function of defect density **72**

5-3 Transient absorbance as a function of defect density **73**

5-4 Attenuation of optical absorbance in high defect density samples **74**

5-5 External QE as a function of defect density **76**

5-6 Outputs of Monte Carlo model and exciton harvesting length **79**

6-1 Length distribution and optical absorbance spectra **88**

6-2 EQE as a function of s-SWCNT ensemble **90**

6-3 Transient absorbance and PL **93**

6-4 Fill factor and open-circuit voltage as a function of length **95**

6-S1 Absorbance of PFO-BPy in s-SWCNT films **99**

6-S2 Modelled Peak EQE versus defect density **99**

6-S3 Raman spectra of three s-SWCNT ensembles **100**

6-S4 PL spectrum with fit peaks **100**

6-S5 Spectral power density of NIR broadband used to excite s-SWCNTs **101**

6-S6 *JV* curves for devices from three ensembles under illumination **101**

A1 Monochromator hardware setup **102**

E1 Cryostat PCB pinout arrangement **110**

CHAPTER 1: SEMICONDUCTING CARBON NANOTUBES FOR PHOTOVOLTAICS

STRUCTURE AND ELECTRONIC TYPE

Single-walled carbon nanotubes (SWCNTs) are atomically thin cylinders of sp2 carbon atoms a few nanometers across, and have been the focus of intense study since their discovery in 1993.[1] SWCNTs are a significant electronic material of interest due to their high tensile strength,[2] impressive high temperature and chemical resistance,[3] alongside their astounding electronic and optoelectronic properties, including high charge transport mobility,[4] strong optical absorptivity,[5] and size-dependent band gaps.[6] Further, SWCNTs are solution-processable,[7] enabling a wide range of fabrication methods and product applications.

Carbon nanotubes are a stunning example of the relationship between a material's physical structure and its electronic and optical properties. They may be described conceptually, and mathematically, as rolled-up cylinders of graphene. (**Figure 1-1A**) Graphene is a sheet of atomically thin sp2-bonded carbon, containing two atoms, located at (0,0) and (a_{cc},0) as its basis. The real-space basis vectors $\overrightarrow{a_1}$ and $\overrightarrow{a_2}$ are

$$\overrightarrow{a_1} = a_{CC}\left(\frac{3}{2}\hat{x} + \frac{\sqrt{3}}{2}\hat{y}\right) \quad \textbf{[1-1a]}$$

$$\overrightarrow{a_2} = a_{CC}\left(\frac{3}{2}\hat{x} - \frac{\sqrt{3}}{2}\hat{y}\right) \quad \textbf{[1-1b]}$$

where $\hat{x}$ and $\hat{y}$ are the unit vectors in the x- and y-directions of the coordinate plane, and a_{CC} is the carbon-carbon distance (1.42Å). The SWCNT structure is described by the rolling, or circumferential vector, $\overrightarrow{C_h}$, which connects the two carbon atoms that are overlaid to form the circumference of the nanotube, and the chiral angle, θ:

$$\overrightarrow{C_h} = n\overrightarrow{a_1} + m\overrightarrow{a_2} \quad \textbf{[1-2]}$$

$$\theta = \cos^{-1}\left(\frac{2n+m}{2\sqrt{n^2+nm+m^2}}\right) \quad \textbf{[1-3]}$$

The chiral angle ranges from 0° ($m = 0$), "zigzag," to 30° ($n = m$), "armchair". Individual chiralities of SWCNTs are designated by their (n, m) index, containing all the structural information about the nanotube. The translation vector $\vec{T}$ is perpendicular to the circumferential vector, and points along the axis of the nanotube:

$$\vec{T} = \left(\frac{2m+n}{d_R}\right)\overrightarrow{a_1} - \left(\frac{2n+m}{d_R}\right)\overrightarrow{a_2} \quad \textbf{[1-4]}$$

where d_R is the greatest common divisor of $2n + m$ and $2m + n$. Finally, the number of atoms in the unit cell of an (n, m) nanotube may be calculated:

$$N_C = \frac{4(n^2+nm+m^2)}{d_R}. \quad \textbf{[1-5]}$$

The electronic band structure of SWCNTs is also dependent on that of graphene. Graphene is notable for its unique band dispersion, in which, at six symmetric points in the first Brouillin zone, the valence and conduction bands touch at a single wavevector, known as K-points. Graphene is therefore a semimetal, and the cone-shaped dispersions are dubbed Dirac cones. Because the curvature of the bands is zero, the effective mass of both electrons and holes is zero. Carbon nanotubes represent further confinement of electrons, in which only certain wavevectors are allowed in the circumferential direction. If these wavevectors cross the K-points in the graphene first Brouillin zone, the resulting SWCNT is metallic. If not, the nanotube is semiconducting. **Figure 1-1B** contains an illustration of the first Brouillin zone of graphene, with allowed wavevectors in a (7,5) carbon nanotube overlaid for illustration. Since none of the wavevectors cross the K-points, the (7,5) nanotube is semiconducting. In general, a nanotube is metallic if and only if $n - m$ is a multiple of 3; otherwise it is semiconducting. Thus, 2/3 of all SWCNTs are semiconducting, while 1/3 are metallic.

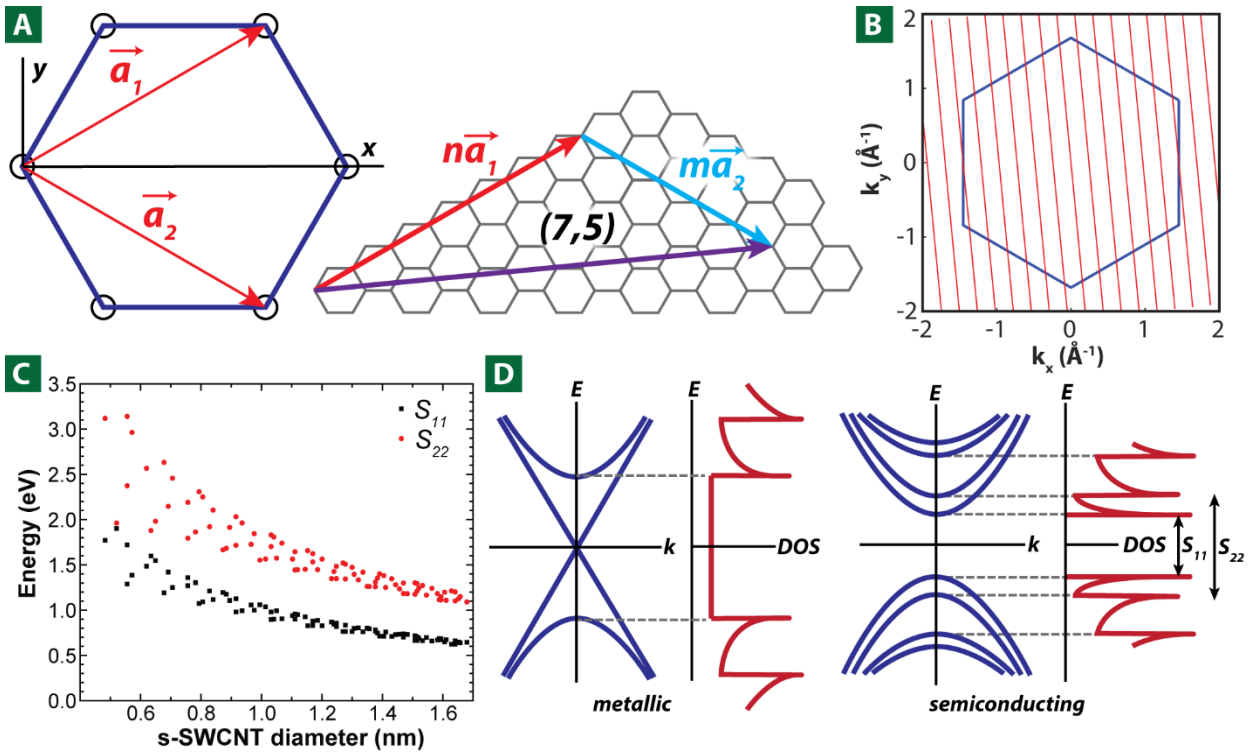

Figure 1-1. (A) Real-space basis vectors $\vec{a_1}$ and $\vec{a_2}$ comprise a unit cell of graphene. SWCNTs are generated by defining a rolling vector (purple) defined by an (n,m) index pair. **(B)** The 1st Brillouin zone of graphene is overlaid by allowed wavevectors (red) for a (7,5) nanotube. Since these wavevectors do not intersect with the corners of the 1st Brillouin zone, the (7,5) nanotube is semiconducting. **(C)** The gap energies (black) of s-SWCNTs[6] are presented as a function of diameter, along with second transition energies (red). **(D)** A schematic of the band structure (blue) and densities of state (red) for metallic and semiconducting SWCNTS. The first two s-SWCNT optical transitions, S_{11} and S_{22}, are shown.

VAN HOVE SINGULARITIES AND S-SWCNT OPTICAL PROPERTIES

Since the electron wavefunction in s-SWCNTs is confined around the circumference, as in particle-in-a-box energy levels, small diameters more strongly confine the electron, and raise energy levels. The result is a bandgap that depends inversely on diameter; small diameter nanotubes have larger bandgaps, and vice versa**. Figure 1-1C** displays a plot of s-SWCNT bandgap as a function of diameter. The s-SWCNT species useful for solar applications have band gaps around 1 eV and diameters near 1 nm. Due to quantum confinement in the circumferential direction, carbon nanotubes are one-dimensional materials containing characteristic van Hove singularities in their densities of state (**Figure 1-1D**). A s-SWCNT has multiple pairs of van Hove singularities, and it is electronic transitions between these states that dominate the optical

properties of the material. The first pair of van Hove singularities are denoted S_{11}, the second, S_{22}, and so on. A typical optical absorbance spectrum of a (7,5) carbon nanotube solution is presented in **Figure 1-2A**. Evident are sharp absorption lines near 1050 nm (S_{11}) and 655 nm (S_{22}). Absorption is dominated by S_{ii} transitions; other electronic transitions like S_{12}, S_{21}, etc. are much weaker, because they do not conserve angular momentum.[8] In addition, phonon-mediated absorption side bands,[9] denoted as $S_{ii}+X$ in **Figure 1-2A**, are evident near 900 nm. m-SWCNTs also absorb (M_{11}) though their absorption lines are weaker and broader, and are typically in the 450-550 nm range for m-SWCNTs with diameters of ~1.0 nm. The presence of m-SWCNT absorption peaks may be used to estimate the relative semiconducting purity of an ensemble, though due to their weak, broad peaks, this technique is limited to measuring m-SWCNT fractions of a few percent.[10-11]

Excitation of s-SWCNTs at any of their optical transitions produces an excited state that can recombine radiatively, releasing a photon of energy S_{11},[12-13] in a process known as photoluminescence (PL). Since each nanotube (n,m) has a unique (S_{11}, S_{22}) pair, varying excitation wavelength and observing emission over a wavelength range that encompasses S_{11} transitions produces a "map" with hot spots corresponding to individual (n,m) chiral indices. An example PL map is shown in **Figure 1-2B**. Photoluminescence is an important tool to use for characterizing solutions and films of s-SWCNTs, and will be explored in greater depth in **Chapter 2**.

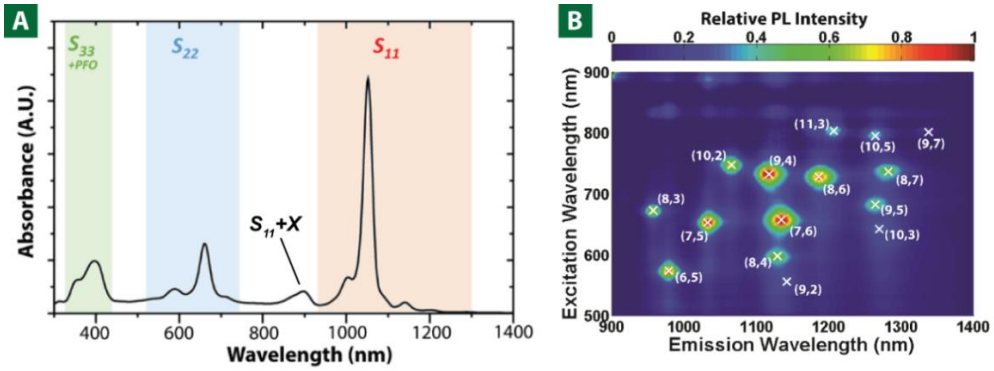

Figure 1-2. **(A)** Optical absorption spectrum of a majority (7,5) s-SWCNT solution in toluene.[14] The S_{11}, $S_{11}+X$, S_{22}, and S_{33} transitions are evident at 1055 nm, 655 nm, and 340 nm, respectively. The peak near 400 nm is from the polymer (PFO-See **Chapter 2**) used to isolate the sample. **(B)** Photoluminescence map of a different solution containing 15 species of nanotubes dispersed using sodium cholate in water. Peaks appear at the unique points (S_{11}, S_{22}) for each nanotube species present.

METALLIC NANOTUBES AND ELECTRONIC TYPE SEPARATIONS

To be incorporated into an electronic or optoelectronic device, a SWCNT ensemble must have high electronic type purity. Spurious metallic SWCNTs cause poor on/off ratios in transistors,[11] and quench excited states in photovoltaics.[15] Therefore, it is vital to separate s-SWCNTs from as-produced mixtures of s- and m-SWCNTs. This challenge is not at all a trivial one; as discussed, the electronic type of s-SWCNTs is only distinguishable by the specific (n,m) chiral index of the nanotube. s- and m-SWCNTs exist in all diameter ranges, and in nearly all chiral angles. Several approaches have been developed to solve this pressing problem. One approach for s-SWCNT transistor fabrication has nanotubes of both electronic types deposited as the channel. Then, the s-SWCNTs are gated "off" and current is forced through the m-SWCNTs, burning them out, leaving only s-SWCNTs crossing the channel.[16-17] However, this method is produces non-uniform arrays, since the location of m-SWCNTs is random. It is also limited to transistor applications, though recently a carbon nanotube computer was realized utilizing this burn-out technique.[16] On the other hand, solution-phase techniques allow control over the electronic type purity prior to deposition. Unfortunately, bare SWCNTs exhibit very low solubility in nearly all solvent systems. One approach to increase solubility is the covalent functionalization of the nanotube sidewalls with solubilizing groups.[18-19] However, this approach disrupts the sp2 character of the s-SWCNT sidewall, decreasing the optical absorption,[20] excited state lifetime,[21] and charge carrier mobility,[22] all of which are vital for photovoltaic applications. Non-covalent functionalization using surfactants in water,[23-24] and polymers in organic solvents,[7, 25] are therefore the focus of much of the current research. A remarkable opportunity is afforded by select non-covalent functionalized systems in which surface coverage or chemistry vary subtly from chirality to chirality, allowing separation of functionalized SWCNTs by chirality or electronic type.[26-28] Specifically, a family of polymers known as polyfluorenes selectively wrap and solubilize s-SWCNTs in organic solvents like toluene.[7, 29-30] These polymers are vital to the large-scale separation of s-SWCNTs that is photovoltaic application-enabling, and will be discussed in further detail in **Chapter 2**.

s-SWCNT Photovoltaic Cells

The dramatic increase in solar power generation in the United States and worldwide over the past decade has been driven by a significant increase in photovoltaic cell production capacity and a steadily decreasing price-point for installed photovoltaics.[31] While power generation is and will continue to be dominated by inorganic materials like amorphous and crystalline silicon, gallium arsenide, and cadmium telluride, for niche applications organic and other emerging photovoltaics may provide particular benefits that inorganic materials cannot. Carbon nanotubes occupy a unique position among photovoltaic materials; like inorganics, they are thermally and chemically stable,[3] and like organic materials they are strong absorbers[32] and may be solution-cast. Their especially strong absorption at the S_{ii} transitions make them attractive for single-wavelength photodetector and beamed power applications. Regardless of the specific application, s-SWCNT photovoltaic cells operate as a type-II heterojunction, usually incorporating an electron acceptor like fullerene-C_{60}. A schematic of the physical structure and of a s-SWCNT/C_{60} type-II heterojunction is given in **Figure 1-3A**, respectively. Like in many organic materials, an absorbed photon in an s-SWCNT generates a bound electron-hole pair, or exciton, with binding energy $E_B > k_B T$.[33] The photogenerated exciton must diffuse to the heterointerface to be dissociated into its constituent hole, which remains in the s-SWCNT film, and electron, which transfers into the electron acceptor. Bindl et al. showed that exciton dissociation at the s-SWCNT/C_{60} interface is extremely efficient, approaching 100%.[34] However, exciton diffusion to the heterointerface is very slow, limiting the thickness of s-SWCNT photoabsorbing film to a few diffusion lengths, typically <10 nm. Once the exciton is dissociated, however, the electron and hole are extracted under short circuit conditions as current (short-circuit current, I_{SC}) , or remain separated at open circuit conditions, developing a voltage (open-circuit voltage, V_{OC}). An example current-voltage curve is shown in **Figure 1-3B**.

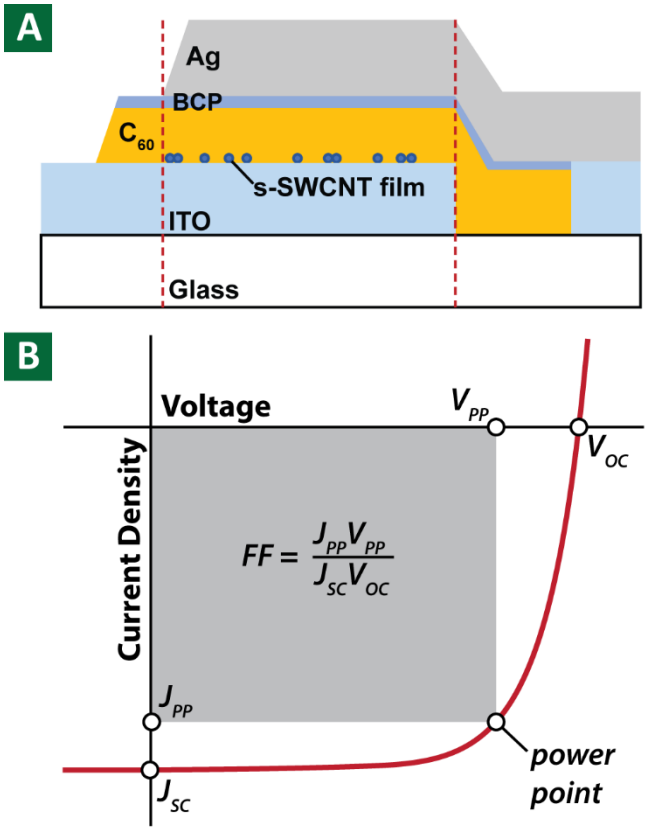

Figure 1-3. (A) A schematic of a s-SWCNT/C60 heterojunction photovoltaic device. The device area is defined by the overlap between the top electrode (Ag) and the bottom electrode (ITO). **(B)** An illustration of a current density – voltage curve of a device under illumination. The fill factor, FF, current density at short circuit (JSC), and open-circuit voltage (VOC) are denoted.

In a photovoltaic cell, the power output is the maximum of the product IV, which occurs at the power point. The ratio of the power at the power point and the product $I_{SC}V_{OC}$ is known as the fill factor, FF. The power conversion efficiency, η_P, is then expressed by

$$\eta_P = \frac{I_{SC}V_{OC}FF}{P_{in}}, \qquad [\mathbf{1\text{-}6}]$$

where P_{in} is the incident optical power. Often, the current is expressed as an area density, the short-circuit current density, J_{SC}. The J_{SC} is the integral of the product of the number of photons impinging on the device, Φ, at wavelength λ, and the external quantum efficiency, EQE, at that wavelength:

$$J_{SC} = \int \Phi(\lambda)\, EQE(\lambda)\, d\lambda. \quad \textbf{[1-6]}$$

Usually, $\Phi(\lambda)$ is taken as the solar spectrum, but for non-solar photovoltaic applications, $\Phi(\lambda)$ can in principle be any spectral distribution. Maximizing the current density, then, requires maximizing the EQE, itself a function of several sub-efficiencies.

$$EQE = \eta_{abs}\eta_{diff}\eta_{diss}\eta_{cc} \quad \textbf{[1-7]}$$

The absorption efficiency, η_{abs}, is equal to the fraction of impinging photons that are absorbed by the s-SWCNT film. Naively, this fraction may be written in the form $1 - \exp(-\alpha t)$ where α is the absorptivity of the s-SWCNT film and t is the film thickness; however, due to optical interference in the device, more complicated methods are required to calculate this value. **Chapters 3** and **5** will discuss some of these methods in more detail; it is sufficient here to assume that a thicker film leads to more light being absorbed, and a higher η_{abs}. On the other hand, the diffusion efficiency η_{diff} strongly decreases as the s-SWCNT film becomes thicker due to the generally poor exciton diffusion length in s-SWCNT films. Since the dissociation efficiency η_{diss} and charge collection efficiency η_{cc} are near unity,[34] maximizing the EQE is often a tradeoff between thin films with low η_{abs} and high η_{diff} and thick films with high η_{abs} and low η_{diff}. **Chapter 3** explores the optimization of thin-film interference in s-SWCNT/C_{60} photovoltaic cells to maximize the EQE, and therefore, J_{SC}, ultimately achieving power conversion efficiency exceeding 1% for the first time. **Chapter 4** describes the behavior of s-SWCNT/C_{60} devices under low temperature and provides an estimate for the maximum open-circuit voltage in these devices. In **Chapter 5** the controlled addition of defects to s-SWCNTs is paired with Monte Carlo simulations to describe barriers to efficient exciton transport within these devices. Finally, in **Chapter 6**, I show that both EQE and FF can be improved by controlling the method of s-SWCNT dispersal, using high-shear mixing in lieu of sonication, to increase nanotube length and decrease exciton quenching at defects and ends.

CHAPTER 2: BINDING CONFIGURATION AND COVERAGE OF PFO ON CARBON NANOTUBES

Adapted from:

Shea, M. J.; Mehlenbacher, R. D.; Zanni, M. T.; Arnold, M. S., Experimental Measurement of the Binding Configuration and Coverage of Chirality-Sorting Polyfluorenes on Carbon Nanotubes. *J. Phys. Chem. Lett.* 2014, **5**, 3742-3749.

The author contributed the majority of the experimental design, sample preparation, data analysis, and manuscript preparation. The author recognizes Dr. Randy Mehlenbacher and Dr. Martin Zanni for their contributions to transient absorbance measurements.

s-SWCNT SORTING

The implementation of SWCNTs in many applications has been constrained by their electronic heterogeneity.[35] The presence of m-SWCNTs degrades the performance of devices requiring highly pure semiconducting s-SWCNTs. In solar cells these m-SWCNTs quench photogenerated excitons, lowering efficiency,[17] and in SWCNT field effect transistors, they reduce the on-off ratio and increase power consumption.[36] Even among pure s-SWCNTs, the effect of diameter and chiral angle polydispersity on device performance can be significant because s-SWCNT bandgap is roughly inversely proportional to diameter. Wu et al. found that even a few percent of small-bandgap s-SWCNTs in an otherwise monodisperse film of larger bandgap s-SWCNTs significantly degrade photovoltaic device performance.[17] Therefore, it is vital to obtain highly pure s-SWCNTs with control over bandgap polydispersity for electronic devices.

Several methods have been developed to separate s- and m-SWCNTs.[37-38] One of the most promising methods for separation uses aromatic organic polymers as selective dispersants. As reported by Nish et al.[7] and Hwang et al.,[39] polymers in the polyfluorene family selectively wrap and disperse specific types of s-SWCNTs in organic solvent. For example, a member of this family, poly(9,9-dioctylfluorene-2,7-diyl) (PFO) was shown to have a particular affinity for the (7,5), (7,6), (8,6), (8,7), and (9,7) chiralities of s-SWCNTs when dispersed in toluene, where (*n*,*m*) denotes the "chirality" and a linear combination of graphene's lattice vectors that is coincident with the SWCNT circumference.[5] In the PFO-mediated

separation process, the polymer strands are believed to solubilize the normally-insoluble SWCNTs by wrapping around them, with alkyl side chains branching away from the SWCNTs into the solvent.[40] PFO and similar polymers have been used to produce relatively high-purity (>99%) s-SWCNTs for transistors,[40-46] photodetectors,[15, 47-48] and solar cells.[14, 49-51]

The factors that promote the selective wrapping of SWCNTs by PFO are not well understood. Empirically, it is known that PFO readily wraps semiconducting near-armchair SWCNTs with diameters near 1 nm;[7] however, the reasons for these strong preferences are not immediately apparent. It is anticipated that the selectivity is related to the PFO-SWCNT binding energy, which affects the wrapping geometry and surface coverage of PFO on the SWCNT. Molecular dynamics modeling has been used to investigate the binding energy, surface coverage, and conformation of conjugated polymers on different (*n*,*m*) chiralities of SWCNTs as a function of the polymer's structure and sidechain length for PFO as well as other conjugated polymers.[40, 50, 52-55] However, thus far few experimental measurements of these parameters exist to confirm the modeling.

In this work, we experimentally explore the factors that lead to chirality and electronic type-sorting. First, we measure the concentration of s- and m-SWCNTs in dispersions of PFO-wrapped SWCNTs as a function of the concentration of PFO in the solution during ultrasonication and determine the efficacy of electronic type-sorting. Second, we measure the coverage of PFO on s-SWCNTs as a function of the PFO concentration in solution and use this relationship to determine the equilibrium concentration for half coverage, K_A. Finally, we use photoluminescence anisotropy measurements to determine the wrapping angle of the PFO around the SWCNTs.

ENERGY TRANSFER AND PFO COVERAGE

Dispersed PFO-SWCNT solutions are analyzed by optical absorption spectroscopy to estimate s- and m-SWCNT concentration, as a function of the PFO concentration in solution during ultrasonication, which we will refer to as simply the "PFO concentration" in the remainder of this chapter. The optical absorption is displayed as a function of wavelength for all PFO concentrations studied in **Figure 2-1A**. The

peaks corresponding to the S_{11} transitions of the (7,5), (7,6), (8,6), (8,7), and (9,7) SWCNTs are located at 1055, 1135, 1195, 1280, and 1345 nm, respectively. The absorption peaks corresponding to the second-order S_{22} transitions are located at 655 nm for the (7,5) and (7,6) SWCNTs, 724 nm for the (8,6) SWCNT, 738 nm for the (8,7) SWCNTs, and 798 nm for the (9,7) SWCNT. A broad background is seen in solutions in which there was a high PFO concentration. We fit Voigt line shapes to the five absorption peaks from the (7,5), (7,6), (8,6), (8,7), and (9,7) SWCNTs and integrate under the curves. We use the integrated carbon SWCNT optical cross sections reported by Streit et al.[56] to calculate the SWCNT concentrations of each chirality in the solution. The peaks observed between 500 and 600 nm at the highest PFO concentrations are m-SWCNT M_{11} absorption signatures.[57] We estimate the m-SWCNT concentration from the area under these peaks (see supporting information Section I).

The total concentrations of s- and m-SWCNTs are displayed as a function of PFO concentration in **Figure 2-1B**. The m-SWCNTs are only detectable in the solution at the highest PFO concentrations. We define the sorting ratio to be the ratio of s- to m-SWCNT in solution. At 5 mg/mL PFO, the sorting ratio is barely better than 2:1, which is roughly the ratio of s-SWCNT to m-SWCNT in the starting material. However, at sufficiently low PFO concentration, here, less than 1 mg/mL, there is no absorption signature from m-SWCNT absorption, and the sorting ratio is greater than 90:1. The detection limit of 0.01 μg/mL m-SWCNT is due to insufficient signal-to-noise ratio in the absorption spectra, and we expect the true s:m sorting ratio is even higher as the PFO concentration decreases. Simple extrapolation below 1 mg/mL suggests that there is good reason to expect that in the dilute PFO regime m-SWCNTs account for dramatically less than 1% of SWCNTs in solution. In addition, it is worth noting that the selectivity decreases as the s-SWCNT yield increases, thus there is a trade-off between these two characteristics. This dependence of the sorting ratio on the PFO concentration implies that there is a difference in the PFO-SWCNT binding energy between s- and m-SWCNTs and possibly a difference in preferred polymer conformation on the SWCNTs.

To learn more about the PFO wrapping coverage and binding configuration, we next perform photoluminescence (PL) measurements. We measure the amount of energy transfer from the PFO to the s-

SWCNTs to quantify the PFO coverage on different (*n*,*m*) species, and we use polarization anisotropy data to determine the binding configuration, using a Horiba NanoLog iHR 320 outfitted with input/output linear polarizers. Excitation-emission photoluminescence (PLE) maps are constructed by varying excitation wavelength from 300 to 820 nm and measuring PL emission over the range of 900 to 1400 nm. The solutions are measured in square cuvettes with a 2 mm path length, and the emission is measured perpendicular to the excitation. The spectra are normalized to the excitation beam intensity at each excitation wavelength and corrected for the relative collection efficiency and photodetector responsivity at the emission wavelength. In addition, we correct the spectra for absorption losses due to the moderate optical density in the most concentrated solutions (see supporting information Section II).

A representative PLE map, taken of the 0.5 mg/mL PFO dispersion, is shown in **Figure 2-1C**. Peaks corresponding to the (7,5), (7,6), (8,6), (8,7), and (9,7) SWCNTs are denoted on the map. The onset of PL for all chiralities near 350 nm arises due to exciton energy transfer to the s-SWCNT from photoexcited PFO molecules wrapping the SWCNT, where emission occurs at the respective S_{11}.[58] We integrate the PL over the region spanning the S_{22} excitation range (550 to 820 nm) and S_{11} emission range (1000 to 1360 nm), enclosed by the grey dotted line labelled "S_{22} exc." in **Figure 2-1C**, and plot the total PL intensity in **Figure 2-1D** as a function of PFO concentration. At low PFO concentration, the total PL intensity increases linearly with the dispersed concentration of SWCNTs (measured from absorption). However, interestingly, at high PFO concentration, the total PL intensity begins to saturate, even as the dispersed concentration of SWCNTs continues to increase. The PL intensity from each (*n*,*m*) species saturates similarly (see supporting information **Figure 2-S2**). The PLE maps are corrected for reabsorption losses; thus, the PL reduction cannot be assigned to a reabsorption effect. Importantly, the saturation of the PL begins to occur at the PFO concentration where the absorption background rises and m-SWCNTs begin to account for a measureable fraction of the SWCNTs in solution.

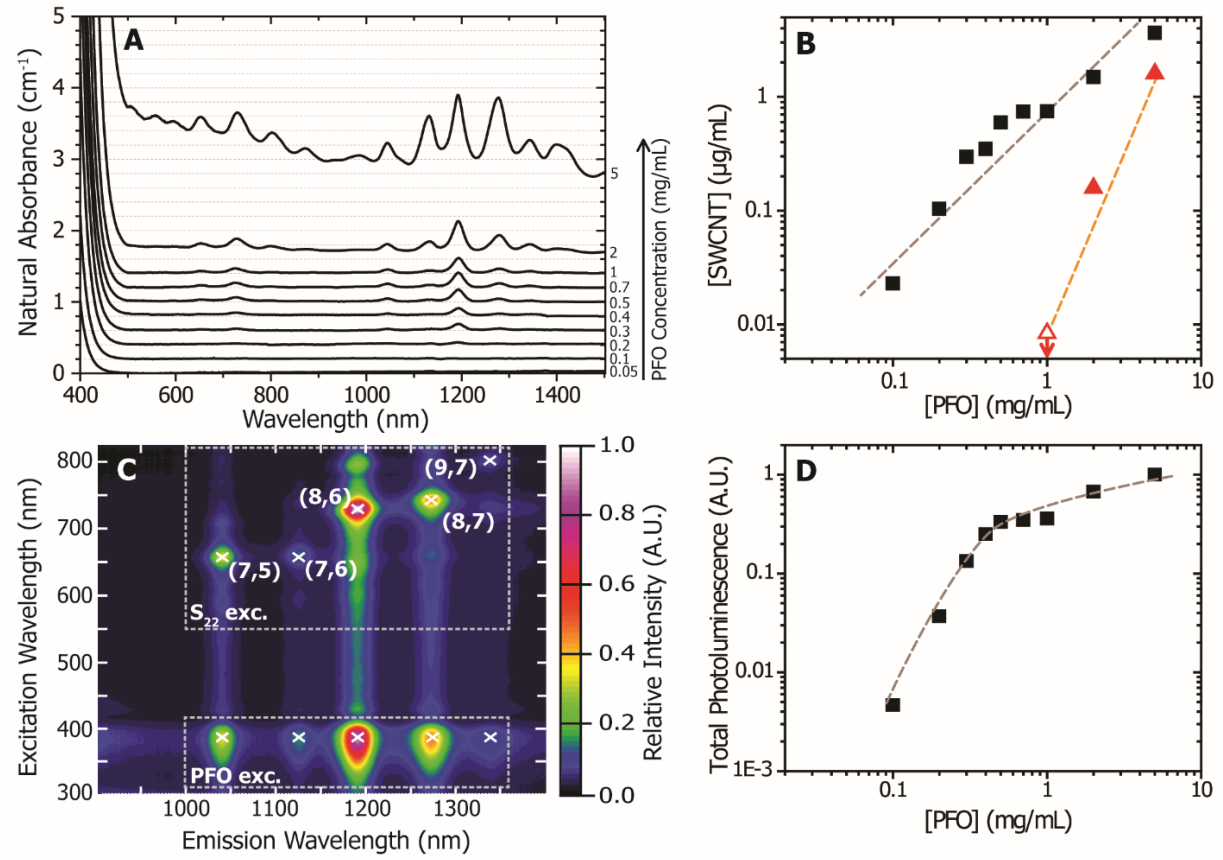

Figure 2-1. (A) The optical absorbance spectra of the SWCNT dispersions in toluene for PFO concentration of 0.05 mg/mL to 5 mg/mL (spectra are offset by 0.2 cm^{-1} each). Note the increase in background and metallic peaks near 500 nm as the PFO concentration increases. (B) The concentration of semiconducting (black) and metallic (red) SWCNTs are calculated by integrating the peak areas. (C) PLE map for the 0.5 mg/mL dispersion with features representative of the entire set of solutions. Peaks corresponding to the S_{22} of the (7,5), (7,6), (8,6), (8,7), and (9,7) SWCNTs are denoted. The peaks at 380 nm excitation are due to exciton energy transfer from PFO to SWCNTs. The grey dotted line enclosing the region labelled "S_{22} exc." represents the bounds on the integrated PL. (D) Integrated PLE spectra for the SWCNTs plotted as a function of PFO concentration in the dispersion. The PL at high concentrations saturates as m-SWCNTs begin appearing in solution.

In addition, the polydispersity among s-SWCNTs begins to increase at the highest PFO concentrations. While at PFO concentrations < 1 mg/mL, PL intensity is detected only from the (7,5), (7,6), (8,6), (8,7), and (9,7) species, at PFO concentrations >1 mL/mL, weak signatures of the (6,5), (10,2), and (9,5) species begin to appear in PLE maps (see supporting information **Figure 2-S3**). Moreover, signatures of larger diameter nanotubes with S_{11} beyond 1400 nm are also observed in the absorption spectra (**Figure 2-1A**) for PFO concentrations > 1 mg/mL. (These signatures are beyond the spectral window characterized

via PLE). Thus, at high PFO concentration, an overall decrease in selectivity is observed, not just between s- and m-SWCNTs, but among the species of s-SWCNTs selected, as well.

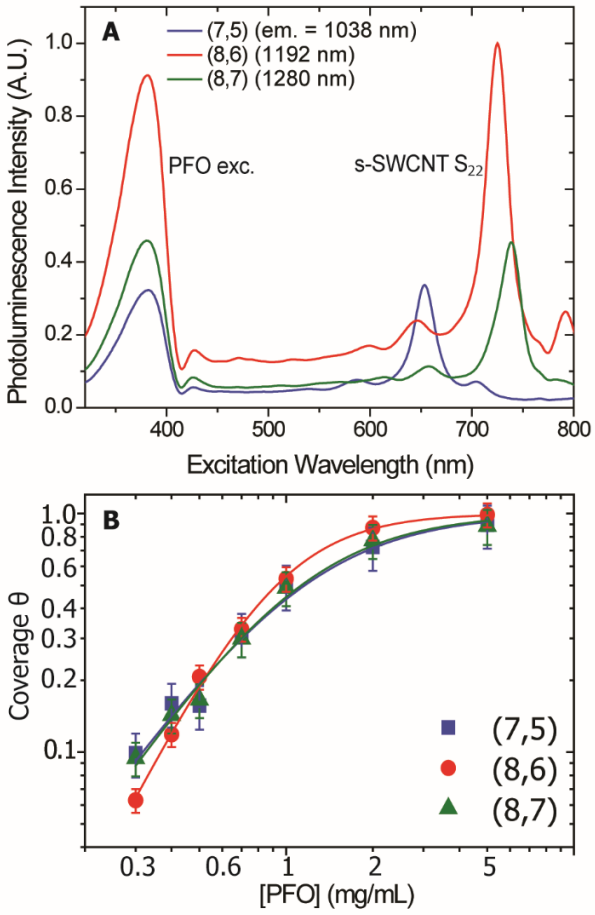

Figure 2-2. (A) Photoluminescence from (7,5) (blue), (8,6) (red), and (8,7) (green) SWCNTs as a function of excitation wavelength for [PFO] = 0.5 mg/mL, normalized to the peak emission from the (8,6) SWCNT. The PFO excitation appears as the peak near 380 nm and the peaks between 650 and 750 nm correspond to the direct excitation of the SWCNTs' respective S_{22} transitions. **(B)** Coverage of PFO on (7,5) (blue, squares), (8,6) (red, circles), and (8,7) (green, triangles) SWCNTs versus PFO concentration. Curves are fits to the Hill equation and used to extract the Hill coefficient *n* and K_A (See Table 1).

Two phenomena may drive the decreased selectivity at the highest PFO concentrations. First, the selectivity of PFO for the (7,5), (7,6), (8,6), (8,7), and (9,7) SWCNTs at low PFO concentrations is well documented; however, the selectivity may decrease at high PFO concentrations as the PFO is driven onto other species of SWCNTs with lower PFO affinity. For example, it may be possible for PFO to individually disperse m-SWCNTs, the (6,5), (10,2), and (9,5) SWCNTs, or other (*n*,*m*) species at sufficiently high PFO

concentration, depending on the (*n*,*m*)-specific binding affinity. Second, it may be possible to drive PFO to bind to not just individual SWCNTs, but bundles of them, at sufficiently high PFO concentration. The composition of these bundles could potentially be as polydisperse as the raw, unsorted starting SWCNT material. Three experimental observations are consistent with this latter case. The large background in the absorption spectra observed for PFO concentration > 1 mg/mL is consistent with the absorption spectrum of polydisperse bundles.[59] Moreover, inter-nanotube energy transfer cross-peaks are evident at high PFO concentrations as well (see supporting information **Figure 2-S4**). These cross-peaks are only possible when different (*n*,*m*) species of SWCNTs are in intimate contact with one another. Finally, the saturated PL intensity can be attributed to the presence of m-SWCNTs, which will predominately quench the PL from bundles containing more than a few nanotubes (see supporting information **Figure 2-S5**).

Spectroscopic evidence of exciton energy transfer from PFO to SWCNTs has been reported by Nish et al. in photoluminescence spectra.[58] We use this phenomenon to determine the surface coverage of PFO on SWCNTs. We quantify the coverage by measuring the intensity of cross-peaks in the PLE maps at excitation energies corresponding to the optical bandgap of the PFO and emission from the s-SWCNTs. Excitation spectra are compared in **Figure 2-2A**. Two prominent peaks are apparent: one at the PFO absorption maximum near 380 nm and the other at the S_{22} of the respective SWCNT. There is a small overlap between the PFO absorption and the S_{33}[60] of some of the (*n*,*m*) SWCNTs; however, the overlap[61] is generally small and subtracted before calculating the PFO surface coverage (see supporting information **Figure 2-S6**). The ratio of the intensity of the PFO peak to the intensity of the S_{22} peak is proportional to PFO mass loading, γ, times the ratio of the absorption cross-sections of PFO and the S_{22} transition, as well as factors relating to the S_{22}-S_{11} relaxation efficiency and the PFO-S_{11} energy transfer efficiency (see supporting information Section VII). Lebedkin et al. studied the S_{22}-S_{11} relaxation efficiency of PFO-wrapped HiPCO SWCNTs and found relatively (*n*,m)-invariant relaxation efficiencies greater than 80%.[8] Calculation of the PFO-S_{11} energy transfer efficiency is somewhat more difficult due to the preponderance of free PFO in solution. However, we draw from experimental measurements conducted on porphyrin-SWCNT complexes, in which the porphyrin-SWCNT energy transfer efficiency has been measured to be

>99.9%, and the kinetics of the energy transfer are independent of chirality.[62-63] Energy transfer in both porphyrin-SWCNT and PFO-SWCNT complexes is believed to be a non-Förster, non-resonant process, namely direct exciton transfer *via* wavefunction overlap, a process that is relatively bandgap-independent. Additionally, for corroboration, we have performed ultrafast transient absorption spectroscopy, described in the supporting information in **Figure 2-S7**. We observe that energy transfer from PFO to SWCNTs occurs within 500 fs. This rate is nearly three orders of magnitude times faster than the PFO fluorescence lifetime of 410ps,[64] implying that the energy transfer efficiency is likely >99% and invariant with respect to (*n*,*m*).

For the dissociation reaction $PFO@\text{SWCNT} \rightleftarrows PFO + \text{SWCNT}$, the PFO acts as a ligand and the SWCNT a macromolecule whose affinity for the PFO is dependent on environmental conditions such as temperature and solvent, as well as materials parameters like chirality and electronic type. In addition, we expect the SWCNT's affinity for PFO to be dependent on the number of PFO strands already wrapping the SWCNT. We calculate the mass loading γ by multiplying the ratio of the PFO peak to the S_{22} peak by the ratio of absorption cross sections (see supporting information Section VIII). We fit γ to the Hill equation for cooperative binding,[65]

$$\gamma = \gamma_s \left[\left(\frac{K_A}{[PFO]} \right)^n + 1 \right]^{-1} \quad \textbf{[2-1]}$$

and extract constants γ_s, K_A, and n. γ_s is the mass loading of PFO to nanotube when there is saturated, presumably monolayer coverage. K_A is the equilibrium concentration of PFO at which there will be half coverage of the SWCNT surface. It should be noted that because the selective binding occurs during ultrasonication, the extracted K_A likely reflects binding characteristics at this condition. We divide the mass loading γ by the calculated saturation mass loading γ_s to solve for θ, the fractional coverage of PFO on the SWCNT surface.

$$\theta = \frac{\gamma}{\gamma_s} = \left[\left(\frac{K_A}{[PFO]} \right)^n + 1 \right]^{-1} \quad \textbf{[2-2]}$$

We plot θ as a function of concentration for the (7,5), (8,6), and (8,7) in **Figure 2-2B**. The (7,6) chirality was omitted due to the congestion of its S_{11} transition with the toluene absorption peak near 1150 nm, and the (9,7) chirality was omitted due to its low abundance and poor PL signal-to-noise ratio. The best fit lines for each SWCNT corresponding to equation [2] are plotted in **Figure 2-2B**, and the constants n and K_A are extracted from the fit. The saturation coverage γ_s, Hill coefficient n, and K_A are presented as a function of chirality in Table 1. We observe several trends. First, the SWCNTs investigated all display $n > 1$, suggesting a positive cooperativity; the presence of a ligand encourages the binding of additional ligands, provided there are still available binding sites, i.e. part of the s-SWCNT surface is still bare. This positive cooperativity may be due to the zipping of the alkyl side chains of two adjacent PFO strands, as suggested in molecular dynamics simulations by Gomulya et al.[40] Second, K_A is comparable among the three (*n*,*m*) analyzed. We suggest that other (*n*,*m*) not well dispersed have a substantially larger K_A. Such SWCNTs with lower affinity would be expected to have coverage curves that shift to the right. Because the solubility of the PFO/SWCNT complex is intimately tied to the surface coverage of PFO on the SWCNT, a disparity in the surface coverage between two species of SWCNTs will give rise to selectivity for and the dispersion of one SWCNT over the other. It is not surprising, then, that the K_A of the three s-SWCNTs studied here do not significantly differ, since they are all well-dispersed by PFO. On the other hand, peaks corresponding to other chiralities of low affinity SWCNTs, including m-SWCNTs, begin to appear in the absorbance and PLE spectra at much higher PFO concentrations, suggesting that the K_A for these SWCNTs is much higher. The lack of PL from m-SWCNTs and the absence of a full coverage versus PFO concentration curve for the low affinity s-SWCNTs preclude the precise quantification of K_A for these species. However, we can estimate that the K_A is at least an order of magnitude higher. For example, we can estimate K_A for metallic/bundled SWCNTs by noting that the dispersed SWCNT concentration versus PFO concentration curve in **Figure 2-1B** is shifted to higher PFO concentration by about one order of magnitude. Thus, assuming a similar relationship between coverage and solubility, we estimate $K_A \approx 10$ mg/mL for the binding of PFO to metallic/bundled SWNCTs. We suggest that the K_A measured for the (7,5), (8,6), and

(8,7) SWCNTs and estimated for m-SWCNTs be a guide to improve the electronic type separation of SWCNTs.

Table 2-1. Mass loading at saturated coverage, Hill coefficient, and concentration at half coverage as a function of (n,m) chirality. These assume an S_{22} to S_{11} relaxation efficiency of 80% and a PFO to S_{11} net energy transfer and relaxation efficiency of 80%. The effects of uncertainties in these efficiencies are discussed in the supporting information.

SWCNT (n,m)	$\boldsymbol{\gamma_s}$ *(PFO/CNT)*	$\boldsymbol{n}$	$\boldsymbol{K_A}$ *(mg/mL)*
(7,5)	3.65 ± 0.64	1.70 ± 0.45	1.16 ± 0.30
(8,6)	2.01 ± 0.10	2.37 ± 0.29	0.93 ± 0.12
(8,7)	2.60 ± 0.32	1.77 ± 0.34	1.13 ± 0.26

BINDING CONFIGURATION VIA PL ANISOTROPY

Next, we determine the binding angle of PFO on s-SWCNTs, α, from the anisotropy of the PL energy transfer from PFO to SWCNTs. We illuminate the PFO-SWCNT dispersions with vertically (V) and horizontally (H) polarized excitation beams and measure the PL emission through V and H polarization filters. The measured PL intensity is specified by I_{XY} where X and Y denote the excitation and emission polarizations, respectively. The PL anisotropy $\langle r \rangle$ is calculated using the relationship,

$$\langle r \rangle = \frac{I_{VV} - G I_{VH}}{I_{VV} + 2G I_{VH}} \qquad \textbf{[2-3]}$$

where G is an instrument-dependent calibration factor accounting for the difference in the responsivity of the emission side optics and detector to horizontally polarized light with respect to vertically polarized light. G is determined according to the relationship $G = I_{HV}/I_{HH}$ and is 1.08 for our setup. We measure the PL anisotropy as a function of PFO concentration for both [PFO-excitation, S_{11} s-SWCNT-emission] and [S_{22} s-SWCNT-excitation, S_{11} s-SWCNT-emission]. The results are displayed in **Figure 2-3A**. The [S_{22} s-SWCNT-excitation, S_{11} s-SWCNT-emission] anisotropy is PFO concentration-invariant for all three species of SWCNT, near the expected anisotropy of $\langle r \rangle = 0.40$ for a system where the excitation and emission transition dipoles align (i.e. both are parallel to the long axis of the SWCNTs).[13] On the contrary, the [PFO-excitation, S_{11} s-SWCNT-emission] PL anisotropy is significantly smaller, between 0.05 and 0.2

depending on (*n*,*m*) and the PFO concentration, indicating that the excitation and emission transition dipoles are not parallel in this case.

These data indicate that the PFO excitation dipole, $\vec{\mu}$, is not parallel to the long axis of the SWCNTs, $\vec{D}$. The angle between the two vectors, δ, is determined by $\langle r \rangle$ according to

$$\delta = \cos^{-1} \sqrt{\frac{5\langle r \rangle + 1}{3}}. \quad \textbf{[2-4]}$$

However, δ does not directly specify the binding angle of PFO on the SWCNTs, α, because $\vec{\mu}$ is not parallel to the polymer backbone vector, $\vec{P}$ (**Figure 2-3B**). The angle β between $\vec{\mu}$ and $\vec{P}$ has reported values that range from 21 degrees[66] to 26 degrees[67]. The three angles α, δ, and β depend on one another according to the relationship $\alpha = \delta \pm \beta$; however, only $\alpha = \delta - \beta$ yields physically realistic binding angles.

We first evaluate the binding angle α at a low PFO concentration of 0.2 mg/mL, where we know from **Figure 2-2B** that the coverage of PFO on the SWCNTs is less than 10% and thus there is little cooperative interaction among the PFO chains. In this limit, using a β of 23.5°, α is 12±2°, 17±2°, and 14±2° on the (7,5), (8,6), and (8,7) SWCNTs, respectively. As the PFO concentration is increased, $\langle r \rangle$ decreases. For example, for the (7,5) SWCNT, $\langle r \rangle$ is 0.2 at a PFO concentration of 0.2 mg/mL corresponding to an α of 12°; but, $\langle r \rangle$ decreases to 0.1 at a PFO concentration of 5 mg/mL corresponding to an α of 22°. For all three (*n*,*m*) characterized, α similarly increases with increasing PFO concentration. This trend indicates that as the coverage of PFO on the SWCNTs increases and cooperative interactions among PFO chains increase, the average binding angle increases. It may also be that as coverage increases the PFO adopts a more disordered conformation. In addition, PFO wrapping bundles of SWCNTs may not be able to adopt a favored wrapping angle, instead producing mixtures of angles depending on the bundle size and composition.

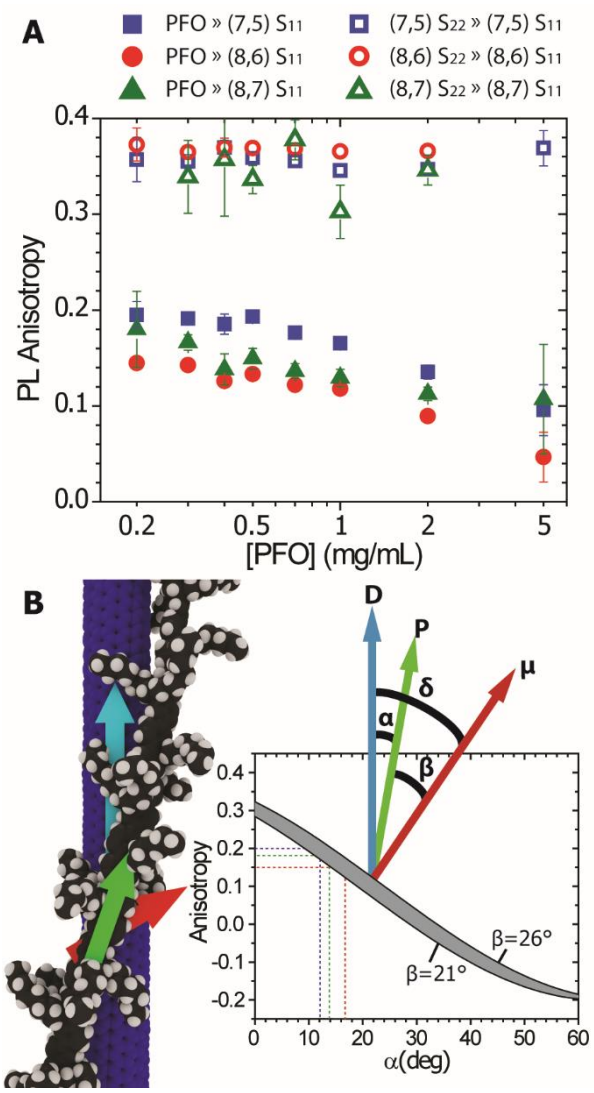

Figure 2-3. (A) The measured anisotropy for the PFO-SWCNT dispersions as a function of PFO concentration for (7,5) (blue, squares), (8,6) (red, circles), and (8,7) (green, triangles) from direct excitation of the SWCNTs (open) and excitation of the wrapping PFO (filled). **(B)** The schematic of PFO wrapping a SWCNT displaying the SWCNT transition dipole $\vec{D}$ (blue), the polymer backbone $\vec{P}$ (green), the polymer transition dipole $\vec{\mu}$ (red), the wrapping angle α, and the dipole angle β, reproduced to the right. Inset: The modeled anisotropy of the PFO-SWCNT system for exciting PFO and SWCNT emission following exciton energy transfer. The line to the right is the calculated anisotropy for $\beta = 26°$, while the line to the left is the anisotropy for $\beta = 21°$. Dotted lines are displayed for the measured anisotropies in **(A)** at PFO concentration of 0.2 mg/mL.

Other groups have sought to model the PFO-SWCNT system and have found that the PFO wraps the SWCNT in a regular helical fashion, however the binding angle predicted by simulations varies widely, from nearly 0° [40] to over 20°.[52] On the other hand, several groups have experimentally observed the helical

arrangement of polymers other than polyfluorenes on the surface of SWCNTs in both aqueous and organic solvent systems. Deria et al. report chiral-selective ionic polymer wrapping of SWCNTs with pitch length 10 nm.[68] Giulianini et al. characterized the poly(thiophene)-SWCNT system and discovered similar helical wrapping patterns with relatively high wrapping angles giving rise to a pitch length of 5 nm.[25] For the wrapping angles we measure here, we estimate pitches ranging from 7 to 14 nm. The similarity of wrapping geometry between these different polymers indicates that a variety of polymer-SWCNT systems operate under similar constraints. Experiments spanning dozens of conjugated polymers suggest that selectivity is dictated by the dihedral angle and steric hindrance of the wrapping polymer on the surface of the nanotube.[69] Quantitative comparison between experiment and simulations are complicated by the fact that simulations to date have incorporated much shorter PFO chains than are used our experiments. Simulation of inter-polymer and polymer-SWCNT interactions, including solvents, over many periods may be necessary to establish the configurations that are not sterically prohibited and to predict a characteristic binding angle that matches experimental results. The specific relationship between the chirality and wrapping angle is difficult to ascertain from the three SWCNTs studied here, and should be a focus of future research.

Through optical absorption, excitation-emission photoluminescence mapping, and photoluminescence anisotropy, we have described the binding configuration and surface coverage of PFO on s-SWCNTs. Our data show that the coverage of PFO on a SWCNT can be modeled according to the Hill equation. The Hill equation predicts a coverage of PFO that depends on the free PFO concentration in solution during ultrasonication and the (*n*,*m*)-dependent binding affinity, which affects K_A (Eq. 2). At low PFO concentration, we find that the PFO is ordered on the SWCNT surface with characteristic wrapping angles of 12±2°, 17±2°, and 14±2° for the (7,5), (8,6), and (8,7) SWCNTs, respectively, whereas at the high PFO concentration the average wrapping angle increases. While K_A = 0.9 – 1.2 mg/mL for the (7,5), (8,6), and (8,7) s-SWCNTs most readily dispersed by PFO, the K_A for (*n*,*m*) SWCNTs not dispersed must be considerably higher, and we infer that the K_A for metallic and bundles SWCNTs is nearly an order of magnitude larger (10 mg/mL).

These findings can serve to better understand the chemistry and thermodynamics of the selectivity of PFO-SWCNT binding and to confirm and guide computational modeling efforts. Practically, our data are important because they indicate that the best semiconductor-metallic sorting occurs at low PFO concentrations during ultrasonication, at which the PFO strands become more ordered on the SWCNT surface and the surface coverage is low. These observations can guide the development of procedures for isolating semiconducting SWCNTs for applications in electronics and optoelectronics where even vanishingly small concentration of metallic SWCNTs can lead to decreased performance.

SUPPORTING INFORMATION

s-SWCNT Separations.

SWCNTs grown by the high pressure carbon monoxide (HiPCO) process (NanoIntegris Lot#R1-831) are dispersed by a horn tip ultrasonicator (Fisher Model 500) at 64 W using a procedure similar to that of Nish et al.[7] PFO (180 mg) was purchased from American Dye Source, Inc., (molecular weight of 53000, polydispersity index of 2.5, Lot#13F002A1) and dissolved in 36 mL of toluene (Fisher) at 90°C until the solution was clear and yellow-green. The 5 mg/mL stock solution was diluted into aliquots of 15 mL each ranging in concentration from 0.05 to 5 mg/mL and allowed to cool to room temperature. HiPCO "mud" (5.2 wt% solids) was added to each aliquot so each contained approximately 1.5 mg SWCNTs. The sonication took place in a stainless steel crucible to allow for efficient heat transfer in a water bath at 22°C for 10 minutes. The temperature of the solution reached 30°C over the course of the sonication. Immediately following sonication, the dispersions were opaque and black. The dispersed SWCNT slurries were centrifuged at 300,000 g for 15 minutes to separate the amorphous carbon, catalyst particles, SWCNT bundles, and unwrapped varieties of m- and s-SWCNTs, which were collected in a pellet at the bottom of the centrifuge tube. The top 90% of the supernatant was removed and set aside for analysis. The supernatants ranged in color from clear and colorless for low PFO concentrations, to yellow-green for moderate PFO concentrations, to grey-yellow for high PFO concentrations.

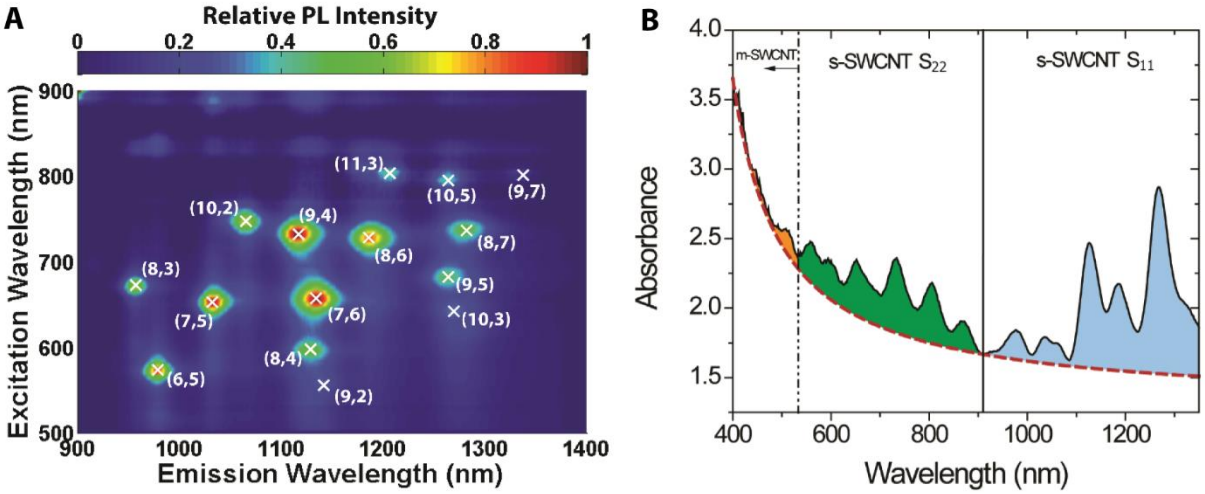

Figure 2-S1. (A) Excitation-emission photoluminescence map of sodium cholate-dispersed carbon nanotubes from HiPCO starting distribution. At least 15 distinct chiralities are observed.[1] (B) The absorbance of the sodium cholate dispersed carbon nanotubes has a large background (red, dashed) and many overlapping peaks. From photoluminescence data, no nanotube has an S_{22} transition below 550 nm, and peaks in this region correlate with metallic nanotubes in solution.

Determination of metallic concentrations.

We dispersed 115 mg of the HiPCO starting material (NanoIntegris, Lot#R1-831, 5.3% SWCNT by weight) in 15 mL of 0.1 mg/mL sodium cholate (Sigma) in deionized water using a Fisher Model 500 sonic dismembrator at 40% amplitude (64 W) for 10 minutes. The slurry was centrifuged at 300,000 g for 15 minutes to remove aggregates, and the supernatant was drawn off and saved for analysis. The solution was diluted 20*x* before measuring optical absorbance and photoluminescence. The excitation-emission photoluminescence map (**Figure 2-S1A**) shows the presence of at least 15 species of semiconducting single walled carbon nanotube (s-SWCNT) with S_{11} ranging from 950 to 1350 nm and S_{22} ranging from 550 to 820 nm.

The optical absorbance of the sample (**Figure 2-S1B**) contains the expected congestion of peaks in the S_{11} and S_{22} regions, in addition to a large background. The small peaks below 550 nm do not correlate with any s-SWCNTs in solution, so we attribute these to metallic nanotubes. We subtract a background of

$$y = \frac{a}{x - b} + y_0 \quad \textbf{[2-S1]}$$

where *a*, *b*, and y_0 are fit constants (see **Figure 2-S1B**, red curve) and integrate the resulting curve from 430 nm to 530 nm, where the majority of the metallic peaks exist. We also integrate the S_{11} transition region from 900 to 1400 nm and define the ratio of the metallic integral to the semiconducting integral. Since sodium cholate solubilizes s- and m-SWCNTs roughly equally, we define the proportionality constant k as follows:

$$k \times \frac{\int A_{metal} dE}{\int A_{semi} dE} = \frac{C_{metal}}{C_{semi}} = 0.5 \quad \textbf{[2-S2]}$$

For our dispersion we find $k = 1.77$.

Next, we measure the absorbance of our PFO-dispersed nanotube solutions and measure the s-SWCNT concentration in accordance with the text. To estimate the concentration of metallic nanotubes in these solutions, we integrate the M_{11} and S_{11} regions as in the sodium cholate solution. The metallic concentration is then

$$C_{metal} = C_{semi} \times k \times \frac{\int A_{metal} dE}{\int A_{semi} dE}. \quad \textbf{[2-S3]}$$

Because of spectral congestion, this only provides a rough estimate for m-SWCNT concentration and m:s ratio, but this rough estimate is sufficient for understanding how the m:s ratio decreases with decreasing PFO concentration.

PL saturation as a function of chirality.

We integrate the PLE maps around each S_{22}/S_{11} peak (integrated over a ±30 nm box in both exciton and emission axes) for each species of SWCNT in **Figure 2-S2**. Each SWCNT species' PL saturates roughly equally with respect to [PFO].

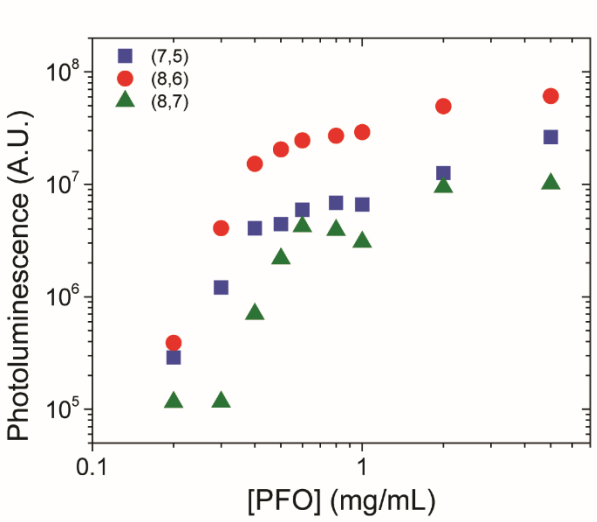

Figure 2-S2. Individual photoluminescence intensity for S_{22} excitation, S_{11} emission for the three s-SWCNT species studied. (7,5) (blue, squares), (8,6) (red, circles), (8,7) (green, triangles) photoluminescence saturate similarly.

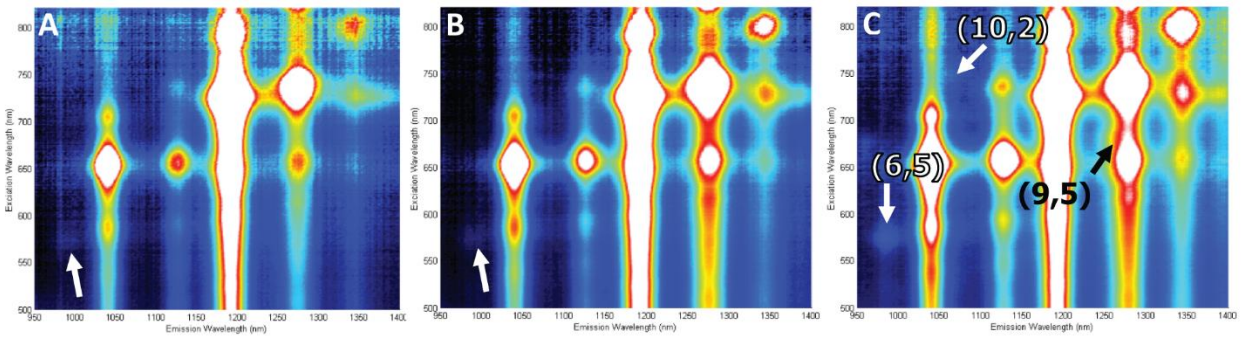

Figure 2-S3. At the highest PFO concentrations **(A)** 1 mg/mL, **(B)** 2 mg/mL, **(C)** 5 mg/mL, minority SWCNTs begin to appear, noticeably (6,5), (10,2), and (9,5). All the PLE maps are normalized to the (8,6) peak.

Evidence for dispersion of SWCNT bundles.

We compare the excitation spectra of (7,5), (8,6), and (8,7) s-SWCNTs for the dispersions obtained with [PFO] = 0.5 mg/mL and 5 mg/mL to seek signatures of increased energy transfer within solutions at high PFO concentration. The excitation spectra are shown in **Figure 2-S4.** The arrow in **(B)** and **(C)** denotes increased energy transfer from the (7,5) and (7,6) SWCNTs to the (8,7) SWCNT. This increase is not

attributed an increase in the optical cross-section of the phonon sideband (X) because the phonon sideband in **(A)** remains unchanged. enotes increased energy transfer from the (8,6) and (8,7) SWCNTs to the (9,7) SWCNT.

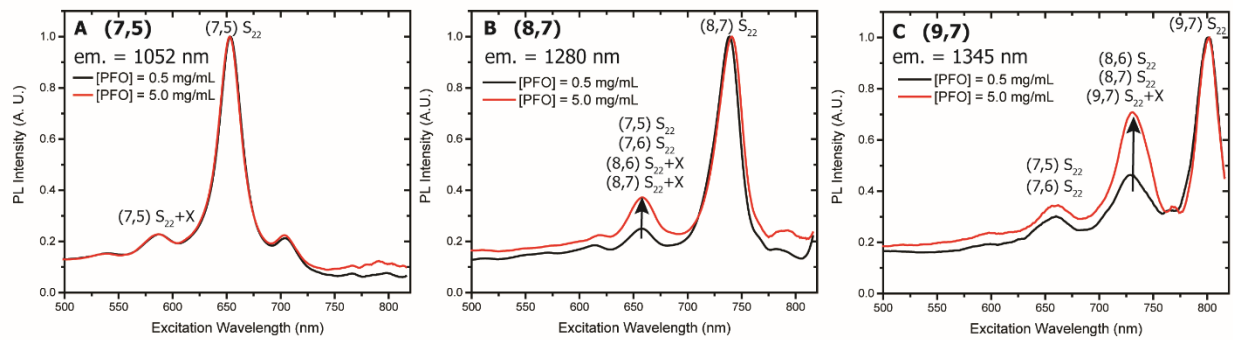

Figure 2-S4. Evidence for dispersion of SWCNT bundles. The arrows in these PLE excitation spectra indicate increased inter-SWCNT energy transfer at higher PFO concentration. Specifically, **(A)**, **(B)**, and **(C)** show excitation spectra of (7,5), (8,7), and (9,7) SWCNTs, respectively, at both PFO concentrations of 0.5 mg/mL (black) and 5.0 mg/mL(red), normalized to the PL intensity measured for excitation at the S_{22} of the (7,5), (8,7), and (9,7) SWCNTs, respectively.

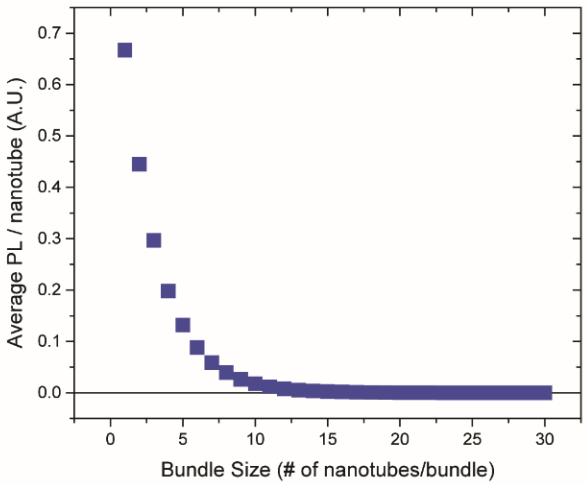

Figure 2-S5. We calculate the average PL per SWCNT as a function of bundle size. On average, most PL comes from bundles of size <5 nanotubes.

Calculation of average PL per nanotube as a function of bundle size.

Since we expect bundles to be of roughly the same composition of the starting material, we use a m-SWCNT concentration of 33.3%. On average, most PL comes from bundles of size <5 nanotubes. As the number of nanotubes in bundles increases, absorbance will increase, but PL will saturate due to

quenching of excitons photogenerated within the bundles. The average PL from a bundle is plotted in **Figure 2-S5** as a function of the number of nanotubes in each bundle.

Removing S_{33} contribution to photoluminescence.

Using the S_{22} and S_{33} relative optical cross sections of Liu et al.,[61] the S_{22} transition energies of Weisman et al.,[6] and the S_{33} transition energies of Haroz et al.,[60] we calculate the absorption profile of each chirality of SWCNT and compare the spectrum to the excitation spectrum extracted from the PLE maps. Most of the S_{33} transitions do not overlap with the measured peak PFO excitation at 380 nm, and only the (8,6) S_{33} has a significant overlap, and can be seen in **Figure 2-S6**. In the worst case for the lowest PFO loading, the magnitude of the S_{33} absorption compared to the magnitude of the PFO absorption, at the exciton wavelength of 380 nm, is 25%.

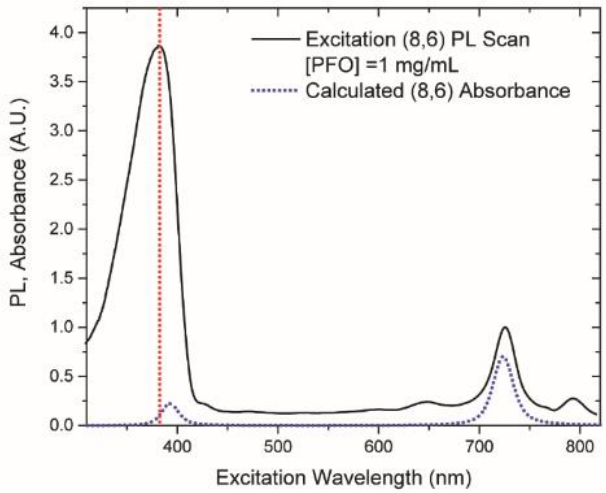

Figure 2-S6. A typical excitation spectrum for (8,6) nanotube, with the contribution from the (8,6) S_{33} transition (blue, dotted line) for comparison. At the peak PFO absorption, there is only very slight overlap with the S_{33}.

Determination of ratio of PFO:SWCNT from PLE maps.

We quantify the coverage and mass loading of PFO on SWCNTs, γ, by measuring the intensity of cross-peaks in the PLE maps. Excitation spectra are measured for emission at the SWCNT S_{11} of interest. Two prominent peaks are apparent in the excitation spectra (**Figure 2-2A**): one at the PFO absorption

maximum near 380 nm, with corrected intensity $PL_{corr}^{PFO\rightarrow S11}$, and the other at the S_{22} of the respective SWCNT, with corrected intensity$PL_{corr}^{S22\rightarrow S11}$.

Derivation of PL intensity corrected for self-absorption can be found in **Appendix C**. The relevant equation is given as **Equation 2-S3**.

$$PL_{corr} = PL_{meas}\frac{A_{ex}}{1-\exp(-L_x A_{ex})}\frac{A_{em}}{1-\exp(-L_y A_{em})}. \quad \textbf{[2-S4]}$$

where A_{ex} and A_{em} are the absorbance of the solution at the excitation and emission wavelengths, respectively, and L_x and L_y are the depths of the cuvette in the excitation (x) and emission (y) directions. According to Eq. S1,

$$PL_{corr}^{S22\rightarrow S11} = \varphi_{PL}^{S22\rightarrow S11}\varphi_{coll}c_{SWCNT}\sigma_{S22} \quad \textbf{[2-S5]}$$

where $\varphi_{PL}^{S22\rightarrow S11}$ is the quantum yield for the relaxation of an exciton from S_{22} to S_{11} followed by radiative emission, c_{SWCNT} is the concentration of SWCNTs at the S_{11} of interest in $g\cdot cm^{-3}$, and σ_{S22} is the S_{22} optical cross section, in $cm^2\cdot g^{-1}$. Likewise, according to Eq. S1,

$$PL_{corr}^{PFO\rightarrow S11} = \varphi_{PL}^{PFO\rightarrow S11}\varphi_{coll}c_{SWCNT}\gamma\sigma_{PFO} \quad \textbf{[2-S6]}$$

where $\varphi_{PL}^{PFO\rightarrow S11}$ is the quantum yield for energy transfer of an exciton from PFO to the SWCNT followed by radiative emission, σ_{PFO} is the PFO optical cross section, in $cm^2\cdot g^{-1}$, and γ is the loading of PFO on the SWCNTs in g PFO / g SWCNT.

Eq. S2 and Eq. S3 can be combined to eliminate c_{SWCNT} and solve for γ to yield the following expression:

$$\gamma = \frac{PL_{corr}^{PFO\rightarrow S11}}{PL_{corr}^{S22\rightarrow S11}}\frac{\sigma_{S22}}{\sigma_{PFO}}\frac{\varphi_{PL}^{S22\rightarrow S11}}{\varphi_{PL}^{PFO\rightarrow S11}} \quad \textbf{[2-S7]}$$

Thus, to calculate the mass loading, γ, we measure the ratio of the cross peaks $\frac{PL_{corr}^{PFO\rightarrow S11}}{PL_{corr}^{S22\rightarrow S11}}$. We used literature values of 2.5×10^5 cm^2·g^{-1} for σ_{PFO}[70] and $3.109, 2.707,$ and 2.256×10^5 cm^2·g^{-1} for σ_{S22}[56] of PFO-wrapped (7,5), (8,6), and (8,7) SWCNTs, respectively.

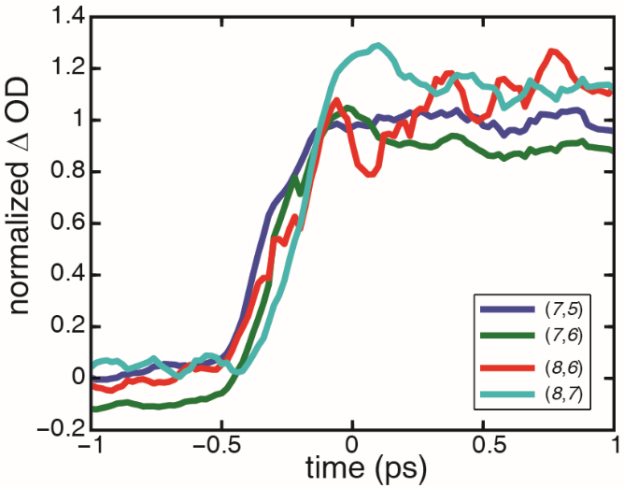

Figure 2-S7. Normalized change in optical density of four nanotube species in solution. The rise time for all are significantly shorter than the fluorescence lifetime of PFO, suggesting that energy transfer is very efficient from PFO to s-SWCNT.

Transient Absorbance.

The output of a Ti:Sapphire regenerative amplifier (800 nm, 150 fs, 1 kHz) is divided into two beams using the reflection from a piece of glass. The majority of the light, ~50 μJ, is focused into a 2 mm thick b-BBO crystal (Eksma) to generate ~1 μJ of 400 nm light. The residual 800 nm light is filtered out using a colored glass filter (Thorlabs). A white light supercontinuum is used as the probe. This is generated by focusing <1 μJ of the 800 nm fundamental into a 4mm thick YAG crystal (DeLn Optics). The pump probe time delay is controlled using a mechanical delay stage (Newport IMS400PP). We chop our pump pulse at 500 Hz using a mechanical chopper (New Focus 3501). Both beams are focused onto the SWCNT sample using a 12.5 cm focal length 30˚ off axis parabolic mirrors (Janos Technology). The probe spectrum is dispersed by a 150 mm focal length spectrometer (Acton SP-2150) and recorded with an InGaAs photodiode array (Princeton Instruments OMA-V:512-1.7). A spectral background for each time delay is fit to a third order polynomial and subtracted.

Energy Transfer Efficiency.

We estimate the PFO-SWCNT energy transfer efficiency using ultrafast transient absorption spectroscopy. We excite the PFO at 400 nm and probe the transient absorption profile at the S_{11} of each chirality of SWCNT. The rise time for each nanotube species is less than 500fs, which is roughly the resolution of the measurement, and is independent of (*n*,*m*). The known fluorescence lifetime of PFO is 410ps, implying that the energy transfer efficiency is on the order of

$$\eta = 1 - \frac{\tau_{CNT}}{\tau_{PFO}} = 1 - \frac{0.5ps}{410ps} > 0.99 \qquad \textbf{[S5]}$$

Therefore, in the main text we use an energy transfer efficiency of 1.00, and a subsequent relaxation efficiency to S_{11} of 0.80 to yield an overall value of $\varphi_{PL}^{PFO \to S11} = 0.80$. We plot γ as a function of the PFO concentration in **Figure 2-S8**.

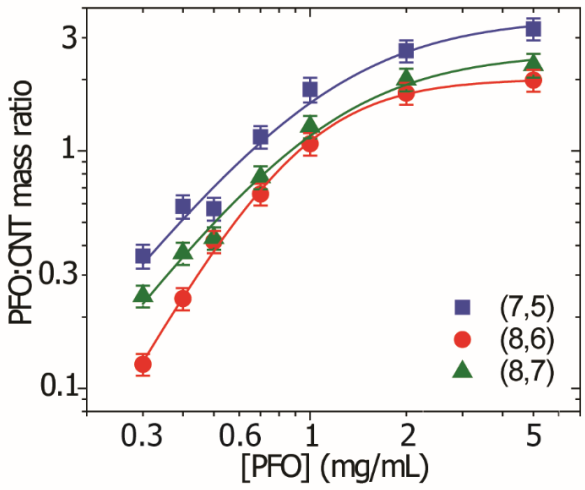

Figure 2-S8. The relative mass loading of PFO on carbon nanotubes (7,5), (8,6), (8,7) is displayed as a function of PFO concentration. The loading saturates at high PFO concentration and follows a Langmuir adsorption isotherm with competitive binding.

PFO:CNT Mass Ratio.

We fit the data to the Hill Equation[65]

$$\gamma = \gamma_s \left[\left(\frac{K_A}{[PFO]}\right)^n - 1\right]^{-1} \quad \textbf{[2-S9]}$$

where γ_s is the saturated mass ratio, corresponding to full coverage, and extract the constants K_A and n. The plot in the text **Figure 2-2B** is the coverage θ, defined here to be

$$\theta = \frac{\gamma}{\gamma_s} = \left[\left(\frac{K_A}{[PFO]}\right)^n - 1\right]^{-1} \quad \textbf{[2-S10]}$$

As we noted above, γ_s is dependent on the values we choose for $\varphi_{PL}^{PFO\rightarrow S11}$ and $\varphi_{PL}^{S22\rightarrow S11}$. Importantly, K_A and n are unchanged upon varying $\varphi_{PL}^{PFO\rightarrow S11}$ and $\varphi_{PL}^{S22\rightarrow S11}$. This is due to the fact that K_A and n depend only on the *shape* of the curve, and γ_s is essentially a scaling factor with no impact on the curve shape.

Fluorescence Anisotropy & Wrapping Angle.

The fundamental fluorescence anisotropy $\langle r \rangle$ is given by

$$\langle r \rangle = \frac{1}{5}\left(3\cos^2\delta - 1\right) \quad \textbf{[2-S11]}$$

Where δ is the angle between excitation and emission dipoles. Then, solving for δ,

$$\delta = \cos^{-1}\sqrt{\frac{5\langle r \rangle + 1}{3}} \quad \textbf{[2-S12]}$$

Since the angle δ is the sum of the angle α between the polymer backbone and the nanotube long axis and angle β between the polymer backbone and the polymer excitation dipole, then the nanotube wrapping angle is given by

$$\alpha = \delta \pm \beta = \cos^{-1}\sqrt{\frac{5r_0 + 1}{3}} \pm \beta \quad \textbf{[2-S13]}$$

The value of β is known to be between 21 and 26° from literature[66-67]. Since δ is in general fairly large, on the order of 40°, α can take on values of <20° or >60°. The required curvature necessary for PFO to wrap at 60° excludes this result as unphysical; therefore, we take the value $\alpha = \delta - \beta$. We calculate the average wrapping angle α as a function of [PFO] in **Figure 2-S9** from the measured $\langle r \rangle$ data in the main text.

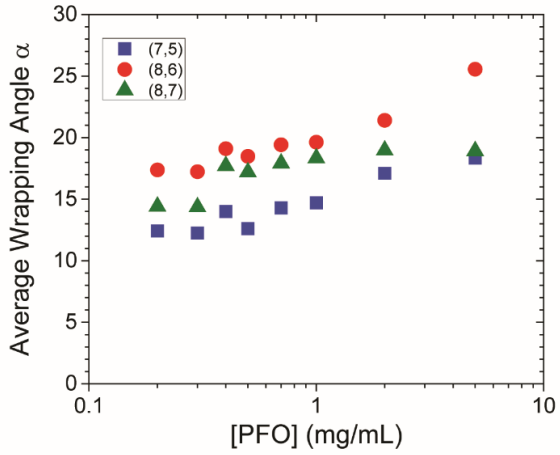

Figure 2-S9. We calculate the average wrapping angle $\boldsymbol{\alpha}$ from the measured $\langle \boldsymbol{r} \rangle$ using **Equation 2-S13** for each of the nanotubes as a function of [PFO].

CHAPTER 3: 1% SOLAR CELLS DERIVED FROM ULTRATHIN CARBON NANOTUBE PHOTOABSORBING FILMS

Adapted from:

Shea, M. J.; Arnold, M. S., 1% Solar Cells Derived from Ultrathin Carbon Nanotube Photoabsorbing Films. *Appl. Phys. Lett*. **2013**, *102*, 5.

The author contributed the entirety of the work.

CARBON NANOTUBE PHOTOVOLTAICS

Semiconducting single-walled carbon nanotubes are promising light absorbers for photovoltaics due to their tunable bandgaps,[5] strong optical absorptivity in the near-infrared (NIR),[71] fast exciton and charge transport,[4] solution-processability, and the potential for chemical and thermal stability.[3] There has already been extensive work on incorporating carbon nanotubes into polymer and hybrid photovoltaic devices in optically passive roles as electrode materials[72-74] and as materials to aid in charge collection or transport.[75-79] However, exploiting the optical absorptivity of carbon nanotubes in photovoltaic devices has been more difficult, requiring the use of electronically type-sorted, semiconducting nanotubes to avoid exciton quenching by metallic nanotube species and necessitating a means to overcome the nanotube exciton binding energy.[15] Bindl et al. have recently overcome these challenges and shown that excitons can be efficiently harvested from type-controlled semiconducting carbon nanotube films by dissociating the excitons into free charge carriers using donor / acceptor heterojunction schemes.[80] An internal quantum efficiency (QE) for exciton dissociation and charge separation of > 80% is achieved using C_{60} fullerenes as photoexcited electron acceptors. Other schemes for harvesting excitons from nanotubes have been implemented in preliminary photovoltaic devices.[49, 51, 81-83] However, thus far, the photoresponse of those devices has still arisen mostly from the non-nanotube components, with only limited success in exploiting either the visible or near-infrared nanotube absorptivity for driving solar power conversion.

In order to further increase the photoresponsivity arising from the nanotubes, Bindl et al. has explored the optimization of the nanotube bandgap distribution and achieved an external QE as high as 34% at the nanotube bandgap by using more monodisperse nanotubes. Here, we extend this optimization, using even more monodisperse nanotubes, further increasing the external QE arising from the nanotubes, and fully optimize layer thickness and optical interference effects to demonstrate for the first time solar cells with > 1% power conversion efficiency in which the photoresponse arises predominantly from the nanotube component.

DEVICE FABRICATION AND EVALUATION

In our approach, we extract (7, 5) semiconducting nanotubes from a powder of small diameter (0.7-1.2 nm) nanotubes (Southwest Nanotechnologies, Lot# SG65i-L38) derived from cobalt molybdenum catalysis of carbon monoxide disproportionation (CoMoCAT). The (7, 5) species are isolated by dispersing the powder in a solution of poly(9,9-dioctylfluorene-2,7-diyl) (PFO) in toluene using a procedure adapted from that of Nish et al.[7] The excess PFO is removed by repeated sedimentation and redispersion in tetrahydrofuran, until a solution of less than 2:1 (w/w) PFO:nanotubes is obtained, which is then dispersed in chlorobenzene. Removal of excess PFO from the nanotube solution has been shown to increase the nanotube QE.[84]

Optical absorption spectra of the nanotubes in solution (diluted for measurement to 2 ng mL^{-1}) and in a film (thickness approximately 7 nm) deposited by doctor-blade casting are compared in **Figure 3-1A**. The strongest peak at 1055 nm corresponds to the first optical excitation (S_{11}), e.g. the bandgap excitation of the (7, 5) chirality, with minor contributions from the S_{11} of (6, 5), (10, 2), (7, 6), and (8,6) nanotubes at 1000, 1090, 1150, and 1200 nm, respectively. The peak at 655 nm corresponds to the second optical excitation (S_2) of the (7, 5) nanotube, with minor contributions from the S_2 of the (6, 5) and (7, 6) nanotubes. The features from 300 – 450 nm are due to a combination of PFO absorption and the third optical excitation (S_3) of the nanotubes. Importantly, the spectrum is free of metallic nanotube peaks near 500 nm. Metallic nanotubes provide exciton quenching sites and are expected to drastically decrease the performance of

nanotube photovoltaic devices.[17] We used the S_{11} oscillator strength chirality dependence predicted by Ando[85] to determine that (7, 5) nanotubes make up greater than 90% of nanotubes present. The broadening of transitions from solution to film is consistent with previous investigations.[80]

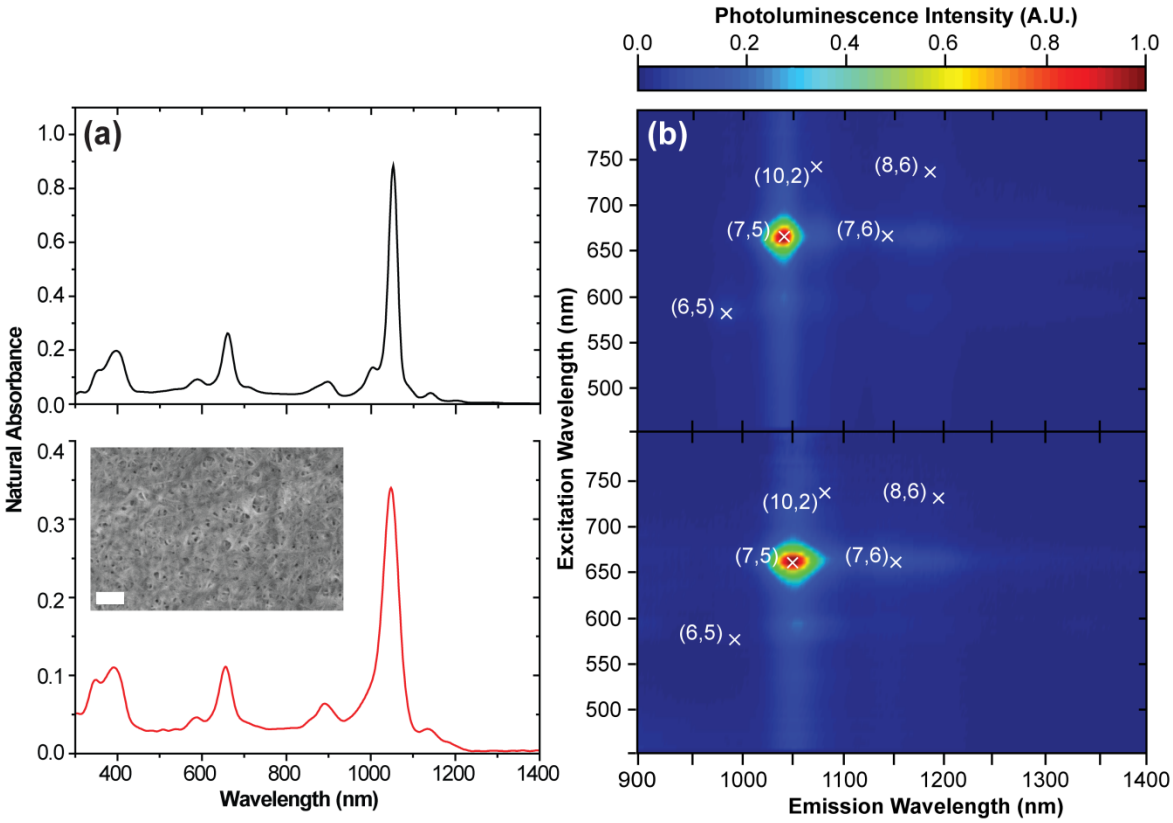

Figure 3-1. (A) Absorbance of solution (black, top) and approximately 7 nm thick film on ITO-coated glass (red, bottom). The strong peak at 1055 nm indicates nearly monochiral (7, 5) nanotubes. Inset: Scanning Electron Micrograph of a (7, 5) nanotube film on ITO-coated glass. Scale bar is 100 nm. (b) Intensity of photoluminescence from solution (top) and film (bottom) on quartz as a function of excitation and emission wavelengths. The strong, narrow peak at (1055, 660) is indicative of nearly monochiral (7, 5) nanotubes, with small contributions by (6, 5) (1000, 570), (10, 2) (1090, 740), (7, 6) (1150, 670) and (8, 6) (1200, 710) apparent in the solution photoluminescence. The photoluminescence arising from film exhibits limited exciton energy transfer, most prominently from (6, 5) to (7, 5) at (1050, 590), and from (7, 5) to (7, 6) and (8, 6) at (1200, 655).

Photoluminescence excitation emission maps (Horiba NanoLog iHR 320) are also measured to confirm the nanotubes' isolation in solution and the degree of coupling in thin film (**Figure 3-1B**). In solution, photoluminescence emission predominantly arises from the (7, 5) nanotube, consistent with the degree of monochirality observed in the absorption spectra. The absence of cross-peaks leads us to conclude

that the nanotubes are well-dispersed, with insubstantial exciton transfer between nanotubes. In a film of thickness approximately 7 nm, there is limited exciton energy transfer between nanotubes, predominantly from the (6, 5) excitation to the (7, 5) emission, corresponding to the peak at (1055 nm, 575 nm). Also evident is weak energy transfer from the (7, 5) nanotube to larger diameter, smaller bandgap nanotubes, predominantly (10, 2), (7, 6), and (8, 6). We note that the trapping of excitons on small bandgap nanotubes is expected to have a negative impact on short-circuit current density (J_{SC}), open-circuit voltage (V_{OC}), and power conversion efficiency (η_P).[17] Thus, limiting the concentration of small bandgap nanotubes even further than that which has been achieved here will be important in future work.

The bilayer heterojunction devices are fabricated on UV-ozone treated, solvent-cleaned indium tin oxide (ITO)-coated glass substrates (15 Ω/□, Prazisions Glas & Optik) as described in more detail elsewhere.[80] The nanotubes are deposited via doctor-blade casting, in which an 8 μL droplet of nanotube solution is placed on an ITO substrate on a hotplate set to 110 °C and a steel blade is drawn across the substrate approximately 500 μm above the surface. The process is repeated two to six times to tailor the film thicknesses, and the films are subsequently annealed at 110 °C for 1 hour in N_2 atmosphere (< 1 part per million O_2 and H_2O) to remove excess solvent. The nanotubes form fibers 5 – 10 nm in diameter, lying parallel to the substrate and are interwoven throughout each other. A layer of C_{60} of tailored thickness is thermally evaporated (10^{-7} Torr background pressure) on top of the nanotube film. Bathocuprione (BCP) of thickness 10 nm and a 100 nm silver electrode are evaporated as the cathode. The active area of each device defined by the cathode is 0.785 mm^2.

In order to maximize the photoresponse arising from the nanotubes in the device stack, we optimize the thickness of the C_{60} layer ($t_{C_{60}}$) and of the nanotube layer. To assess the separate contributions of the nanotubes and the C_{60} to the photocurrent during the optimization, we measure the zero-bias external quantum efficiency (QE) as a function of wavelength using a calibrated monochromatic light source from 375 to 1300 nm. The main effect of varying $t_{C_{60}}$ is to alter optical interference within the device stack. Because the nanotube layer is thin and the dominant internal reflection is at the BCP/Ag interface, we can

closely approximate the interference at the nanotube/C_{60} heterointerface, where excitons are most efficiently harvested, using the procedure of Peumans *et al.*[86] We expect the photoresponse to be maximized at the S_{22}, S_{11}+X, and S_{11} transition when $t_{C_{60}}$ is in the range of 40 – 60 nm, 60 – 80 nm, and 80 – 100 nm, respectively.

Based on these guidelines, we fabricate actual heterojunction diodes with $t_{C_{60}}$ = 50, 70, and 86 nm and measure the external QE. The peak external QE at the S_{11} transition of the (7, 5) nanotube at 1055 nm increases from 22.1% to 34.0% to 43.5% as $t_{C_{60}}$ increases from 50 to 70 to 86 nm, respectively (**Figure 3-2**). The peak external QE of 43.5% for the device with $t_{C_{60}}$ = 86 nm is to our knowledge the highest reported nanotube external QE in any device. The external QE at the S_2 transition at 650 nm concurrently decreases from 19.0% to 12.5% and 7.6%, respectively. The external QE at the S_{11} + phonon transition is 8 – 10% for all three devices. The C_{60} response is broad from 375 nm to its cutoff near 650 nm, with peak external QE near 30% for all three devices. These trends are consistent with that predicted by the interference model.

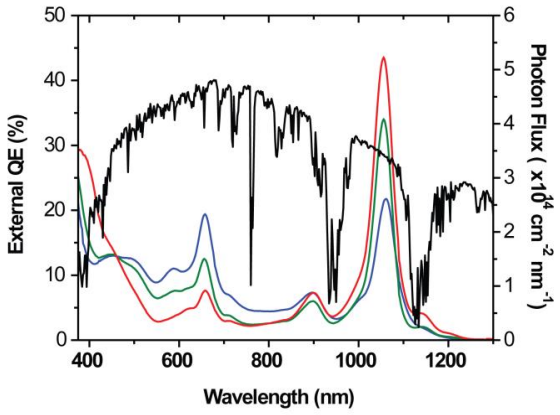

Figure 3-2. External QE from nanotube/C60 device stacks with C_{60} thickness of 50 nm (blue), 70 nm (green) and 86 nm (red) compared to the AM1.5G photon flux (black). The external QE is modulated by the optical interference and depends strongly on C60 thickness.

The J_{SC} driven by the nanotube/C_{60} device stacks under solar irradiation can be predicted by integrating the product of the external QE and the solar photon flux. We separately quantify the contribution

to J_{SC} by the nanotubes and the C_{60} by comparing the external QE spectra of the nanotube/C_{60} devices with equivalent devices lacking a nanotube film. The external QE at 380 nm mostly arises from the C_{60}. A peak external QE of 8.7% at 380 nm is achieved with the architecture ITO/C_{60}/BCP/Ag compared with nearly 29% at the same wavelength in our best nanotube/C_{60} device. This discrepancy is due to a decrease the efficiency at which excitons photogenerated in the C_{60} layer are dissociated and harvested in the absence of the nanotube film, which acts as a hole acceptor for the photoexcited C_{60}. Scaling the external QE spectrum from the C_{60}-only device and subtracting it from the nanotube/C_{60} external QE spectrum yields the contribution from the nanotubes, alone, which is then used to estimate the nanotube contribution to J_{SC}. This contribution is a conservative lower-bound due to neglecting the nanotube S_3 transition and the possibility of over-estimating the C_{60} contribution to the photocurrent in the ultraviolet/visible spectrum.

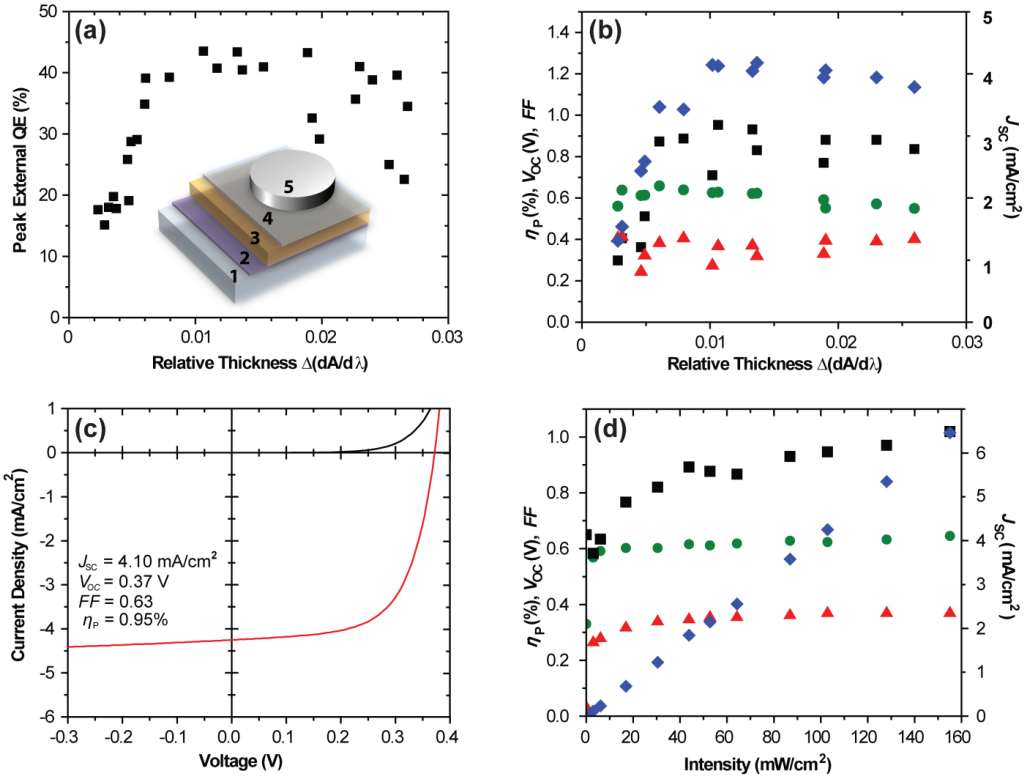

Figure 3-3. (A) Optimization of external QE at λ = 1055 nm as a function of the relative thickness of the nanotube layer. Inset: Device Architecture: (1) ITO-coated glass; (2) (7, 5) nanotube film; (3) C_{60}; (4) BCP; (5) Ag. **(B)** Optimization of AM1.5G photovoltaic parameters J_{sc} (blue diamonds), V_{oc} (red triangles), *FF* (green circles), and η_P (black squares) at 1.0 sun as a function of the relative thickness of the nanotube layer. **(C)** Current density – voltage curves from the device exhibiting maximum power conversion efficiency in

part **(B)** in the dark (black) and under AM1.5G 100mW cm^{-2} illumination (red). **(D)** Photovoltaic parameters, using the same symbols as **(B)**, adjusted for and plotted against corresponding AM1.5G intensity. η_P = 0.95% and 1.02 % at 1.0 and 1.5 suns, respectively.

According to this analysis, the expected total J_{SC} under 1 sun AM1.5G is 4.11 mA cm^{-2}, 4.09 mA cm^{-2}, and 4.21 mA cm^{-2} as the C_{60} thickness is increased from 50 to 70 to 86 nm and the fraction of J_{SC} arising from nanotube excitons increases from 53% to 58% to 63%, respectively. We therefore use $t_{C_{60}}$ = 86 nm in our devices in order to maximize the fraction of J_{SC} from the nanotubes and to maximize the total J_{SC}. Unlike other devices[49, 51, 81-82] in which the carbon nanotube photoresponse has been secondary to other materials and less efficient, here the photoabsorption by the nanotube phase is responsible for the majority (63%) of the power conversion.

At a fixed $t_{C_{60}}$ = 86 nm, we also optimize the nanotube film thickness, which we quantify by measuring the optical density of the nanotube film in transmission. The peak external QE at the (7, 5) bandgap of 1055 nm at first increases but then decreases with nanotube film thickness, with a maximum at an optical density corresponding to a film thickness of roughly 5 nm (**Figure 3-3A**). The shape of the external QE versus thickness curve can be understood by considering intra- and inter-nanotube diffusion-limited exciton transport and optical losses.[80, 84] We also determine the photovoltaic parameters under a simulated solar spectrum, as a function of nanotube film thickness (**Figure 3-3B**). A custom 2-source solar simulator is used, which better reproduces the solar spectrum in the near-infrared than a single Xe lamp. The J_{sc}, η_P, (**Figure 3-3B**) and the external QE (**Figure 3-3A**) are all maximized at a similar nanotube thickness. Generally, the fill-factor (*FF*) decreases with nanotube thickness while no clear trend in V_{oc} is observed.

We further characterize the device at the peak of the η_P distribution of **Figure 3-3B**, in **Figures 3-4C-D**. The current–voltage characteristics in the dark and under 100 mW cm^{-2} simulated solar illumination are shown in **Figure 3-4C**. In the dark, the devices are diodes with rectification greater than 10^5 at ±1 V. The photovoltaic parameters, corrected to the AM1.5G spectrum, are characterized as a function of intensity in **Figure 3-3D**. The J_{SC} is linear with incident power, indicating that our devices are not series resistance-

limited in this irradiance range. The V_{OC} reaches 92% of its 1 sun value at 30 mW cm^{-2}, and the *FF* is relatively independent of intensity greater than 10 mW cm^{-2}. At 1.0 sun, J_{SC} = 4.10 mA/cm^2, V_{OC} = 0.370 V, *FF* = 0.63, and the AM1.5G η_P = 0.95%. At 1.5 sun, J_{SC} = 6.40 mA/cm^2, V_{OC} = 0.380 V, *FF* = 0.65, and the AM1.5G η_P = 1.02%. The integrated external QE – AM1.5G intensity product predicts a J_{SC} = 4.20 and 6.50 mA/cm^2 under 1.0 and 1.5 suns, respectively, which are both within 2.0% of the measured and then corrected J_{SC}, confirming the validity of the correction. In comparison, Bindl et al.[34] did not directly measure an AM1.5G η_P. However, we estimate an AM1.5G η_P of 0.70% by spectrally correcting their external QE spectra and monochromatic power dependencies. Thus, we see a >35% increase in η_P by improving the isolation of (7,5) nanotubes and optimizing optical interference within the device.

To better make the point that the majority of the power conversion arises from nanotube photoabsorption in this work, we introduce a figure of merit, the nanotube-contributed power conversion efficiency, $\eta_{P,CNT}$, by multiplying the overall AM1.5G power conversion efficiency by the fraction of J_{SC} arising from nanotube absorption. $\eta_{P,CNT}$ = 0.60% and 0.64% at 1.0 and 1.5 suns, respectively, as compared to < 0.13% in other implementations.[49, 51, 81-82] It is also worthwhile to note that the peak η_P occurs near the linear regime of external QE versus nanotube film thickness, which suggests an internal QE within the nanotube layer on the order of 85% in accordance with Bindl et al.[34]

In summary, we show that due to their strong optical absorptivity, we can use a film of semiconducting carbon nanotubes that is < 5 nm in thickness to drive meaningful photovoltaic power conversion. By implementing highly monochiral (7, 5) nanotubes, optimizing the nanotube film thickness, and tailoring optical interference effects in the device stacks, we achieve an external QE as high as 43% at the nanotube bandgap at λ = 1155 nm and a AM1.5G solar power conversion efficiency of 0.95% and 1.02% at 1.0 and 1.5 suns, respectively. The nanotube photoabsorption drives > 60% of the power conversion. At the time of publication this work represents the highest external QE, largest fraction of nanotube-contributed J_{SC}, and the highest $\eta_{P,CNT}$ that has been reported, thus far. The high internal QE suggests that substantial improvements in efficiency will be possible by nanostructuring the heterojunction or

implementing multiple layers to harness photoabsorption from more nanotube material and by better controlling the anisotropy and dynamics of exciton migration.

SUPPORTING INFORMATION

SWCNT processing.

Poly(9,9-dioctyl-fluorene-2,7-diyl) (PFO) was purchased from American Dye Source (ADS329BE Lot#12J046A1) and dissolved in toluene (Fisher Scientific, ACS grade) at the concentration of 2 mg/mL while stirring at 80°C. Nanotubes were purchased from Southwest Nanotechnologies (Lot#SG65i-L38) and mixed with the PFO solution in the ratio of 50 mg nanotubes : 50 mL PFO solution. 20 mL of fresh toluene was added to avoid gelling of the nanotubes during sonication. The 70 mL of raw nanotube solution was sonicated using a Fisher sonic dismembrator model 500 horn sonicator (400 Watts) at 40% amplitude for 30 minutes. The resulting dispersion was divided into six equal aliquots in ThermoFisher polyalomer centrifuge tubes and centrifuged in a ThermoFisher WX Ultra series centrifuge at 41,000 rpm (300,000 g) for 1 hour. The top 80% of supernatant from each centrifuge tube was collected and filtered through a Millex SV 5 µm PTFE filter. The entire process was repeated 8 times to attain roughly 450 mL of supernatant. The combined supernatant was placed in a 500 mL round-bottom flask and was distilled under vigorous stirring using a custom vacuum line at room temperature, in which the distilled toluene was collected in a second flask held at 77K in liquid nitrogen. The resulting powder was green-blue in color and contained PFO and aggregated but PFO wrapped nanotubes. This powder was dissolved in 20 mL of boiling tetrahydrofuran (THF) and stirred until transparent. Upon cooling, nanotubes precipitated out of the solution, as evidenced by dark blue wispy solids in the green solution. The hot solution was immediately pipetted into Nalgene Oak Ridge teflon centrifuge tubes and centrifuged at 25,500 rpm (50,000 g) at 4 °C for 3 hours. After this time, the supernatant, containing dissolved PFO, was drawn off. The nanotubes were collected and dispersed in THF by micro-tip sonication at 10% amplitude, reheated until the solution was transparent, and centrifuged for 3 hours. This process was repeated an additional two times, until the

supernatant was clear and colorless. The nanotubes were collected and dispersed in 1 mL of chlorobenzene using the microtip at 10% amplitude. The resulting concentration of nanotubes was about 0.1 mg/mL. Finally, immediately before use, the nanotube solution was centrifuged for 15 minutes at 17,500 rpm (30,130 g) in an Eppendorf 5430 centrifuge and the supernatant was collected and sonicated for 1 minute using the microtip at 10% amplitude before doctor-blading of films.

Quantifying nanotube solution chirality composition.

We used the oscillator strength calculations of Ando et al. and the measured optical absorption cross section for the (6,5) nanotube to estimate the chirality distribution in our nanotube solutions in chlorobenzene. Table I below contains the relative oscillator strength, the calculated optical absorption cross section, and the peak height and full width half maximum for each nanotube peak in the absorption cross section, after a linear background subtraction. We estimate 6.9%, 90.4%, 1.2%, 1.2%, and 0.3% composition, by weight, for (6,5), (7,5), (10,2), (7,6), and (8,6) nanotubes, respectively.

Quantifying nanotube film thickness.

In order to estimate nanotube film thickness, the absorbance of the film was measured and the derivative $dA/d\lambda$ was calculated. The derivative of the absorption has a minimum and maximum on either side of the nanotube S_{11} absorption peak at 1055 nm. At constant spectral width, the positive difference of the maximum and minimum, denoted $\Delta(dA/d\lambda)$, is proportional to the thickness and independent of a linear background. This allows the determination of the thickness of nanotubes. We measured the thickness of a nanotube film with $\Delta(dA/d\lambda) = 0.03$ to be 10 nm via profilometry, and extrapolated this result to estimate the actual thickness of the nanotube films in our devices. The relative thickness $\Delta(dA/d\lambda) = 0.01$ associated with the peak of the QE versus $\Delta(dA/d\lambda)$ plot (**Figure 3-4A**) is equivalent to a < 5 nm thick film. The film pertaining to the absorbance and photoluminescence data in **Figure 3-1** has relative thickness 0.01 and a calculated absolute thickness 6 –7 nm.

Optical Modeling of Devices.

To model optical interference within the device stacks, we used the optical transfer matrix approach of Peumans et al. and literature optical constants for ITO, C60, BCP, and silver. For a given device architecture, we calculated optical intensity as a function of wavelength within the device stack. We approximated the optical intensity within the nanotube layer of our actual devices by modeling an architecture consisting of ITO / C60 / BCP / Ag. Using a nanotube-less model is necessary because the optical constants of highly monochiral nanotubes have not yet been fully determined. With this said, the nanotube-less models are excellent approximations to the real devices because our nanotube films are so extremely thin. The optical intensity at the nanotube film (determined at the ITO / C60 interface in our models) is overlaid with external QE in **Figure 3-S1**. The optical intensity is maximized near the E11, E11+phonon, and E22 transitions for 80-100 nm, 60-80 nm, and 40-60 nm, respectively, in the models, closely matching experiment.

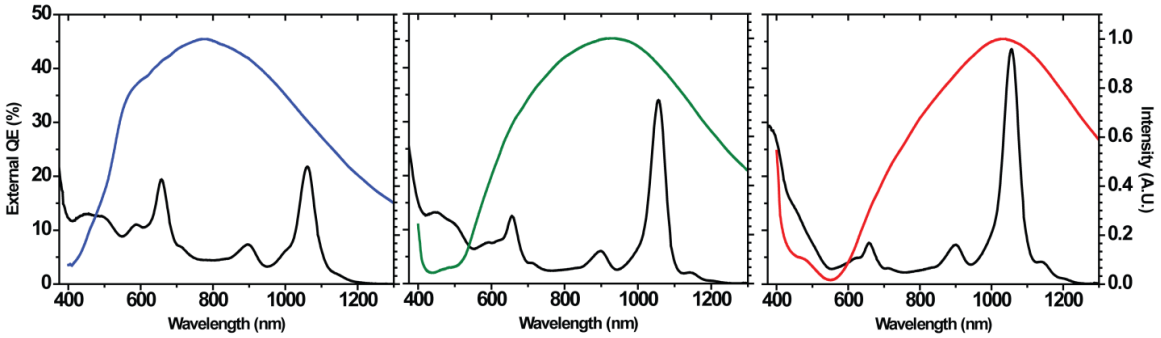

Figure 3-S1. External QE of (7, 5) – C_{60} devices with varying C_{60} thickness (a) 50 nm, (b) 70 nm, (c) 86 nm compared to the model of the electric field intensity as a function of wavelength in the nanotube film. Changing the C_{60} thickness modulates the optical interference within the device stack, and changes the contribution from S_{11} and S_{22}.

Calculation of nanotube-contributed J_{SC}.

To compare our data to other work, we formulated a measure of the contribution of nanotubes to JSC, and by extension, ηP. We estimated the contribution of C60 in our devices by overlaying the nanotube/C60 external QE spectrum with the scaled C60-only devices from 540 nm to 800 nm, as shown in **Figure 3-S2**. We applied the conservative assumption, neglecting the nanotube E33 transition

contribution, that nearly all the external QE below 540 nm was due to C60. Multiplying this spectrum by the solar photon flux, we were able to estimate JSC arising from the nanotubes, alone. In analyzing other devices from literature, we either used the given estimation of nanotube external QE or estimated external QE arising from nanotubes along similar parameters to our own. These spectra are compared in **Figure 3-S3**. We subtracted the non-nanotube component from the external QE spectrum to estimate the nanotube contribution to J_{SC}.

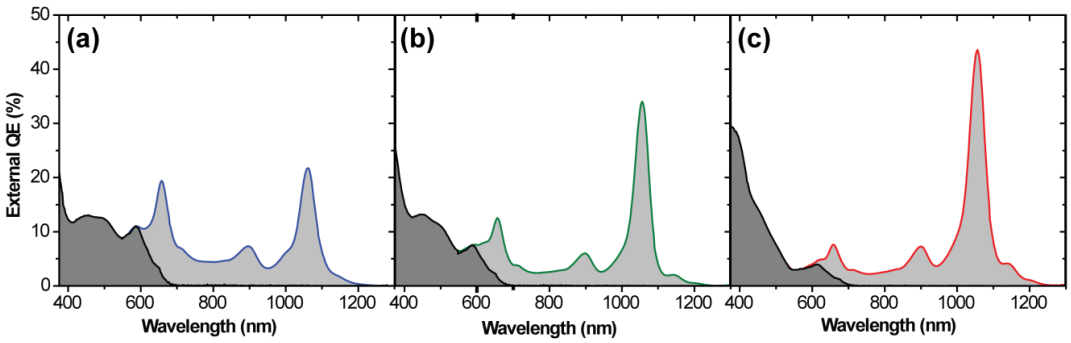

Figure 3-S2. External QE of (7, 5) – C_{60} devices from nanotubes (light grey) and C_{60} (dark, hashed) as a function of C_{60} thickness of (a) 50 nm, (b) 70 nm, (c) 86 nm. Increasing the C_{60} thickness increases the proportion of nanotube-contributed J_{SC} from 53% to 58% to 63%, respectively.

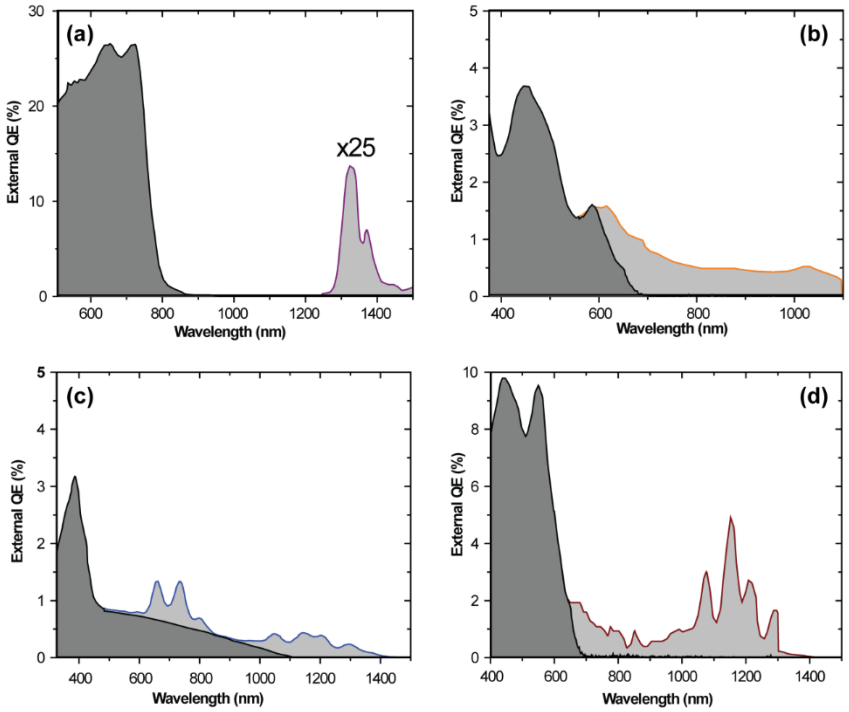

Figure 3-S3. The nanotube-contributed (light grey) external QE spectra of previously reported nanotube devices compared to the non-nanotube contribution (dark grey hashed) from **(A)** the P3HT-nanotube devices reported by Ren et al.[82] **(B)** aqueous-processed (6, 5)-C_{60} devices reported by Jain et al.[81] **(C)** silicon nanocrystal-nanotube devices reported by Sverck et al.[51] and **(D)** C_{60}-nanotube devices reported by Ramuz et al.[49]

Solar Simulator.

A custom 2-source solar simulator was constructed using a tungsten lamp as a visible/near-infrared source and a Newport xenon arc-discharge lamp as an ultraviolet/visible source. The xenon source was filtered by a KG5 colored glass filter to remove the emission lines from xenon above 800 nm and combined with the tungsten source using a 50/50 beamsplitter. The relative magnitude of the xenon contribution was controlled by an iris, and the resulting spectrum, shown in **Figure 3-S3** was measured using a monochrometer and a Newport 818-UV calibrated detector. The efficiency of the monochrometer and optics was measured using an AvaLight-HAL-CAL calibrated light source. The intensity of the beam was measured using the Newport 818-UV calibrated detector with a calibrated 3 OD attenuator, and an Abet Technologies RR-176-O NIST-calibrated silicon solar cell.

Spectral Correction.

The photovoltaic parameters of the device were measured under our simulated solar spectrum (**Figure 3-S4**) and then corrected to the AM1.5G spectrum using the procedure of Osterwaald.[87] A spectral mismatch factor *M* is defined as a function of the simulated spectrum E_{SIM}, the solar spectrum E_{REF}, the measured responsivity of the reference silicon cell R_{RC}, and the measured responsivity of the device R_{UN}:

$$M = \frac{\int_a^b E_{SIM}(\lambda)R_{RC}(\lambda)d\lambda \int_a^b E_{SIM}(\lambda)R_{UN}(\lambda)d\lambda}{\int_a^b E_{REF}(\lambda)R_{RC}(\lambda)d\lambda \int_a^b E_{REF}(\lambda)R_{UN}(\lambda)d\lambda} \quad \textbf{[3-S1]}$$

Then, the current density of the unknown device under solar illumination $J_{UN_{REF}}$ may be calculated as a function of the current density of the unknown device under the simulated spectrum $J_{UN_{SIM}}$ of the reference cell under simulated spectrum $J_{RC_{SIM}}$ and of the reference cell under solar spectrum $J_{RC_{REF}}$.

$$J_{UN_{REF}} = \frac{J_{UN_{SIM}} J_{RC_{REF}}}{M \cdot J_{RC_{SIM}}} \quad \textbf{[3-S2]}$$

A value of *M* close to unity signifies good spectral simulation. A representative value of *M* from our dataset is 0.93. After determining the corrected J_{SC}, the *FF* and V_{OC} at an equivalent current density were interpolated from the measured *FF* and V_{OC} versus J_{SC} under the simulated spectrum.

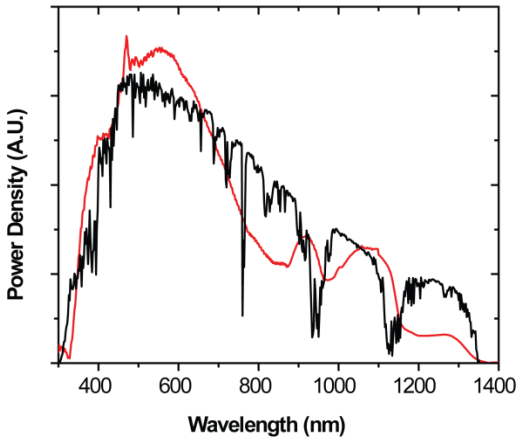

Figure 3-S4. Comparison of power density of the simulated spectrum (black) to AM1.5G solar spectrum (red).

CHAPTER 4: ENERGY OFFSET AND TRAP-LIMITED RECOMBINATION AT THE CARBON NANOTUBE/C_{60} HETEROJUNCTION

Adapted from:

Shea, M.J., Wang, J., Arnold, M.S., Trap-Limited Recombination and Energy Offsets at the Carbon Nanotube-C_{60} Heterointerface, *Journal of Physical Chemistry C, In Submission*

The author conceived of and carried out all experiments and data analysis. The author thanks Jialiang Wang for his preparation of the (7,5)-enriched carbon nanotubes used in this study.

Despite the considerable research into s-SWCNT/C_{60} devices, several challenges remain. The current-voltage curves are not easily fit to the traditional modified Shockley diode equation under all conditions, and the specific recombination mechanisms at the s-SWCNT/C_{60} interface are unknown. In addition, the energy gap between the s-SWCNT highest occupied molecular orbital (HOMO) and C_{60} LUMO, ΔE_{HL}, is a vital parameter for modeling the maximum open-circuit voltage (V_{OC}) attainable and is presently unmeasured. Observations of carbon nanotubes at cryogenic temperatures to date have been mostly limited to photoluminescence[88-90] and charge transport studies.[4, 91] Here, we explore the electronic properties of the s-SWCNT / fullerene heterojunction at low temperatures to discern the physical processes occurring in photovoltaic cells incorporating these materials.

MEASUREMENTS AT CRYOGENIC TEMPERATURE

s-SWCNTs are purified using a method modified from Nish et al.,[7] in which the aromatic polymer poly(9,9-dioctylfluorene-2,7-diyl) selectively wraps semiconducting SWCNTs from a mixture of semiconducting and metallic SWCNTs. CoMoCat-grown SWCNT soot (Sigma, SG65i) (0.5 mg mL^{-1}) is dispersed in a solution of PFO in toluene (1 mg mL^{-1}) using a horn-tip ultrasonicator (Fisher model 500, 400W) at 40% amplitude for 20 minutes. The SWCNT-polymer slurry is centrifuged at 300,000g for 10 minutes and the top 90% of the supernatant is extracted and set aside. The pellet, consisting of unwrapped or poorly wrapped SWCNTs, is discarded. The supernatant is rotary-evaporated to concentrate it, and

subsequently centrifuged again at 180,000g for up to 24 hours to remove excess polymer. The s-SWCNTs, collected in a pellet at the bottom of the centrifuge tube, are dispersed into tetrahydrofuran using the ultrasonicator at low (10%) amplitude briefly (typically <1 min). The dispersed s-SWCNT solution is centrifuged again, and these steps are repeated several more times, until the ratio of the PFO absorbance peak at 380 nm to s-SWCNT S_{22} transition is nearly 1:1 (corresponding to approximately 50 wt%).[84] Finally, the s-SWCNTs are dispersed in ortho-dichlorobenzene at a concentration of approximately 50 μg mL^{-1}.

Patterned indium tin oxide (ITO)-coated glass substrates (Thin Film Devices, Inc., 15 Ω/square) are cleaned in successive baths of acetone, trichloroethane, and isopropanol, and exposed to UV-ozone for 10 minutes. Immediately, the s-SWCNT solution is spin-coated on the ITO at 2,000 rpm to form a thin uniform film. Thicker films are formed by blade-casting, in a process similar to our previous work.[14] We especially focus on films with sub-monolayer coverage, with s-SWCNT fibers spanning regions of bare ITO. A representative scanning electron micrograph is shown in **Figure 4-1A.** We choose to focus on devices fabricated from very thin films of s-SWCNTs (sub-monolayer) to eliminate effects of exciton diffusion in thicker films and to therefore facilitate understanding of charge recombination and band offsets.[14, 80] After deposition, the substrate is placed in a bath of hot toluene at 120°C for 1 hour to remove unbound PFO or other contaminants from the film, and blown dry under N_2. Fullerene-C_{60} of thickness 60 nm is evaporated at 10^{-7} torr in an Angstrom Amod thermal evaporator, followed by 10 nm of bathocuproine as an exciton barrier and protective layer. 120 nm of Ag is evaporated as a cathode through a shadow mask, so that the region of silver-ITO overlap defines the active area of the device (0.0121 cm^2). A diagram of the cross section of the device is shown in **Figure 4-1B**.

Devices are immediately placed in a liquid helium cryostat (Janis ST-100) with optical windows under vacuum (2×10^{-6} Torr) and cooled from 300 to 4.5 K in steps of 20 K, allowing sufficient time for equilibration at each temperature, typically 15 minutes. We measure the external quantum efficiency (QE) using a chopped monochromatic light source, calibrated photodetectors, and a lock-in amplifier, from 350 to 1300 nm. We measure current-voltage curves with a Keithley 2636A sourcemeter in the dark and under

NIR illumination from a 50 mW, 1053 nm laser, using 6 different neutral density filters to achieve an incident power range of 1.6 to 524 mW cm^{-2}.

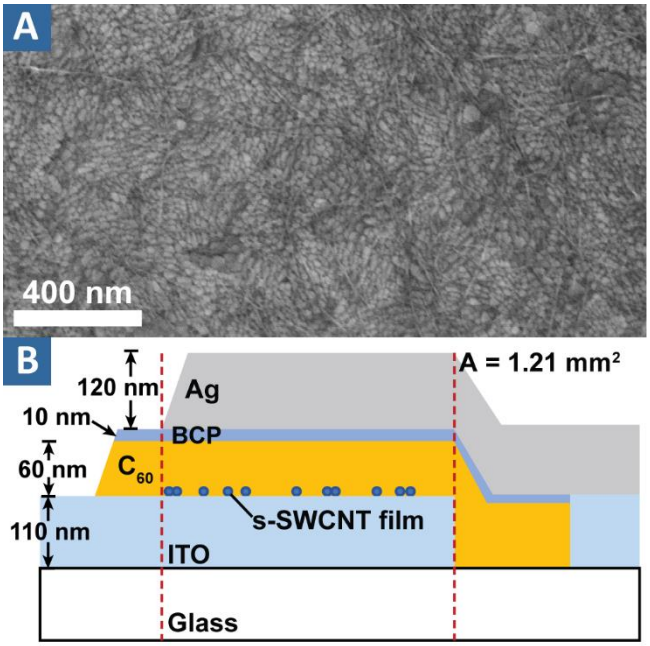

Figure 4-1. (A) (7,5) s-SWCNTs are deposited on ITO substrate via spin-coating. The s-SWCNTs are the filaments covering the ITO grains, which are visible between s-SWCNT fibers. **(B)** Cross section diagram of photovoltaic cells. The active area is defined by the overlapping silver and ITO regions and is 1.21 mm^2.

EXTERNAL QE AT LOW TEMPERATURE

Before examining charge recombination and energy offsets, we first study the external QE of the s-SWCNT/C_{60} photovoltaic cells as a function of temperature to gain insight into the energetics of exciton dissociation at the s-SWCNT/C_{60} interface. The external QE is shown in **Figure 4-2A** as a function of wavelength and temperature. The region of the spectrum corresponding to s-SWCNT excitation has several features: S_{11} transitions from (7,5) near 1050 nm and minority chirality s-SWCNTs (here, likely (6,5) at 1000 nm and (7,6) at 1150 nm), S_{22} transitions near 650 nm, and the S_{11}-phonon sideband near 900 nm. All of these transitions display only small changes with temperature over the entire temperature range of 300 to 4.5 K. The second region is dominated by absorption and exciton generation in C_{60} and extends from 700 nm to below 350 nm. We fit Gaussians to the S_{11} and S_{22} peaks. An exponential C_{60} absorption tail is subtracted from the S_{22} region (see **Figure 4-S1**) and a linear background is subtracted from the S_{11} region

prior to fitting. The fit parameters, peak height, centers, and full width at half maximum, (FWHM) are displayed in **Figure 4-2B-D** as a function of temperature. For both s-SWCNT transitions, the peak external QE at S_{11} and S_{22} only slightly decreases with temperature. The peak centers show a blue shift of 7 and 4 meV, and the FWHM decrease by 7 and 10 meV for the S_{11} and S_{22} transitions, respectively. The fits for S_{22} are somewhat complicated by the C_{60} background subtraction, and we believe that the apparent increase in the S_{22} FWHM near 200 K is likely an artifact of imperfect fitting of this background. The external QE of the device at 420 nm is dominated by exciton generation in bulk C_{60} and experiences a more significant drop below 200 K from nearly 13% at 200 K to a minimum of 5.2% at 4.5 K.

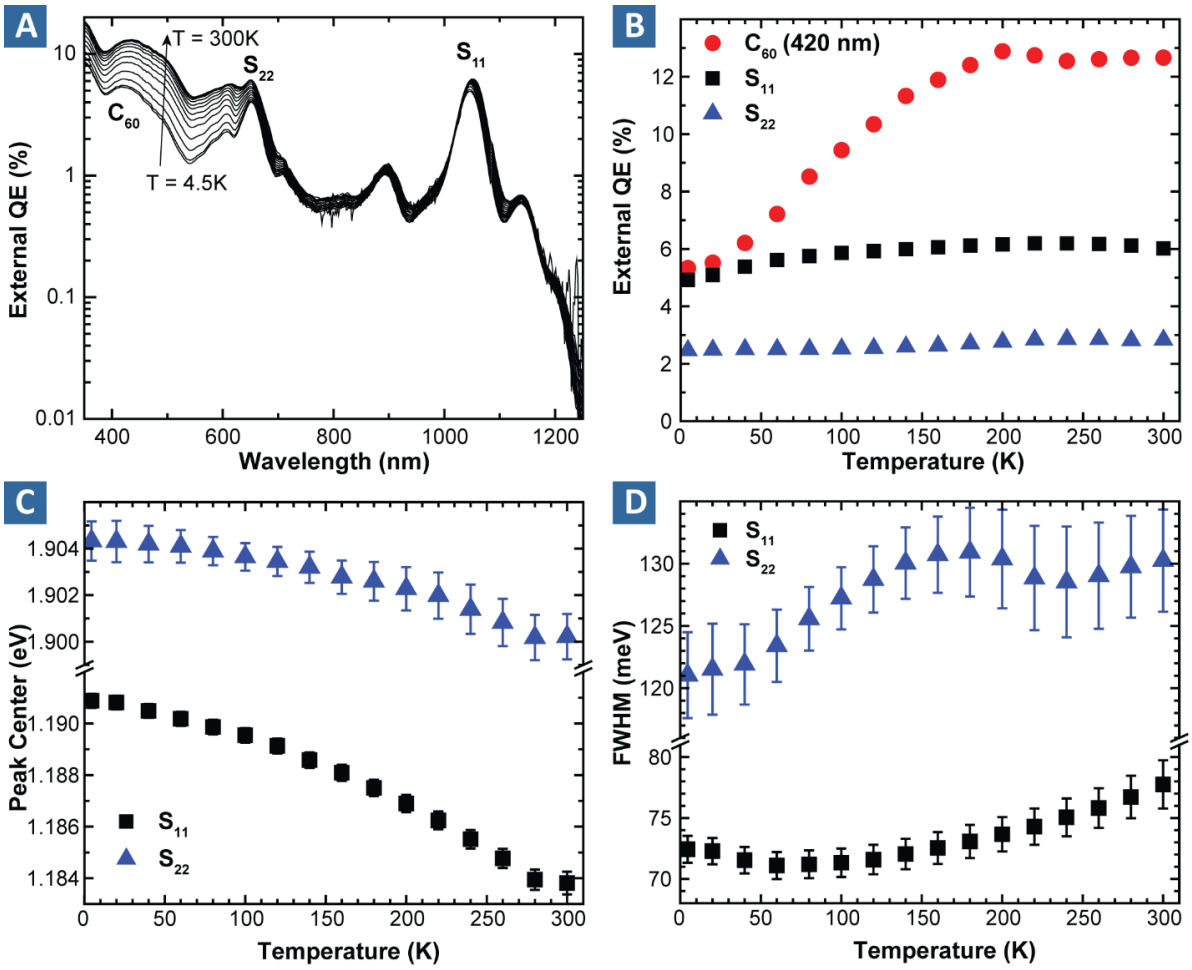

Figure 4-2. (A) The external quantum efficiency (EQE) is displayed as a function of wavelength for temperature from 300 to 4.5 K in 20 K increments. (B) Peak external QE at three selected wavelengths corresponding to C_{60} (red circles) at 420 nm, s-SWCNT S_{11} (black squares), and s-SWCNT S_{22} transitions (blue triangles). (C) Peak centers and (D) full widths at half maximum (FWHM) are displayed as a function of temperature.

We first discuss the near temperature-independence of the s-SWCNT transitions in the external QE spectrum. Previous studies have investigated the external QE of s-SWCNT solar cells as a function of polymer concentration[84] and s-SWCNT chirality,[80] providing insight into exciton diffusion and dissociation at s-SWCNT/C_{60} heterojunctions. Temperature-dependent measurements of external QE enhance understanding of the energetics of exciton dissociation at the heterojunction. The external QE is the product of four terms:

$$\text{External QE} = \eta_{Abs}\eta_{Diff}\eta_{Diss}\,\eta_{CC} \quad \textbf{[4-1]}$$

Here, η_{Abs} is the fraction of photons absorbed by the s-SWCNT film; η_{Diff} is the fraction of photogenerated excitons that reach the interface; η_{Diss} is the fraction of excitons reaching the interface that are dissociated into free carriers; and η_{CC} is the fraction of free carriers collected at the electrodes. The nearly temperature-independent external QE suggests that each of the four terms is also highly temperature independent. Of the four terms, η_{Diss} is the most interesting. Among the other 3 terms, we expect that both η_{Diff} and η_{CC} should be high because the s-SWCNTs films are so thin that exciton and charge transport are not expected to be limiting processes, and **Figure 4-S2** shows that the transmission spectrum of a s-SWCNT thin film, and thus η_{Abs}, only weakly changes with temperature.

The exciton dissociation efficiency η_{Diss} is proportional to $k_{Diss}/(k_{Diss} + k_{Loss})$ where k_{Diss} is the dissociation rate and k_{Loss} comprises other loss mechanisms, chiefly exciton quenching at defects,[20] exciton trapping on small-bandgap nanotubes,[17] and interfacial recombination. In accordance with Ihly et al., k_{Diss} may be described by Marcus theory,[92]

$$k_{Diss} = A\exp\left(-\frac{(\lambda + \Delta G)^2}{4\lambda k_B T}\right) \quad \textbf{[4-2]}$$

where A is a pre-exponential factor, λ is the reorganization energy, and ΔG is the change in Gibbs free energy associated with exciton dissociation. Notably, since we do not observe an exponential dependence of external QE, and therefore η_{diss}, on temperature, either the value of k_{Loss} decreases commensurately with k_{Diss}, which is unlikely, or k_{Diss} is only a weak function of temperature. A temperature-independent k_{Diss} is indicative of λ and ΔG being of similar magnitude and opposite sign. Indeed, Ihly et al. estimate λ

and ΔG for the (7,5)/C_{60} heterojunction to be 133±27 meV and -110 meV respectively, predicting a nearly temperature-independent k_{Diss} consistent with our measurements. In contrast to the s-SWCNT transitions, the C_{60} transition in the external QE spectra does substantially decrease with temperature. It is known that photocurrent in C_{60} thin films is mostly generated *via* bulk ionization, as opposed to exciton dissociation, in a process that is temperature-dependent,[93] explaining the significant decrease observed in the C_{60} region of the spectra below 200 K.

GENERATION, RECOMBINATION, AND CURRENT-VOLTAGE CURVES

We next examine the current-voltage characteristics of the s-SWCNT/C_{60} photovoltaic cells to gain understanding of the charge carrier recombination mechanisms present in these devices. Careful study of current-voltage curves yield estimates for the hole trap depth in s-SWCNT films and the offset energy ΔE_{HL}. We begin from a mathematical approach by deriving the diode equations from a treatment of charge carrier balances at the interface. In **Figure 4-3A** we present a diagram of the relevant energy levels within the device. We model recombination occurring at the s-SWCNT/C_{60} interface only. Initially we consider the case where recombination proceeds between free electrons in the C_{60} acceptor and free holes in the s-SWCNT. The free carrier balance is

$$\frac{J}{qd} - R + G_{th} + \frac{J_L}{qd} = 0 \qquad \textbf{[4-3]}$$

where J is the current density, q is the fundamental charge, d is the distance across the interface, R is the recombination rate at the interface, G_{th} is the equilibrium rate of free carrier generation in the dark devoid of applied voltage, and J_L is the current density arising from exciton dissociation at the interface. The recombination rate $R = k_{rf}np$ where k_{rf} is the free carrier recombination rate constant, and n and p are the free electron and hole densities at the interface, respectively. At thermal equilibrium, the generation rate is equal to the recombination rate, and $G_{th} = k_{rf}n_{eq}p_{eq}$ where the subscript eq refers to the value of the charge carrier density at thermal equilibrium. Rearranging and substituting into equation (3) gives

$$J = qdk_{rf}\left(np - n_{eq}p_{eq}\right) - J_L. \quad \textbf{[4-4]}$$

The free carrier concentration at the metal-semiconductor interfaces are described by

$$p_0 = N_V f_a(E,T)\exp\left(-\frac{\Phi_a}{k_B T}\right) \quad \textbf{[4-5a]}$$

$$n_0 = N_C f_c(E,T)\exp\left(-\frac{\Phi_c}{k_B T}\right) \quad \textbf{[4-5b]}$$

where N_V and N_C are the effective density of states at the valence band of the s-SWCNT and conduction band of the C_{60}, respectively. The functions $f_a(E,T)$ and $f_c(E,T)$ describe the effect of electric field E and temperature T on the anode and cathode injection current, respectively, and are usually assumed to remain near unity at low fields near room temperature.[94] We proceed under this assumption, though we will return to discuss its validity upon examination of the device operation at low temperature.

The population density of electrons and holes at the s-SWCNT/C_{60} interface is related to the built-in potential $V_{bi} = \Delta E_{HL} - \Phi_a - \Phi_c$ where ΔE_{HL} is the energy between the s-SWCNT donor highest occupied molecular orbital (HOMO) and C_{60} acceptor lowest unoccupied molecular orbital (LUMO),

$$p = p_0\exp\left(-\frac{q\delta_{CNT}(V_{bi}-V)}{k_B T}\right) \quad \textbf{[4-6a]}$$

$$n = n_0\exp\left(-\frac{q\delta_{C_{60}}(V_{bi}-V)}{k_B T}\right) \quad \textbf{[4-6b]}$$

where the fractions of the applied potential that drop across the s-SWCNT and C_{60} layers are δ_{CNT} and $\delta_{C_{60}}$, respectively. At equilibrium, there is no applied voltage, and

$$p_{eq} = p_0\exp\left(-\frac{q\delta_{CNT}V_{bi}}{k_B T}\right) \quad \textbf{[4-7a]}$$

$$n_{eq} = n_0\exp\left(-\frac{q\delta_{C_{60}}V_{bi}}{k_B T}\right) \quad \textbf{[4-7b]}$$

Substituting equations (5), (6), and (7) into equation (4) gives the following expression for the current density through the diode with free carrier recombination only and is equivalent to the Shockley diode equation. If the total applied voltage drops only across the semiconductor bulk (i.e. $\delta_{C_{60}} + \delta_{CNT} = 1$), then:

$$J = J_S\left(\exp\left(\frac{qV}{k_BT}\right) - 1\right) - J_L \quad \textbf{[4-8a]}$$

$$J_S = qdk_{rf}N_CN_V \exp\left(-\frac{\Delta E_{HL}}{k_BT}\right). \quad \textbf{[4-8b]}$$

Typically, the current-voltage characteristics of photovoltaic cells are fit with the modified Shockley diode equation to account for series and shunt resistances

$$J = J_S\left(\exp\left(-\frac{q(V - JR_S)}{nk_BT}\right) - 1\right) - \frac{V - JR_S}{R_P} - J_L(V). \quad \textbf{[4-9]}$$

Here, J is the current density, J_S is the reverse-bias saturation current density, which is temperature-dependent, q is the elementary charge, V is the applied voltage, R_S is the series resistance, n is the diode ideality factor, k_B is Boltzmann's constant, T is the temperature, R_P is the parallel, or shunt, resistance, and J_L is the generated photocurrent density.

Though it is widely used, the Shockley equation often poorly fits polymer and small molecule solar cells and is not able to accurately replicate the forward bias current-voltage curve, especially at low forward bias and low temperatures.[94-95] Indeed, we observe difficulty fitting s-SWCNT/C_{60} *J-V* characteristic curves to the generalized Shockley equation in forward bias (see **Figure 4-S3**). Particularly at low temperature, the ideality factor n becomes much larger than 2, which is unphysical for both Shottky-Read-Hall and direct band-to-band recombination. The failure in fitting to the generalized Shockley equation suggests that additional recombination mechanisms beyond free-carrier recombination must be relevant at the s-SWCNT/C_{60} interface.

It is common to attribute the current voltage behavior in the low bias region to shunt resistance.[95-97] However, Giebink et al. have examined the current-voltage characteristics of two model devices with fullerene-C_{60} as the electron acceptor and copper pthalocyanine or boron subphthalocyanine chloride as the donor[94] and shown that the current-voltage curves for these devices are best fit by a model that considers two different, parallel recombination mechanisms. The *J-V* behaviors predicted by this model are the same as those produced by a circuit with two diodes in parallel, each with a distinct ideality factor and saturation current density corresponding to a different recombination pathway. In Giebink's work, the two

recombination pathways are attributed to (i) the recombination of free electrons in the acceptor layer with trapped holes in the donor layer and (ii) the recombination of free holes in the donor layer with trapped electrons in the acceptor layer. As we will show, we are able to successfully fit the *J-V* curves in **Figure 4-3C** to this two diode model. We follow Giebink's derivation of recombination currents for trap-mediated processes in the discussion that follows.[94]

Including recombination at trap sites, the free carrier balance at the interface becomes

$$\frac{J}{qd} - R_{pt} - R_{nt} + G_{pt,th} + G_{nt,th} + \frac{J_L}{qd} = 0. \quad \textbf{[4-10]}$$

Here, the subscripts *pt* and *nt* refer to hole and electron trap-dominated processes, respectively. We develop the following expressions for the total current density:

$$J = J_{pt} + J_{nt} - J_L \quad \textbf{[4-11a]}$$

$$J_{pt} = qdk_{rpt}\left(np_t - n_{eq}p_{t,eq}\right) \quad \textbf{[4-11b]}$$

$$J_{nt} = qdk_{rnt}\left(n_t p - n_{t,eq}p_{eq}\right) \quad \textbf{[4-11c]}$$

Here, the subscript *t* indicates trapped carriers. At each temperature and applied voltage, one of the two recombination pathways will dominate. To determine which pathway dominates under particular conditions, we relate the trapped carrier concentration to the free carrier concentration assuming an exponential trap distribution.[98] The number of trapped carriers depends on the temperature and density of trap states and is described by

$$p_t = N_{Vt}\left(\frac{p}{N_V}\right)^{\frac{T}{T_{pt}}}. \quad \textbf{[4-12a]}$$

$$n_t = N_{Ct}\left(\frac{n}{N_C}\right)^{\frac{T}{T_{nt}}} \quad \textbf{[4-12b]}$$

where N_{Vt} and N_{Ct} are the density of trap states in the valence and conduction bands, and T_{pt} and T_{nt} are the trap temperatures for holes in s-SWCNT and C_{60} films, respectively. Substitution into equations (6) and (7) yields the following expressions for recombination current density, consistent with the derivation of Giebink et al.[94]

$$J_{pt} = J_{Spt}\left(\exp\left(\frac{qV}{n_{pt}k_BT}\right) - 1\right) \quad \textbf{[4-13a]}$$

$$J_{nt} = J_{Snt}\left(\exp\left(\frac{qV}{n_{nt}k_BT}\right) - 1\right) \quad \textbf{[4-13b]}$$

where

$$J_{Spt} = qdk_{rpt}N_CN_{Vt}\exp\left(-\frac{\alpha_{pt}}{k_BT}\right) \quad \textbf{[4-14a]}$$

$$J_{Snt} = qdk_{rnt}N_{Ct}N_V\exp\left(-\frac{\alpha_{nt}}{k_BT}\right). \quad \textbf{[4-14b]}$$

The terms α_{pt} and α_{nt} are energetic terms that closely follow ΔE_{HL}.

$$\alpha_{pt} = \frac{\Delta E_{HL}}{n_{pt}} + \frac{T_{pt} - T}{T_{pt}}\Delta\Phi \quad \textbf{[4-15a]}$$

$$\alpha_{nt} = \frac{\Delta E_{HL}}{n_{nt}} - \frac{T_{nt} - T}{T_{nt}}\Delta\Phi \quad \textbf{[4-15b]}$$

where

$$\Delta\Phi = \delta_{CNT}\Phi_c - \delta_{C_{60}}\Phi_a. \quad \textbf{[4-15c]}$$

In these equations, n_{pt} and n_{nt} represent two new ideality factors,

$$n_{pt} = \frac{T_{pt}}{\delta_{C_{60}}(T_{pt} - T) + T} \quad \textbf{[4-16a]}$$

$$n_{nt} = \frac{T_{nt}}{\delta_{CNT}(T_{nt} - T) + T} \quad \textbf{[4-16b]}$$

For clarity, we assign n_{pt} and n_{nt} to the low and high-forward bias ideality factors, respectively, though the choice of carrier is arbitrary at this point. Thus, we write a modified two-diode equation with these assignments in mind,

$$J = J_{Spt}\left(\exp\left(\frac{q(V - JR_S)}{n_{pt}k_BT}\right) - 1\right) + J_{Snt}\left(\exp\left(\frac{q(V - JR_S)}{n_{nt}k_BT}\right) - 1\right) + \frac{V - JR_S}{R_P} - J_L(V). \quad \textbf{[4-17]}$$

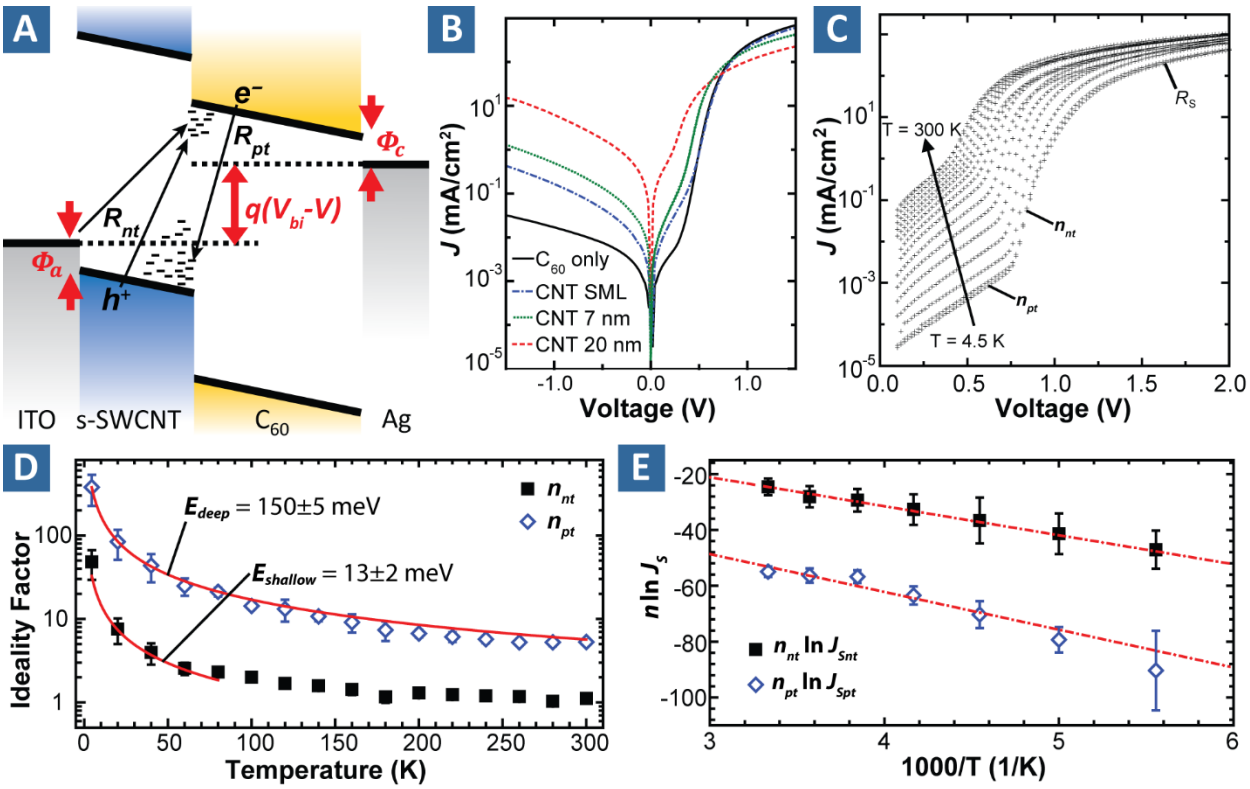

Figure 4-3. (A) Energy band diagram of the s-SWCNT/C_{60} photovoltaic cell under bias. The injection barriers at the anode and cathode are Φ_a and Φ_c, respectively. Interfacial trap states are represented by the short lines in the gap. Recombination proceeds via two pathways, associated with two trap depths, and possibly two carriers; for example, free electrons may recombine with trapped holes in the s-SWCNT film at rate R_{pt} and free holes recombine with trapped electrons in the C_{60} at rate R_{nt}. **(B)** The *J-V* characteristics of ITO/C_{60} Schottky junction diode, and s-SWCNT/C_{60} photovoltaic cells with varying thickness of s-SWCNT, from the sub-monolayer (SML) used in external QE measurements to 20 nm. In all devices two distinct slopes, each corresponding to a separate ideality factor, are observed, though the curves are offset with increasing thickness. **(C)** The forward bias *J-V* characteristics of the s-SWCNT/C_{60} devices in the dark over the temperature range from 300 to 4.5 K are plotted in 20 K intervals. **(D)** Ideality factors extracted from fits to the two diode model, with n_{pt} and n_{nt} fit (red) to equation (16). **(E)** Plot of $n\ln(J_S)$ versus $1000/T$ for both diodes. The red lines are linear fits, and applying equations (14) and (15), allow ΔE_{HL} to be estimated as 0.81±0.10 eV.

IDEALITY FACTOR AND TRAP-LIMITED RECOMBINATION

We next compare the predictions of the model to experimental current-voltage curves at room temperature (300 K). First, to understand the effects of s-SWCNTs on recombination pathways in the device, we fabricate equivalent devices lacking the s-SWCNT film. The current-voltage curve of an ITO/C_{60} device is shown in **Figure 4-3B**. We observe an exponential region, in which $d(\log J)/dV$ is linear, and a

region at higher bias where series resistance dominates. In the exponential region, the slope $d(\log J)/dV \approx 1$. We attribute this region to free carrier recombination of electrons in C_{60} with holes in the ITO. We next fabricate devices with increasing thickness of s-SWCNT film, from sub-monolayer films used in external QE measurements, to thick, ~20 nm films (see **Figure 4-S4** for SEM image and optical absorbance of thick films). Current-voltage curves for these devices are also shown in **Figure 4-3B**. We note several features of the current-voltage curves as the s-SWCNT thickness increases. First, $d(\log J)/dV$ in the region from 0.4 to 0.7 V remains near 1, implying the free carrier recombination mechanism is the same in all cases. However, the curve shifts to lower bias, consistent with a changing density of states $N_V N_C$ or recombination rate constant k_r. The series resistance also increases in thicker films. On the other hand, at low bias ($V <$ 0.4 V), the current density is significantly higher in devices containing s-SWCNTs, even for sub-monolayer films. Interestingly, $d(\log J)/dV$ is also linear in this region, although the slope is significantly lower, corresponding with an ideality factor ~5 at room temperature. Though we have here focused on sub-monolayer s-SWCNT films to avoid the potentially confounding effects of exciton diffusion in thick films, we have observed many of the same behaviors in thick films as well (see Supporting Information).

We next measure the *J-V* curves for the sub-monolayer devices over the temperature range of 4.5 to 300 K (**Figure 4-3C**). We fit the *J-V* curves to equation (17) to understand the recombination mechanisms responsible for each diode. The parameters n_{pt}, n_{nt}, J_{Spt}, J_{Snt}, and R_S are fit for each temperature. The ideality factors are presented in **Figure 4-3D** as a function of temperature. n_{pt} increases gradually from a value of ~5 at 300 K to nearly 400 at 4.5 K, while n_{nt} remains near unity until $T < 100K$ below which it too increases dramatically. The dependence of n_{pt} and n_{nt} on temperature is fit to equations (16a) and (16b) where $T_{t,CNT}$ and $T_{t,C_{60}}$ are the trap temperatures. We fit a trap depth of 150±5 meV (1700±50 K) for hole traps in the s-SWCNT film. This trap depth is consistent with the presence of minority s-SWCNT present in the film, predominantly (7,6) and (8,6), which have band gaps several hundred meV less than the (7,5) nanotube majority. The traps could arise from other factors as well including sidewall defects or impurities incorporated into the films. On the other hand, at extremely low temperatures, the ITO/C_{60} *J-V*

curves appear to contain two diodes as well, though at significantly lower current density (see Supporting Information). Since two diodes are expected to appear whenever two distinct and asymmetric recombination mechanisms exist, it is unclear whether this new ideality factor is due to recombination via deep traps in C_{60}, or some other mechanism, and should be the focus of future study.

The temperature dependence of n_{nt}, on the other hand, does not agree well with equation (16b), which predicts that n_{nt} remains near unity independent of temperature. A similar disagreement of model with measurement was observed by Giebink et al. at the low temperature limits of their measurements.[94] We implicitly made three assumptions in the derivation of equations (13-16) that may not be valid under all conditions. First, the parameters δ_{CNT} and $\delta_{C_{60}}$ are constrained by $\delta_{C_{60}} + \delta_{CNT} = 1$. If this constraint is relaxed, such that other sources of voltage drop exist within the device at low temperature, then equations (16a) and (16b) are decoupled and both ideality factors are allowed to increase. In the case that δ_{CNT} and $\delta_{C_{60}}$ are independent, we may estimate a much shallower trap depth of 13±2 meV (150±20 K). Second, we assumed that the factor $f(E,T)$ included in the description of carrier injection at the metal-semiconductor interface in equations (5a) and (5b) was near unity; under high fields and low temperature, injection is dominated by Schottky barrier lowering[99] and injection via tail states.[100] Finally, the number of free carriers at the interface were implicitly assumed to be roughly equal to the total number of carriers given by equations (6a) and (6b). This may not be the case at low temperature, where a significant portion of carriers are "frozen" into traps. In equations (11a) and (11b) the diode currents J_{pt} and J_{nt} depend on np_t and $n_t p$, respectively and are treated as independent. If the population of trapped holes far outnumbers that of free holes, then $n_t p$ is no longer independent of np_t, and the recombination rate of trapped electrons not only depends on the electron trap temperature, but the hole trap temperature as well.

ENERGY OFFEST AT THE S-SWCNT/C_{60} HETEROINTERFACE

Next, we estimate the interfacial energy offset by studying the temperature dependence of the saturation current density. The products $n_{pt} \ln J_{Spt}$ and $n_{nt} \ln J_{Snt}$ extracted from the fits of the *J-V* data

are plotted as a function of inverse temperature in **Figure 4-3E**. Lines are fit to the data in the high temperature limit, where the modeled and measured ideality factors are in agreement. Using the fit slopes of and equations (14) and (15), we solve for $\Delta E_{HL} = 0.81 \pm 0.10$ eV and $\Delta\Phi = 0.08 \pm 0.02$ eV. The large confidence interval is a result of the relatively large error bars on the fit values of J_{Spt} and J_{Spt} (typically >10%). Nevertheless, this method provides a measure of the energy offset that will be shown to be consistent with that inferred from examination of the open circuit voltage. The calculated value of $\Delta\Phi$ is consistent with our assumption that the contact barrier heights are relatively symmetric.

A second pathway to understanding the energy offset ΔE_{HL} is studying the open circuit voltage (V_{OC}) as a function of temperature. Since we are interested in exciton generation in the s-SWCNT film, we illuminate the devices with a 1053 nm laser, corresponding to the S_{11} transition of the (7,5) s-SWCNT, at incident power density ranging from 1.6 to 524 mW cm^{-2} and measure *J-V* curves. Since the excitation laser is beyond the range of C_{60} absorption, the only effect of the electron acceptor is the energy level of the LUMO; all photovoltage arises from excitons generated in the s-SWCNT layer. However, the V_{OC} of an equivalent ITO/C_{60} device may be measured using different excitation wavelength and is included in **Figure 4-S6** in the supporting information. The dependence of V_{OC} on temperature in s-SWCNT/C_{60} devices is displayed in **Figure 4-4A**. V_{OC} increases with increasing incident power and decreasing temperature. In addition, the incident power required to achieve a high V_{OC} decreases; at 4.5 K, the difference in V_{OC} between minimum and maximum illumination (almost three orders of magnitude) is only 75 mV, whereas at 300K, there is nearly 400 mV difference. For a single diode, it is known that the open-circuit voltage follows a logarithmic dependence on current density,

$$V_{OC} = \frac{nk_BT}{q} \ln \frac{J_{SC}}{J_S}. \qquad \textbf{[4-18]}$$

In the case of two diodes, the V_{OC} is limited by the dominant diode at $J = J_{SC}$. At low illumination, and therefore low J_{SC}, recombination at deep traps dominates, and the slope of V_{OC} versus $\ln J_{SC}$ is proportional to n_{pt}. At higher illumination and higher J_{SC}, recombination of free carriers at room temperature, or shallow traps at cryogenic temperature, dominates, and the slope of V_{OC} versus $\ln J_{SC}$ is proportional to n_{nt}. This

relationship is observed in **Figure 4-4B**. In addition to measuring V_{OC} versus $\ln J_{SC}$, we use equation (17) and the fit parameters from the dark *J-V* characteristics of **Figure 4-3C** to model the expected V_{OC} for each current density, and plot the results for T = 120, 200, and 300 K in comparison to the experimental results for those temperatures. Once again, there are two regions each with a different characteristic slope. At high J_{SC}, the slope corresponds to $n_{nt}k_BT/q$. At low J_{SC}, the slope is larger, and corresponds to $n_{pt}k_BT/q$. This two slope character is also present in the V_{OC}-$\ln J_{SC}$ plot for thick (~20 nm) s-SWCNT/C_{60} devices. (**Figure 4-S7**). The quality of agreement between the V_{OC} extracted from the dark characteristics and experimentally measured V_{OC} further supports the physics underlying the model we have presented.

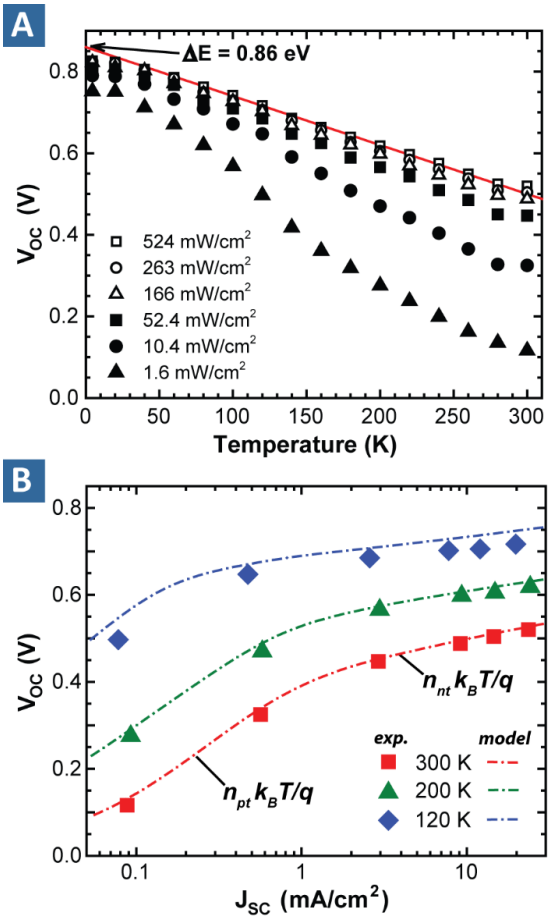

Figure 4-4. (A) The open circuit voltage (V_{OC}) is plotted as a function of temperature for all six incident power densities. V_{OC} increases with decreasing temperature to a maximum that is relatively power-independent at 0.82 V. **(B)** V_{OC} is plotted as a function of incident power. Two distinct slopes are evident. At high J_{SC}, the slope is proportional to n_{nt}, while at smaller incident power the slope is proportional to n_{pt}. The V_{OC} predicted from the dark current characteristics are plotted as dashed lines and display remarkable congruence with the experimental data measured under illumination.

The maximum open circuit voltage $V_{OC}^{\max}$ of a cell is a subject of great interest in the organic PV community. Understanding the origins of $V_{OC}^{\max}$ informs materials design to maximize efficiency and gives insight into the fundamental mechanisms of operation of organic photovoltaic devices. We note that J_L may be approximated by J_{SC} when series resistance is small, and $n_{nt}\alpha_{nt} \approx \Delta E_{HL}$ from equation (14). Then, when J_{SC} is large enough for the V_{OC} to be limited by n_{nt}, equation (18) may be written

$$qV_{OC} = \Delta E_{HL} - n_{nt}k_B T \ln\left(\frac{qdk_{rnt}N_{Ct}N_V}{J_{SC}}\right). \quad \textbf{[4-19]}$$

Equation (19) is equivalent to descriptions of the temperature dependence of V_{OC} elsewhere.[101-103] In general, $J_{SC} < qdk_{rnt}N_{Ct}N_V$, since the latter term represents the maximum recombination current possible given densities of states N_{Ct} and N_V. As J_{SC} increases, the slope of the V_{OC} versus T decreases, as observed in **Figure 4-4A**. Additionally, equation (19) predicts that the intercept of the fit to the linear region of the V_{OC} versus T plot is independent of incident power, and is equivalent to ΔE_{HL}. We fit a line to the data and extract $\Delta E_{HL} = 0.86 \pm 0.02$ eV, which compares favorably to the estimate of 0.81±0.10 eV from the analysis of the dark *J-V* curves.

In conclusion, we characterize the behavior of carbon nanotube / fullerene-C_{60} heterojunction photovoltaic cells as a function of temperature. We show that the external QE arising from s-SWCNT films is relatively robust with decreasing temperature, in contrast to the external QE from C_{60}, which decreases significantly below 200 K. The temperature independence of the external QE points to nearly identical values of the reorganization energy λ and free energy gain ΔG for excitons dissociating at the s-SWCNT/C_{60} heterojunction. We probe the current-voltage characteristics of the devices in the dark and fit to a two diode model, in which two different recombination pathways lead to two distinct ideality factors. We calculate two distinct trap depths of 13±2 and 150±5 meV. By fitting the temperature dependence of the saturation current density we estimate an interfacial energy gap of 0.81±0.10 eV. We also study the temperature and incident power dependence of the open circuit voltage of the devices under NIR illumination. The V_{OC} saturates at 0.82 V at 4.5 K, and linear extrapolation to the V_{OC} at 0 K allows the estimation of the interfacial

energy gap to be 0.86 eV, in agreement with that calculated from the temperature dependence of the saturation current density.

Finally, we briefly discuss the implications of these results on the behavior of s-SWCNT/C_{60} photovoltaic cells under solar illumination (100 mW cm^{-2}) in the context of these conclusions. The high-slope region of the V_{OC} vs J_{SC} curve, corresponding to recombination mediated by deep trap states at the s-SWCNT/C_{60} interface, is prominent only for incident power that is < 20 mW cm^{-2} at 300 K. Thus, these trap states in s-SWCNT photovoltaic cells are not expected to limit V_{OC} at room temperature. However, this high-slope region shifts to lower incident power at lower temperature; and, we can infer that it shifts to higher power at higher temperature. As a result, these trap states may play a role in limiting the V_{OC} and the power conversion efficiency of s-SWCNT/C_{60} heterojunction devices at the elevated operating temperature expected in the field. Therefore, in future work, it will be important to identify the origin of these trap states and to research materials processing approaches to eliminate them.

SUPPORTING INFORMATION

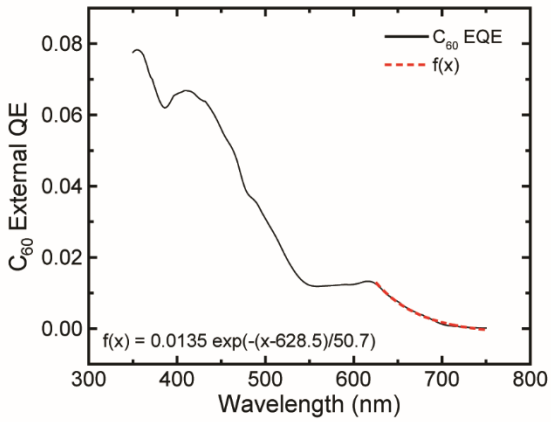

Figure 4-S1. External QE of ITO/C_{60} Schottky barrier photovoltaic cell at zero bias. The absorption tail between 630 and 750 is fit to the exponential function shown. This function is scaled to the height of the C_{60} peak in the s-SWCNT/C_{60} external QE spectrum and subtracted from the S_{22} region before fitting.

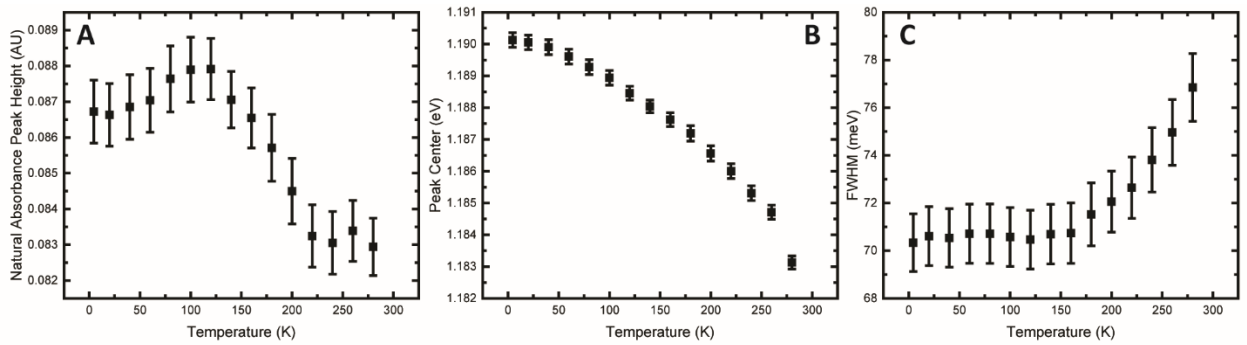

Figure 4-S2. Analysis of natural absorbance at S_{11} transition of ITO/s-SWCNT/C_{60} as a function of temperature. The S_{22} transition is obscured by C_{60} absorption. **(A)** Peak height, **(B)** Peak Center, and **(C)** Full width at half maximum (FWHM). Peak Center and FWHM are consistent with external QE (**Figure 4-2**). The absorption peak increases as temperature decreases, in contrast to external QE, which decreases with temperature. Error bars are associated with Gaussian fits.

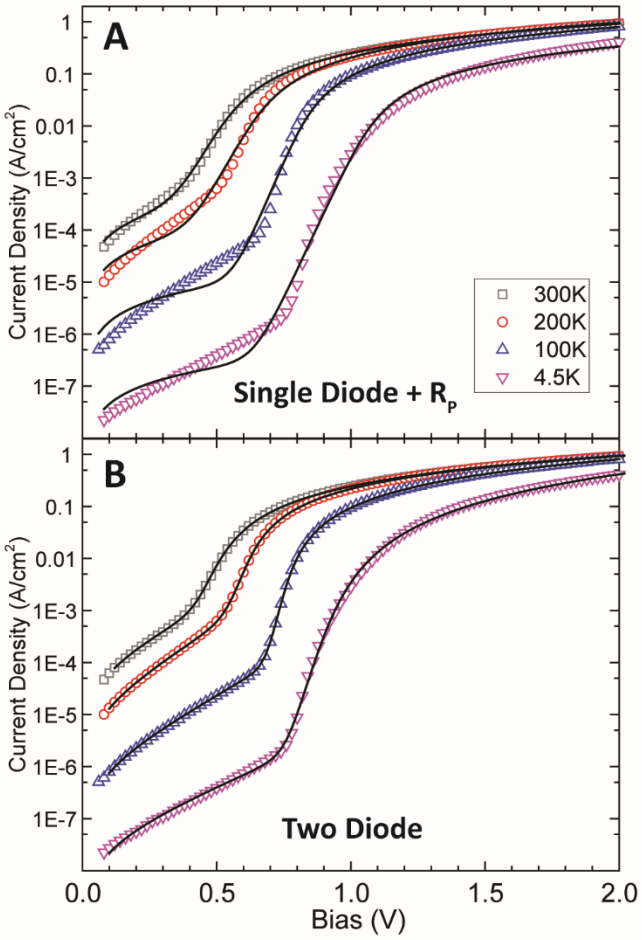

Figure 4-S3. Comparison of fits obtained from (A) a single diode Shockley equation and (B) the two diode model described in the main text.

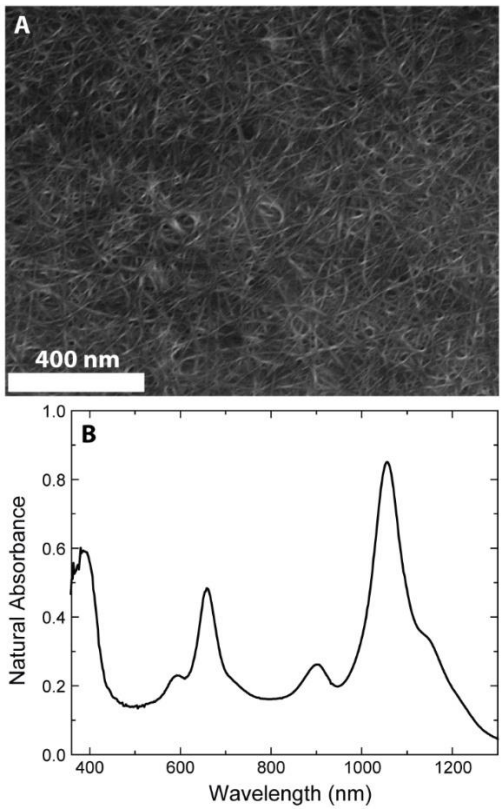

Figure 4-S4. (A) Scanning electron micrograph of a thick (~20 nm) film, in which grains of ITO are not visible, in contrast to **Figure 4-1A** in the main text. **(B)** Optical absorption spectrum of the thick film on ITO.

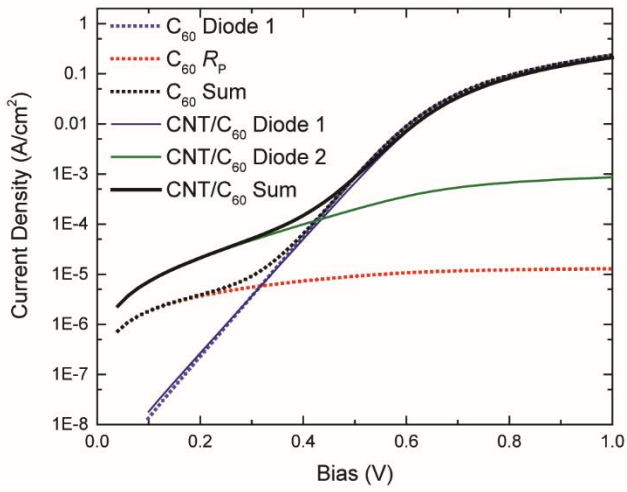

Figure 4-S5. Modeled J-V curves for the parallel components of C_{60} Schottky device, modeled by a single diode with shunt resistor and s-SWCNT/C_{60} device, modeled by two diodes in parallel. The shunt resistance R_P is sufficiently high to be a negligible contribution to the two-diode model. Therefore, we model equation (3) in the text without parallel resistance.

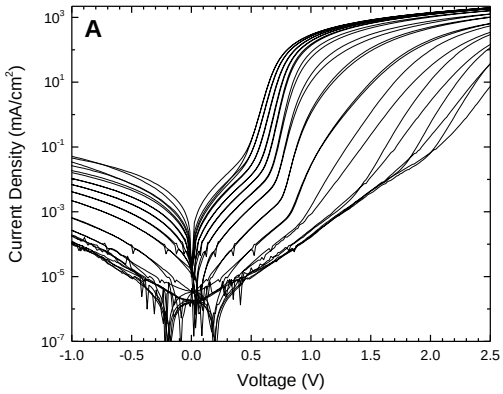

Figure 4-S6. JV curves of ITO/C_{60} devices in the dark.

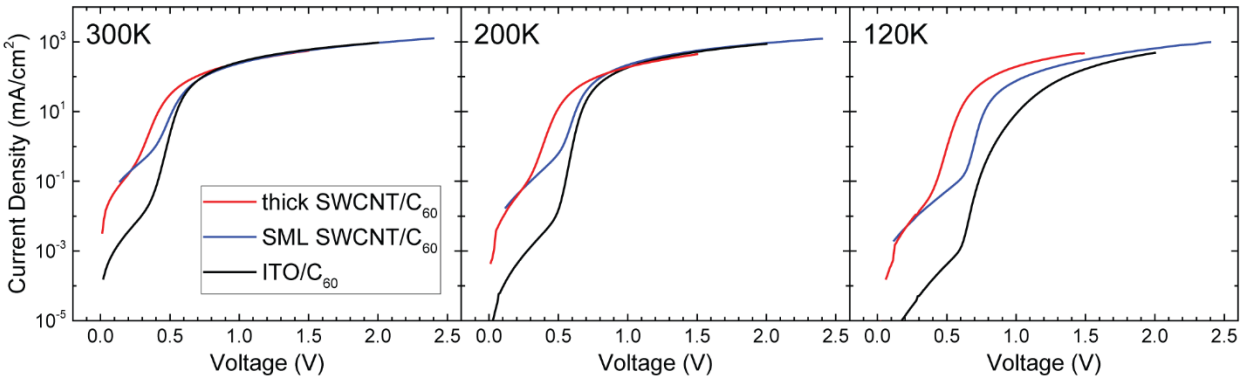

Figure 4-S7. Comparison of JV curves at select temperatures. At sufficiently low temperatures, the ITO/C_{60} appears to exhibit two diode behavior. This may be due to a second, deeper electron trapping level that is hidden by shunt resistance at room temperature. The thick films show a shifted diode, as at room temperature in **Figure 4-3B**.

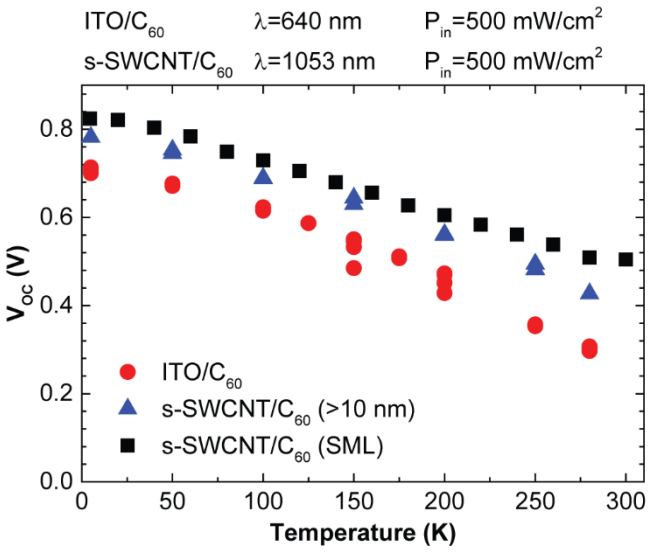

Figure 4-S8. Open circuit voltage (V_{OC}) of devices under 524 mW/cm^2 illumination (black, squares) from **Figure 4-4A** in the main text, compared with thick s-SWCNT/C_{60} devices (blue, triangle) at ~500 mW/cm^2. Both nanotube devices are illuminated with a 1053 nm laser. ITO/C_{60} devices illuminated with a 640 nm laser show a V_{OC} somewhat lower than the nanotube devices. According to our model, we expect this corresponds to the difference between the C_{60} LUMO and ITO work function.

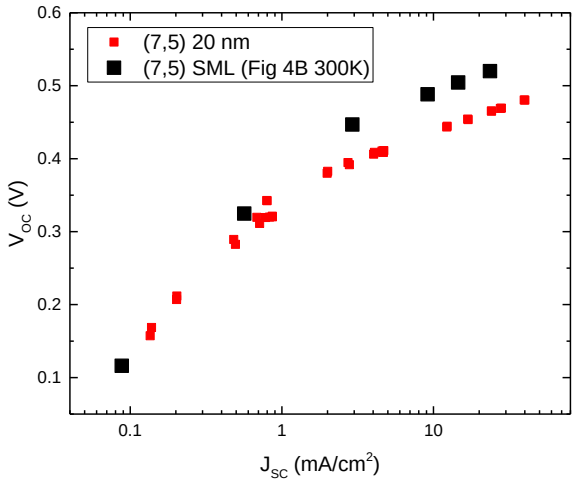

Figure 4-S9. Open-circuit voltage (V_{OC}) versus short circuit current density (J_{SC}) on a semi-log scale. Thick s-SWCNT films (~20 nm) were used to fabricate devices in the manner of the main text. The V_{OC} – log J_{SC} plot displays the same two-slope character described in the main text, consistent with two recombination mechanisms. The slightly lower V_{OC} for a given J_{SC} in the thicker devices is attributed to the increased series resistance and decreased shunt resistance in these devices.

CHAPTER 5: THE ROLE OF DEFECTS AS EXCITON QUENCHING SITES IN CARBON NANOTUBE PHOTOVOLTAICS

Adapted from:

Wang, J. L.; Shea, M. J.; Flach, J. T.; McDonough, T. J.; Way, A. J.; Zanni, M. T.; Arnold, M. S., Role of Defects as Exciton Quenching Sites in Carbon Nanotube Photovoltaics. Journal of Physical Chemistry C 2017, 121, 8310-8318.

The author developed and executed the Optical interference and Monte Carlo simulations, and assisted Jialiang Wang in the characterization and data analysis of experimental results. Jialiang Wang conducted all reactions, fabricated, and characterized devices. The author acknowledges Austin Way for X-ray photoelectron spectroscopy measurements and Jessi Flach, Dr. Thomas McDonough, and Dr. Martin Zanni for their transient absorbance data used in this work.

EXCITON DIFFUSION AND THE LIMITS OF QUANTUM EFFICIENCY

The performance of s-SWCNT-based devices has been limited to date, with a solar power conversion efficiency of less than a few percent[104] and a peak external quantum efficiency (QE) of less than 50%.[14] Several studies have sought to understand the fundamental behaviors of excitons and charges in these heterostructures,[105-107] but the dominant factors that limit external QE are still poorly understood. It is well known that photogenerated carriers in s-SWCNT layers are strongly bound as excitons with binding energies of 0.2-0.3 eV.[108-109] Bindl et al. have shown that this binding energy can be overcome in bilayer s-SWCNT/C_{60} donor/acceptor heterostructures with very thin (< 5 nm) s-SWCNT layers, in which an offset in the lowest unoccupied molecular orbital (LUMO) energy between the two materials drives exciton dissociation and electron transfer from the s-SWCNT to C_{60} at the heterointerface with an internal QE of >85%.[110] Ihly et al. have recently confirmed this electron transfer QE and shown that it can be described using Marcus theory.[111]

While an internal QE of >85% is excellent, high external QE devices will need to capture more light, and thus drive excitons through thicker s-SWCNT layers to the heterointerface. Experiments show that internal QE decreases with increasing s-SWCNT layer thickness because of the poor diffusion of excitons to the heterointerface.[110] Although excitons have long diffusion lengths along the long-axis of s-SWCNTs (typically > 100 nm),[112-114] most s-SWCNTs are oriented in the plane of the substrate in thin film

devices, necessitating inter-SWCNT exciton transport for which the diffusion length is much shorter, typically ≤ 5 nm.[84, 106, 110] Models have identified that metallic SWCNTs and spurious small bandgap s-SWCNTs might be factors that prevent long-range inter-SWCNT exciton transport.[115] However, experiments have demonstrated that the inter-SWCNT exciton diffusion length is short even when using s-SWCNTs that are > 99.9% semiconducting;[110] and, transient photobleaching and two-dimensional white light spectroscopy data show that most excitons in s-SWCNT films are lost to recombination even before they can become trapped on spurious small bandgap SWCNTs, suggesting that neither metallic nor small bandgap SWCNTs are primarily responsible for poor exciton diffusion to the heterointerface.[116-118]

The role of defects on exciton transport in s-SWCNT/acceptor heterojunction devices has yet to be studied in detail. There are good reasons to expect that both sidewall- and end- defects on SWCNTs play a large role in limiting exciton harvesting efficiency. For example, it is known from photoluminescence studies of isolated, individual s-SWCNTs that defects covalently bonded to the sidewalls of s-SWCNTs can trap and quench excitons.[119-121] Likewise, studies have shown that the photoluminescence decay dynamics of ensembles of s-SWCNTs isolated in solution can be described by a stretched exponential diffusion-limited contact-quenching model, in which the lifetime and population of excitons are dictated by the diffusion of excitons to defects where they are quenched. The ensemble data indicate that solution-processed SWCNTs (much like the SWCNTs used in photovoltaic devices) may be riddled with exciton quenching defects at a linear density as high as 8.3 μm^{-1}, limiting the exciton lifetime to several picoseconds.[21, 113]

In this work, we systematically study the influence of defects on the performance of bilayer s-SWCNTs/C_{60} heterojunction photovoltaic devices via both experiments and modeling. First, we intentionally add sp^3 sidewall defects to s-SWCNTs at varying concentrations via covalent diazonium chemistry. The density of defects is estimated using Raman and transient absorption spectroscopy. Next, s-SWCNT/C_{60} heterojunction photovoltaic cells are fabricated and characterized. Second, a diffusion limited contact-quenching Monte Carlo model is developed to assess the contributions of exciton quenching defects

on exciton migration in bilayer s-SWCNT/C_{60} heterojunction devices under a wide range of scenarios that cannot yet be experimentally accessed.

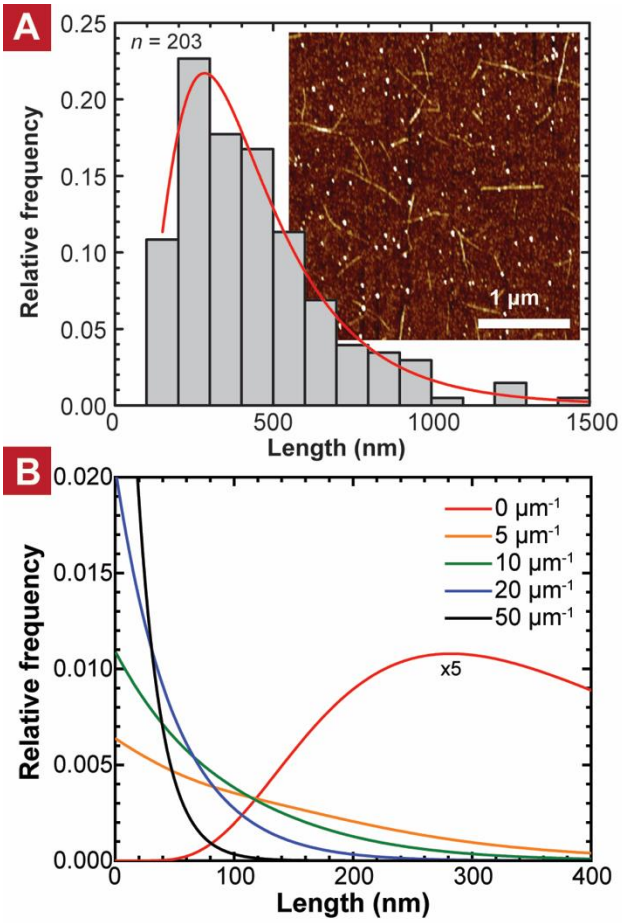

Figure 5-1. (A) Relative length frequency distribution of SWCNT 1. *Inset*: Representative atomic force micrograph of SWCNT 1 prior to functionalization. **(B)** Simulated probability distribution of segment length for various defect densities, n_d, if defects are added randomly to the measured distribution.

LINKING DEFECT DENSITY AND DEVICE PERFORMANCE

Estimating the defect density, n_d.

To experimentally study the influence of defects on bilayer s-SWCNT/C_{60} planar heterojunction photovoltaic devices, diazonium chemistry is used to introduce aryl sp^3 sidewall defects to s-SWCNTs at five different densities by varying the concentration of the diazonium reactant during the solution-phase functionalization described in the Experimental Methods section. s-SWCNT samples that have not been

treated via diazonium chemistry are referred to as sample **1** in the discussion and figures, below, whereas the five treated s-SWCNT samples are referenced as samples **2-6,** in which sample **6** is the most defective. Defects grafted via diazonium chemistry cluster on s-SWCNT sidewalls because the presence of one defect lowers the local energetic barrier for the nearby grafting of additional defects during the functionalization process. Of interest for understanding exciton migration in s-SWCNT photovoltaics are the density of these defect clusters (n_d) and the average length of the unfunctionalized segments of s-SWCNT in between the defect clusters ($\langle L_s \rangle = n_d^{-1}$). It is important to note that although not aryl-functionalized, sidewall defects are still likely present on **s-SWCNT 1** as byproducts of synthesis and processing. The ends of s-SWCNTs also quench excitons[21, 122-123] and thus the length distribution of the s-SWCNTs must be considered. The length distribution of **s-SWCNT 1** is measured by AFM (**Figure 5-1A**) to have a log-normal length distribution with a mean and standard deviation of 451 nm and 0.56, respectively. The random addition of defect clusters effectively sub-divides s-SWCNTs into shorter segments, shifting the weight of $g(L_s)$ towards smaller L_s with increasing n_d. The probability distribution functions, $g(L_s)$, associated with these length distributions are plotted in **Figure 5-1B**.

Raman spectroscopy and transient absorption spectroscopy may be used to provide measures of n_d and $g(L_s)$. **Figure 5-2A** shows the Raman spectra for **s-SWCNTs 1-6**. The Raman defect ratio I_D/I_G increases with increasing reactant concentration. Previous studies of Raman scattering in graphene and nanotubes have determined that n_d can be estimated from I_D/I_G according to the relationship,[124-125]

$$n_d = 1.5925 \times 10^{10}\ nm^3\ \frac{I_D}{I_G}\ \lambda(nm)^{-4} \qquad \textbf{[5-1]}$$

where λ is the wavelength of the Raman laser. Equation (5-1) plotted in **Figure 5-2B** (red) along with the experimentally measured values of I_D/I_G (circles), which gives n_d of 7.4, 9.3, 10, 19, 34, and 42 μm^{-1} for **s-SWCNTs 1-6**, respectively. (**Figure 5-2B**)

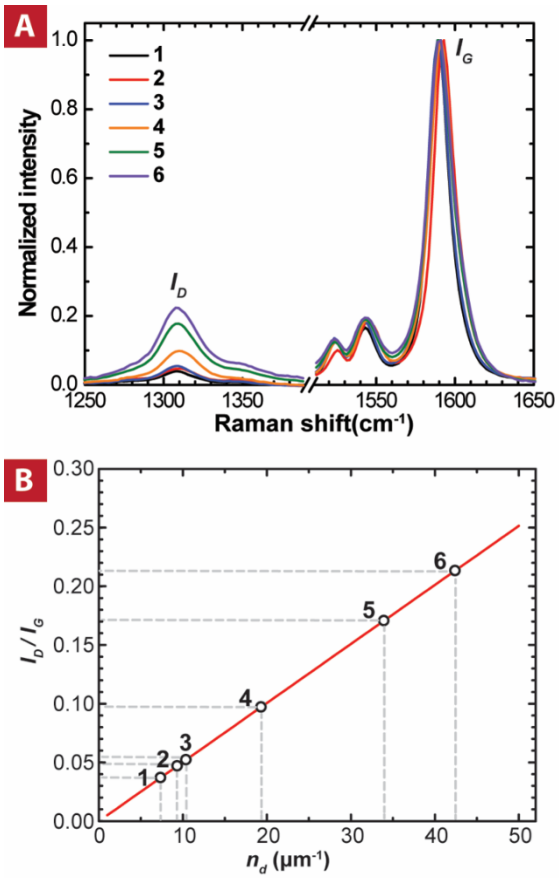

Figure 5-2. (A) Experimental Raman spectra of s-SWCNT samples with various defect densities. The "D" peak at 1310 cm^{-1} increases with increasing diazonium reactant concentration. **(B)** Expected relationship between I_D/I_G and defect density, n_d (see **Eqn. 5-1**).

Transient absorption spectroscopy is used to provide a separate measure of n_d and $g(L_s)$ through ensemble measurements of exciton decay dynamics in solution. **Figure 5-3A** shows the measured change in optical density (ΔOD) of **s-SWCNT 1-6** following a pump pulse, which tracks the exciton dynamics. The dynamics follow the form of a stretched exponential, in which

$$\Delta OD(t) = OD_o \exp\left(-\left(\frac{t}{\tau_0}\right)^{\frac{1}{2}}\right). \qquad \textbf{[5-2]}$$

The fit characteristic time-constant, τ_o, is 3.23, 2.87, 2.71, 1.59, 1.36, and 1.30 ps for **s-SWCNT 1-6**, respectively. This stretched exponential dependence is consistent with diffusion-limited defect-quenching kinetics.[21, 113] To relate τ_o to n_d, we first consider the diffusion-limited decay dynamics expected in a single segment of s-SWCNT and then calculate the dynamics expected for an ensemble of segments. Following a

short pump pulse, the population, φ, of excitons in a single segment of s-SWCNT of length, L_s, is expected to decay, to first order approximation, as

$$\varphi(t, L_s) = \varphi_o e^{\frac{-\pi^2 Dt}{L_s^2}}. \quad \textbf{[5-3]}$$

In this case, the population of excitons in an *ensemble* of length distribution $g(L_s)$ will decay as

$$\Delta OD(t) = OD_o \int_0^\infty g(L_s) e^{\frac{-\pi^2 Dt}{L_s^2}} dL_s. \quad \textbf{[5-4]}$$

Using $g(L_s)$ generated at various n_d (see **Figure 5-1**) and an intra-SWCNT diffusion coefficient, D, of 8 cm^2 s^{-1} (which falls in the middle of the range of 6.0 to 20 cm^2 s^{-1} reported in literature[113, 122]), we have used Eq. 4 to calculate the expected relationship between τ_o and n_d, which is plotted in red in **Figure 5-3B**. The experimentally measured values of τ_o are also plotted in **Figure 5-3B** (circles), giving n_d of 6.9, 7.6, 8.0, 12, 13, and 14 μm^{-1} for **s-SWCNTs 1-6**, respectively.

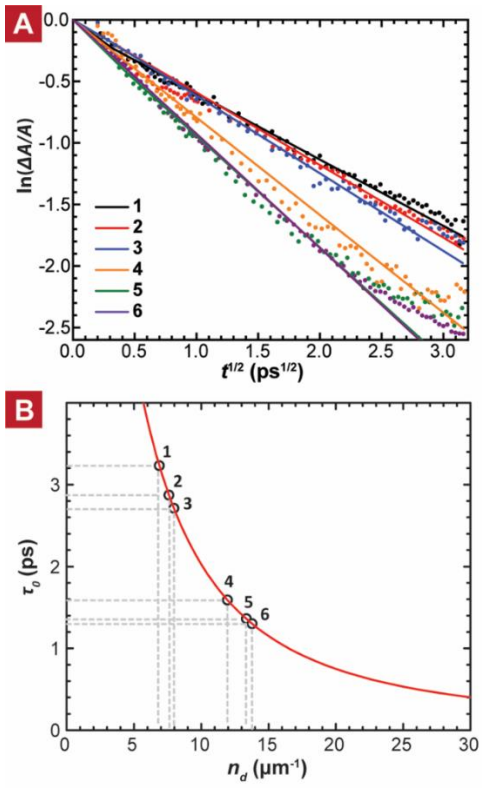

Figure 5-3. (A) Experimentally measured differential absorbance of s-SWCNT solutions with various defect densities, n_d. The time constant $\boldsymbol{\tau_0}$ is extracted from the slope of the best fit lines, in accordance with equation 2. **(B)** Simulated effect of random defect addition at density n_d (see **Figure 5-1B**) on $\boldsymbol{\tau_0}$.

Both the Raman and transient absorption data indicate an n_d of approximately 7 μm^{-1} in the untreated **s-SWCNT 1** sample. Both the Raman and transient absorption data also indicate that n_d increases with increasing aryl-functionalization, although the two methods disagree regarding the magnitude of the increase. For example, the Raman data estimate that n_d increases to 40 μm^{-1} in the most defective **s-SWCNT 6** sample whereas the transient absorption data estimate an increase to only 14 μm^{-1}. The actual n_d likely falls somewhere in between these two estimates because D-band Raman scattering from within the defect clusters themselves likely artificially inflates measures of I_D/I_G and n_d whereas the segment length may not be truly random, skewing the relationship between τ_o and n_d in the transient absorption calculation. Regardless, both datasets show a monotonic increase in n_d with diazonium reactant concentration, enabling an opportunity to experimentally study the impact of defects on device external QE.

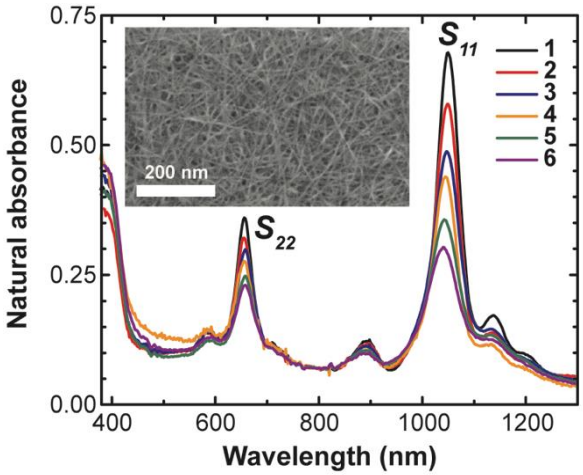

Figure 5-4. Natural absorbance as a function of wavelength for each defect density studied. Notably the S_{11} peak at 1050 nm decreases with increasing defect concentration. *Inset*: Scanning electron micrograph of a representative film of s-SWCNTs.

Device characterization.

The absorption spectra of s-SWCNT thin films prepared from **s-SWCNT 1-6** are compared in **Figure 5-4**. The distinctive absorption peak at 1055 nm corresponds to the first excitonic bandgap transition (S_{11}) of the (7,5) s-SWCNT. Features at 1000, 1150, and 1200 nm arise from the (6,5), (7,6), and (8,6) species, respectively. The second-order (S_{22}) transitions of the s-SWCNT species are visible near 650 nm.

The rise in absorption at 390 nm is attributed to the PFO wrapping, which makes up 50% of the film by weight.[84] The absence of metallic SWCNT absorption features[126] near 500 nm confirms the high semiconducting purity of the SWCNT films. Each film is the same thickness (~ 11 nm). However, we see that the absorptivity at the S_{ii} transitions decreases with increasing aryl-functionalization, indicating that optical cross-section decreases with increasing functionalization. We quantify the integrated S_{11} optical cross-section for the aryl-functionalized s-SWCNTs, σ_i, by using the following relationship

$$\int \sigma_{11,i}\, dE = \frac{\int A_{11,i} dE}{\int A_{11} dE} \int \sigma_{11} dE. \qquad \textbf{[5-5]}$$

Where the subscript i denotes the functionalization reaction condition, $\int A_{11,i}\, dE$ is the measured integrated absorption at the S_{11} transition of the functionalized **s-SWCNTs 2-6**, $\int A_{11}\, dE$ is the measured integrated absorption at the S_{11} transition of the unfunctionalized **s-SWCNTs 1**, and $\int \sigma_{11}\, dE$ is the known integrated S_{11} cross-section for unfunctionalized s-SWCNTs from Streit et al. The $\int \sigma_{11,i}\, dE$ at the various reaction conditions are compared in **Table 5-I**. The magnitude of the decrease in $\int \sigma_{11,i}\, dE$ with increasing functionalization density is important for understanding the measured external QE and determining the s-SWCNT film thicknesses in the device studies, to follow.

Bilayer s-SWCNT/C_{60} heterostructure devices are fabricated from **s-SWCNT 1-6**. A C_{60} layer thickness of 85 nm is chosen to maximize constructive interference[14, 86] at the (7,5) S_{11} while the thickness of the s-SWCNT layer is varied from 0 – 25 nm. External QE spectra of devices with a s-SWCNT thickness of approximately 5 nm are compared in **Figure 5-5A**. The external QE significantly decreases with increasing aryl-sidewall functionalization, decreasing from 40% at the (7,5) S_{11} using **s-SWCNT 1** to less than 8% using **s-SWCNT 6**. The external QE at the (7,5) S_{11} is plotted as a function of s-SWCNT layer thickness in **Figure 5-5B**. The external QE generally increases with increasing s-SWCNT layer thickness up to about 5 nm, regardless of the degree of sp^3-functionalization, but then decreases with further increase in s-SWCNT layer thickness. The initial rise can be attributed to the increased capture of photons that is achieved as the thickness of the s-SWCNT layer is increased, whereas the fall-off has been attributed to the

absorption losses that are incurred from s-SWCNTs deeply embedded in thicker layers beyond the inter-SWCNT exciton diffusion length.

Only part of the decline of external QE with increasing functionalization density can be attributed to the decreased optical cross-section previously noted in **Figure 5-4**. **Figure 5-5C** characterizes the peak external QE at 1050 nm, normalized by the peak optical cross-section at 1050 nm, as a function of the n_d estimated by Raman spectroscopy. The external QE normalized by cross-section decreases by a factor of 2.5 when comparing **s-SWCNT 1** with n_d = 7 μm^{-1} and **s-SWCNT 6** with n_d = 40 μm^{-1}. The external QE normalized by cross-section significantly declines even for small changes in n_d, for example decreasing by a factor of 1.3 when increasing n_d from 7 to only 9 μm^{-1} when comparing **s-SWCNT 1** and **2**. This strong dependence of external QE on n_d indicates that defect-induced quenching of excitons is a significant limitation even in photovoltaic devices fabricated from s-SWCNTs that have not been intentionally aryl-functionalized, presumably because of defects introduced to the s-SWCNTs via synthesis or during their processing.

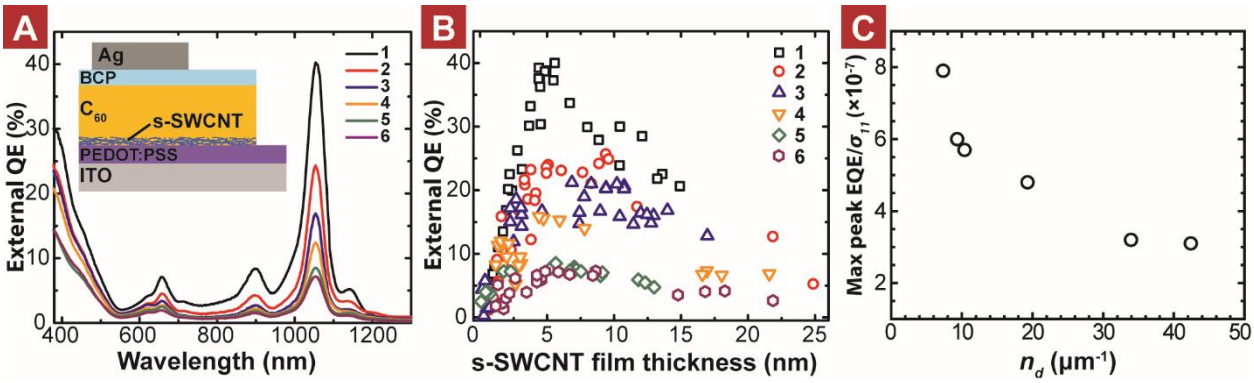

Figure 5-5. **(A)** External QE as a function of wavelength for each defect concentration. *Inset*: Bilayer s-SWCNT/C_{60} device architecture. **(B)** Peak external QE at S_{11} as a function of film thickness. **(C)** The peak external QE for each dataset is plotted versus the defect density, n_d, calculated from Raman spectroscopy in **Figure 5-2B**.

Table 5-I. Summary of s-SWCNT parameters under different reaction conditions.

Sample	$[R]:[C]^a$	I_D/I_G	Raman $n_d{}^b$ (μm^{-1})	τ_0 (ps)	TA $n_d{}^c$ (μm^{-1})	$\int \sigma_{11} dE^d$ ($10^4\ cm^2 eV\ g^{-1}$)	EQE^e (%)	$\sigma_{11}{}^f$ ($10^5\ cm^2$)	EQE/σ_{11} ($10^{-7}\ cm^{-2} g$)
1	0:1	0.037	7.4	3.2	6.9	3.88	40	5.05	7.9
2	0.1:1	0.047	9.3	2.9	7.6	3.17	26	4.37	6.0
3	1:1	0.052	10	2.7	8.0	3.03	21	3.69	5.7
4	22:1	0.097	19	1.6	12	2.52	16	3.32	4.8
5	1000:1	0.17	34	1.4	13	2.35	8.6	2.71	3.2
6	1784:1	0.21	42	1.3	14	2.06	7.1	2.26	3.1

[a] Molar ratio between reactant and s-SWCNT carbon atoms during solution-phase grafting. [b] Defect density calculated from Raman result. [c] Defect density calculated from transient absorption. [d] Composition-weighted average integrated optical cross-section, including (6,5), (7,5), (7,6) and (8,6) species. [e] Maximum EQE at (7,5) S_{11}. [f] Peak optical cross-section at (7,5) S_{11}.

DIFFUSION LIMITED CONTACT QUENCHING MONTE CARLO MODEL.

Next, we implement a Monte Carlo model of exciton diffusion in s-SWCNT layers to independently affirm that defect-inducted quenching of excitons is a significant limitation to s-SWCNT based photovoltaic devices. We also use this model to assess the possible performance gains that might be obtained if longer and/or more pristine s-SWCNTs were to be experimentally realized and used in devices. To show that our models closely mimic the behaviors of real devices, we first simulate the thickness-dependent external QE as a function of n_d. For these simulations, the exciton generation profile must be modeled, and for this, we use the optical transfer matrix method of Peumanns et al.[86] The real part of the complex index of refraction is taken from Blackburn et al.[127] and the imaginary part is determined from the optical cross-section measured in **Figure 5-4**. A SWCNT film of thickness t is modeled as a series of layers of thickness 2 nm. The exciton generation rate in each layer is proportional to the optical field intensity at S_{11} in each layer. Excitons are generated on a SWCNT segment of length L_s, where L_s is consistent with the SWCNT segment length distribution after the introduction of defects at a density n_d (see **Figure 5-1B**). The introduction of defect clusters is assumed to be a random process. **Figure 5-6A** displays a schematic of the simulation conditions. Once an exciton is generated, it is able to (1) diffuse to and quench at a defect (red arrow in

Figure 5-6A), with a characteristic time $\tau_q = {L_s}^2/\pi^2 D$.[21] We use a diffusivity of D = 8 cm^2 s^{-1} to be consistent with the transient absorption studies, above.[113, 128] The exciton may (2) dissociate at the C_{60} heterojunction, provided that the SWCNT is in contact with C_{60} (yellow arrow). The top layer is always in contact with C_{60}, and in order to simulate interfacial roughness, each SWCNT layer below the top layer has a decreasing chance of being in contact with C_{60} according to $P(n) = \exp(-\alpha(N-n))$ where *n* is the layer number, *N* is the top layer, and α is a free parameter we set to a value of 3 so that the fraction of SWCNT exposed to C_{60} is consistent with the bathochromic shift measurements of Ferguson et al.[107] Measurements indicate that the dissociation time τ_d is ≤ 120 fs. . The simulations are not sensitive to τ_d provided that τ_d << τ_t; therefore, we use a τ_d of 120 fs Finally, the exciton may (3) hop to an adjacent SWCNT with characteristic time $\tau_t = 1000$ fs (blue arrow).[129-130] Each SWCNT has between two and four neighbors, one on the layer above (provided the SWCNT is not in the top layer), two in the same layer, and one below (provided the SWCNT is not in the bottom layer). Excitons are allowed to move through the film until they are quenched or dissociated, and the total number of dissociated excitons are summed to calculate the internal QE for that layer. The external QE is the sum of the internal QE for all layers, divided by the number of photons entering the device.

We calculate the external QE (**Figure 5-6B**) as a function of thickness for various n_d ranging from 3.3 to 67 μm^{-1}, covering the range of n_d measured via Raman and transient absorption spectroscopy. The exact reproduction of the experimentally measured external QE curves is not realistic given the unknown degree of defect clustering in experiments and other non-idealities such as the presence of small bandgap impurity SWCNTs,[131] which are not present in the simulation. Nonetheless, the simulated QE closely reproduces the experimentally observed trends. For example, the simulated external QE rises, peaks at a s-SWCNT layer thickness of between 4-6 nm, and then falls – consistent with experiments (**Figure 5-5B**) and reports from elsewhere.[25, 36, 110] Moreover, increasing n_d in the simulations significantly decreases the peak external QE by reducing the average time an exciton lives before finding a defect and quenching.

A particularly instructive parameter that can be extracted from simulations is the exciton harvesting depth, L_H. L_H is the distance from the C_{60} interface at which the internal QE decreases by a factor of e. The simulations indicate that L_H is only 3 nm for s-SWCNTs matching the characteristics of **s-SWCNT 1** with an average length of 451 nm and an n_d = 7 um^{-1}. The short L_H is consistent with our previous transient absorption studies, which have shown that excitons undergo inter-SWCNT transfer 1-2 times during their lifetime.[116-117, 131]

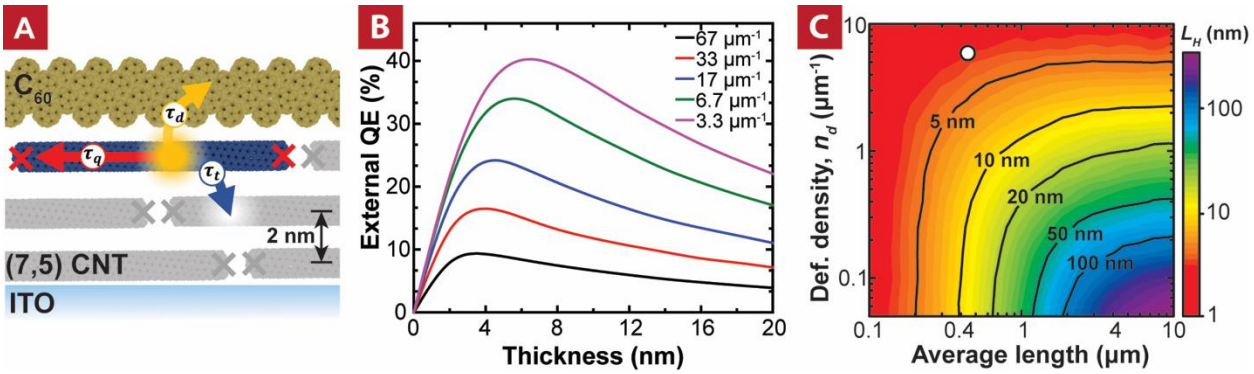

Figure 5-6 (A) Illustration of exciton transfer processes included in the diffusion limited contact quenching Monte Carlo model. Excitons are generated on s-SWCNTs of random length and may quench at defects with segment length-dependent characteristic time $\boldsymbol{\tau_q}$, dissociate at the C_{60} interface with characteristic time $\boldsymbol{\tau_d = 120\ fs}$, or transfer to other s-SWCNTs with characteristic time $\boldsymbol{\tau_t = 1000\ fs}$. **(B)** Simulated external QE as a function of s-SWCNT thickness for five n_d. **(C)** Simulated exciton harvesting depth. L_H, as a function of average s-SWCNT length and defect density. The white circle represents an estimate of the harvesting depth for the unreacted s-SWCNT 1 sample in this work.

Ideally, L_H should be similar to or exceed the absorption length, L_A, in high performance bilayer devices. Wu et al. have estimated that for (7,5) s-SWCNTs, L_A is 10 nm for monochromatic photodetector applications and is 100 nm for broadband AM1.5G photovoltaics applications.[115] We have used simulations to predict how increasing both the average length of the s-SWCNTs and decreasing n_d might increase L_H from 3 nm to more closely match L_A in the range of 10-100 nm. Towards this end, **Figure 5-6C** displays L_H as a function of mean s-SWCNT length and the added defect density, n_d. Contours corresponding to L_H = 5, 10, 20, 50, and 100 nm are displayed, in comparison to **s-SWCNT 1**, labeled by a white circle. Because defects create additional segments, the contours roughly follow iso-$\langle L_s \rangle$ curves; for example, ensembles

with average length and defect concentration 400 nm and 0.1 μm^{-1} exhibit the same L_H as those with 10,000 nm and 2.5 μm^{-1} – in both cases yielding a L_H of about 10 nm. Accordingly, improving L_H is possible by either increasing the average length of the initial distribution or decreasing the defect concentration. However, due to end defects, decreasing defect density below the inverse of the average length provides diminishing returns on improvement of L_H. Similarly, increasing average length above the inverse of defect density only produces mild improvement of L_H. The simulations predict that, in the absence of other exciton loss mechanisms, an L_H of 10 nm can be achieved by decreasing n_d to 0.4 μm^{-1} with the current length distribution, or increasing the average length to 1000 nm and decreasing the defect density to 1 μm^{-1}. For the larger L_H = 100 nm required to meet L_A = 100 nm for AM1.5G harvesting, our model predicts that average lengths on the order of 5 μm and defect density as low as 0.2 μm^{-1} are necessary.

Both the experiments and simulations presented here indicate that current, state-of-the-art, solution-processed s-SWCNT-based photovoltaic devices are limited by poor exciton harvesting efficiency because defect-induced exciton quenching necessitates films that are <5 nm thick that are weakly absorbing. Improving the exciton harvesting efficiency, and therefore device performance, should therefore focus on decreasing this defect density, while also increasing the length of the s-SWCNTs, so that thicker films can be utilized to harvest more light. Both of these objectives might be met by decreasing dispersal sonication time and/or power, development of less destructive de-bundling techniques such as shear-force mixing,[132] improved crystallinity of as-synthesized s-SWCNT material, and/or post sorting defect repair.

SUPPORTING INFORMATION

Preparation of s-SWCNTs.

Poly(9,9-dioctyl-fluorene-2,7-diyl) (PFO) wrapped (7,5)-enriched s-SWCNTs are prepared and used to fabricate the s-SWCNT layer of heterojunction devices following procedures outlined in our previous work.[14] First, (7,5)-SWCNTs are selectively isolated from as-produced heterogeneous powders of s-SWCNTs, using methods adapted from those previously developed by Nish et al.[126] PFO purchased from

American Dye Source (ADS329BE Lot#15H006A1) is dissolved in toluene (Fisher Scientific, ACS grade) at a concentration of 1 mg mL^{-1} by magnetic stirring and heating at 80 °C. Heterogeneous SWCNT powder purchased from Southwest Nanotechnologies (Lot#SG65i-L55) is added to the PFO solution to form a 0.5 mg ml^{-1} s-SWCNT and 1 mg ml^{-1} PFO mixture. Next, 70 ml of the above solution is sonicated using a Fisher sonic dismembrator model 500 horn sonicator (400 W) at 35% amplitude for 20 minutes, in which the vial of SWCNT solution is cooled by immersion in a water bath. The resulting dispersion is centrifuged with a ThermoFisher WX Ultra series centrifuge at 41,000 rpm (300,000 g) for 10 minutes. The top 80% of the supernatant is retained and filtered through a 5 μm PTFE filter to remove undissolved impurities. The s-SWCNT pellets that form at the bottom of each centrifuge tube are collected and mixed with fresh PFO solution to repeat the above process 3 times. The combined supernatant is transferred to a 500 ml round-bottom flask and distilled under a reduced pressure with a rotary evaporator (IKA® RV 10).

The resulting blue-green s-SWCNT powder is then collected and is rich in excess PFO. In order to remove this excess PFO, the powder is dissolved in boiling tetrahydrofuran (THF) under magnetic stirring. The dispersion is then centrifuged at 25,500 rpm (50,000 g) at 4 °C for 24 hours, which selectively pellets s-SWCNTs, preferentially leaving free PFO in solution. The precipitated s-SWCNT pellet is then redispersed again in THF by heating and mild tip sonication (10% amplitude, < 1 min) and centrifuged for 12 hours. This process is repeated for 4-5 cycles until the PFO to s-SWCNT mass ratio in the precipitate is about 1:1 as assessed by absorbance spectroscopy using methods outlined in our previous work.[84] Finally, the s-SWCNT powder is collected and dispersed in ortho-dichlorobenzene (ODCB) by using mild tip sonication (10% amplitude, < 2 min). These s-SWCNTs are named **s-SWCNT 1**.

Preparation of aryl-functionalized SWCNTs (aryl-SWCNTs).

Aryl functionalized SWCNTs are prepared with five different functionalization densities, via solution-phase diazonium chemistry.[18] In short, 20 ml of 1 μg ml^{-1} **SWCNT 1** in ODCB is added into a three-neck round-bottom flask equipped with a reflux condenser and is purged for 20 minutes by flowing nitrogen. 4-nitroaniline (Sigma) is dissolved in 10 ml of acetonitrile (Fisher) and added to the above s-

SWCNT dispersion. The concentration of 4-nitroaniline is varied from 2.3, 23, 510, 23000, to 41000 μg ml^{-1} in order to affect the density of aryl functional groups on the s-SWCNT sidewalls to create **s-SWCNT 2** through **s-SWCNT 6**. After flowing nitrogen gas for another 15 minutes, isoamyl nitrite (Sigma) is added at a molar ratio of isoamyl nitrite:4-nitroaniline of 1.5:1. The reaction then proceeds in an oil bath at 60 °C for 23 hours in dark conditions. Afterwards, the reactants are poured into 40 ml of dimethylformamide (DMF) and centrifuged at 25,500 rpm (50,000 g) for 4 hours, which selectively pellets the s-SWCNTs. To remove excess diazonium, the precipitated aryl-SWCNTs are redispersed in DMF by bath sonication and centrifuged at 25,500 rpm (50,000 g) for 2 hours. This washing process is repeated for 4-5 times until the supernatant turns colorless. The aryl-SWCNTs are dried under vacuum and dispersed in ODCB using a mild tip sonication (10% amplitude, < 2 min).

Characterization of thin film optical absorbance spectra.

Absorption spectra of thin films of s-SWCNTs are measured to quantify the reduction of the s-SWCNT optical cross-section at the (7, 5) bandgap transition at 1050 nm that occurs with increasing functionalization density.[111] Thin films of constant thickness are created via the vacuum filtration (Advantec) of a controlled concentration and volume of s-SWCNT solution. Al_2O_3 membranes (Anodisc 13, mean pore size: 0.2 μm, diameter: 13 mm) are used as the filter. After the s-SWCNT film forms on the membranes, DMF is added to the apparatus until the filtrate is colorless. The Al_2O_3 membranes are then etched in 1M NaOH solution to obtain freestanding SWCNTs films. The films are transferred onto glass substrates via floating transfer from deionized water and rinsed in three successive deionized water baths.

Microscopy.

The morphology of s-SWCNT thin films prepared via vacuum filtration and doctor-blade casting (see below) are characterized using a LEO 1530 scanning electron microscopy (SEM) with an electron beam energy of 3 keV. Atomic force microscopy (AFM) images are taken in tapping mode using a Bruker Multimode 8 instrument and used to obtain the length distribution of the as-prepared s-SWCNTs.

Raman spectroscopy:

Raman spectra are collected at 1600 different points spread over a 40 μm × 40 μm area using a Thermo Scientific DXRxi Raman Imaging Microscope with a λ = 532 nm, 1.4 mW laser focused to a spot size of 700 nm. The spectra are collected with a measurement time of 0.025 s per spectrum and then averaged over the entire area. Sidewall binding of aryl functional groups introduces sp^3 defect sites on the sp^2 carbon network, which leads to the appearance of the symmetry-breaking, disorder-induced Raman phonon mode (D peak, ~1300 cm^{-1}).[133] The intensity of the Raman D peak with respect to the tangential stretching mode of the sp^2 carbon lattice (G peak, ~1590 cm^{-1}), i.e. the I_D/I_G ratio, is often used to quantify the defect concentration of graphitic materials[125, 134] and is of interest, here.

Transient absorption.

Transient absorption measurements are conducted using a custom two-dimensional white-light spectrometer previously described elsewhere.[117-118] Briefly, the 300 μJ per pulse output of a Ti:Sapphire regenerative amplifier (800 nm, 150 fs, 1 kHz; Spectra Physics Spitfire) is split equally into pump and probe beams. In both paths, the fundamental is attenuated by a combination of an iris and a neutral density filter to ~1 μJ per pulse and focused into an undoped yttrium aluminum garnet (YAG) crystal to generate a supercontinuum. The residual fundamental in the pump beam is spatially filtered out in a prism compressor used to correct for temporal dispersion. Both the pump and probe pulses are ~100 fs in duration, as determined by optical Kerr effect cross-correlation of the supercontinuum with the fundamental in CaF_2. The pump fluence is controlled to remain in the single exciton regime (~$9x10^{13}$ photons cm^{-2}). The time between the pump and probe pulses is controlled by a mechanical delay stage (Newport IMS600PP). The polarization of the pump pulse relative to the probe pulse is set by a broadband polarizer (Meadowlark). The pump and probe beams are focused in the sample solution with a f = 5 cm, 90° off-axis parabolic mirror. The transmitted signal, heterodyned by the probe beam, is dispersed with a 150 mm focal length spectrometer (Acton SP-2150) onto an InGaAs photodiode array (Princeton Instruments OMA-V:512−1.7).

Transient absorption spectra are calculated by chopping the pump pulse at 500 Hz (Newport 3501) and calculating $\Delta OD = -\log\frac{I_{pump\ on}}{I_{pump\ off}}$ from shot-to-shot, where $I_{pump\ on/off}$ is the intensity of the dispersed probe when the pump is unblocked/blocked, respectively.

Fabrication of photovoltaic devices.

Devices are fabricated by closely following procedures established in our previous work.[14] Briefly, indium tin oxide (ITO)-coated glass substrates (15 Ω/square, Prazisions Glas & Optik) are first cleaned with acetone and isopropyl alcohol, followed by a short UV-ozone treatment. Poly(3,4-ethylenedioxy-thiophene) polystyrene sulfonate (PEDOT:PSS, Clevios Al 4083) is spin-cast on the ITO substrates at 4,000 rpm for 1 minute and annealed at 120 °C for 15 minutes in ambient. The s-SWCNTs are deposited via a doctor blading technique, in which 8 µl of s-SWCNTs in ODCB solution (~50 µg ml^{-1}) are dropped onto the substrate on a hotplate set to 135 °C, and a steel blade is drawn across the substrate approximately 500 µm above the surface. The film thickness can be tuned by repeating the above process multiple times. The resulting s-SWCNT film is annealed at 135 °C for 15 minutes in a nitrogen atmosphere and soaked in boiling toluene for 30 minutes to remove excess PFO and other adsorbates. After drying in an air stream, a 85 nm thick layer of C_{60} is deposited on the top of s-SWCNT film in high vacuum via vacuum thermal evaporation, followed by 10 nm of bathocuproine (BCP). A 120 nm Ag film is deposited through a shadow mask to define a circular cathode. The effective area of each device is 0.785 mm^2, as determined by the Ag electrode area.

Quantifying s-SWCNT film thickness in photovoltaic devices.

To determine the thickness of the doctor-bladed s-SWCNT films, an optical transmission spectrum is collected from a 1 mm spot-size, immediately adjacent to each device. A broad polynomial background is subtracted to remove the absorption from the ITO layer. The film thickness is then calculated by integrating the total S_{11} peak area for the (6,5), (7,5), (7,6) and (8,6) s-SWCNTs and then using the optical

cross-sections data of Streit et al.,[56] adjusting for the relative contribution of each s-SWCNT species, and the reduction in optical cross-section with increasing aryl-functionalization measured above.

External QE measurement.

The external QE is measured with a custom two light source optical setup. A xenon lamp equipped with a KG5 colored glass bandpass filter to remove strong emission lines above 800 nm is used to provide ultraviolet/visible light. A tungsten lamp is used to provide the visible/near-infrared light. These two light sources are combined by using a 50/50 beam splitter and then passed through a monochromator. Long pass filters are sequentially used to prevent excitation of the sample by higher energy multiples of the monochromator output. We specifically use long pass filters with specific cut-offs of 420, 680, and 1090 nm, in addition to a near-infrared-specific grating for wavelengths greater than 1090 nm. The beam is modulated via a mechanical chopper, and the intensity is quantified using Newport 818-UV and 818-IR detectors, which are calibrated over the range of 300–1088 nm and 800–1300 nm, respectively. The device photocurrent is measured using a lock-in amplifier, and divided by the photon flux measured by the photodetectors to calculate the external QE.

CHAPTER 6: IMPROVING PHOTOVOLTAIC PERFORMANCE BY AVOIDING HARSH SONICATION

Adapted from:

Shea, M.J., Wang, J., Flach, J.T., Zanni, M.T., and Arnold, M.S., Carbon nanotube length effects on photovoltaic performance, *In Preparation*

The author conceived of and carried out experiments as well as analyzed data. The author recognizes Jialiang Wang for Raman spectroscopy measurements, and Jessi Flach and Dr. Martin Zanni for their measurements of transient absorbance.

SONICATION EFFECTS ON NANOTUBE LENGTH

While the efficiency of excited state ("exciton") dissociation into free carriers at a s-SWCNT/C_{60} heterojunction is high,[34] exciton diffusion between individual s-SWCNTs is slow. Due to the short excited state lifetime of several ps, excitons only travel a few nm through the film before they are quenched at defects or nanotube ends.[17] Recently, we have studied the effects of defect density on the peak external quantum efficiency (EQE) of bilayer s-SWCNT/C_{60} photovoltaic cells using experiment and Monte Carlo simulations.[20] In that work, we intentionally and controllably added sp^3 defects via diazonium chemistry and observed the deleterious effect of sidewall defects on external quantum efficiency (EQE). Here, we show improved device performance associated with increasing average length and decreasing sidewall defect density by controlling the processing methods used to isolate s-SWCNTs.

Most s-SWCNT isolation methods rely on tip sonication to achieve separation. Tip sonication is a highly energetic process that is known to introduce sidewall defects on the s-SWCNTs and decrease mean length.[135] Recently, shear force mixing (SFM) has been used to isolate s-SWCNTs, resulting in longer ensemble lengths and increased photoluminescence (PL) quantum yields (QY).[132] In this work, we compare nearly monochiral (6,5) s-SWCNTs isolated *via* SFM and sonication, and incorporate them into photovoltaic devices as the photoabsorbing layer. We find that the long s-SWCNTs isolated by SFM exhibit increased external QE compared to shorter, sonicated ensembles, and show that devices fabricated with severely shortened s-SWCNTs have lower EQE, as well as fill factor (FF) and open-cirucit voltage. We compare the predictions of our Monte Carlo EQE model to defect densities obtained *via* transient

absorbance and photoluminescence. This work illustrates the importance of choosing s-SWCNT isolation methods that reduce sidewall defect density and increase length for efficient photovoltaic performance.

We prepare solutions of polymer-wrapped (6,5) s-SWCNTs using a method adapted from those of Ozawa et al.[30] and Graf et al.,[132] in which the copolymer poly[(9,9-dioctylfluorenyl-2,7-diyl)-alt-co-bipyridine)] (PFO-BPy) and raw nanotubes are mixed in toluene solution and horn-tip sonicated for 10 minutes ("Moderate Sonication,") or 1 hour ("Excessive Sonication"). In our previous work, we have followed dispersion procedures closest to sample S. Alternatively, the mixture is shear force mixed to isolate s-SWCNTs. The resulting slurries are centrifuged to remove soot and large particles. The supernatants were collected and successively precipitated in tetrahydrofuran to remove excess PFO-BPy as in our previous work,[84] before finally dispersing the s-SWCNTs in ortho-dichlorobenzene using mild, brief (< 30s) horn-tip sonication. (See Supporting Information)

The length distribution of each solution was measured by atomic force microscopy (AFM) in which a sub-monolayer of nanotubes was spin-cast onto clean SiO_2/Si wafers from a dilute (<1 μg/mL) solution in toluene. Typical AFM images, and their respective length distributions, are displayed in **Figure 6-1A**. The SFM dispersion contains significantly longer nanotubes, with a mean length of 1090 nm, compared to 480 nm for sample MS and 310 nm for sample ES. The normalized absorbance of each solution in toluene is displayed in **Figure 6-1B**. Peaks correspond to (6,5) S_{11} and S_{22} transitions at 1000 and 580 nm, respectively, as well as phonon side bands[8] at 850 nm. Other peaks correspond to minority chiralities in solution, most notably (6,4) at 940 nm. The region between 1100 and 1200 is dominated by small contributions from larger diameter nanotubes, but is complicated by the strong toluene absorbance feature near 1150 nm, precluding precise quantification. However, the absorbance in this region is similar in all three solutions, suggesting that large diameter impurity concentrations are not appreciably different in solutions ES, MS, and SFM. We estimate that (6,5) nanotubes account for ~95% of the s-SWCNTs in solution, with minority (6,4) and (7,5) nanotubes accounting for the balance.

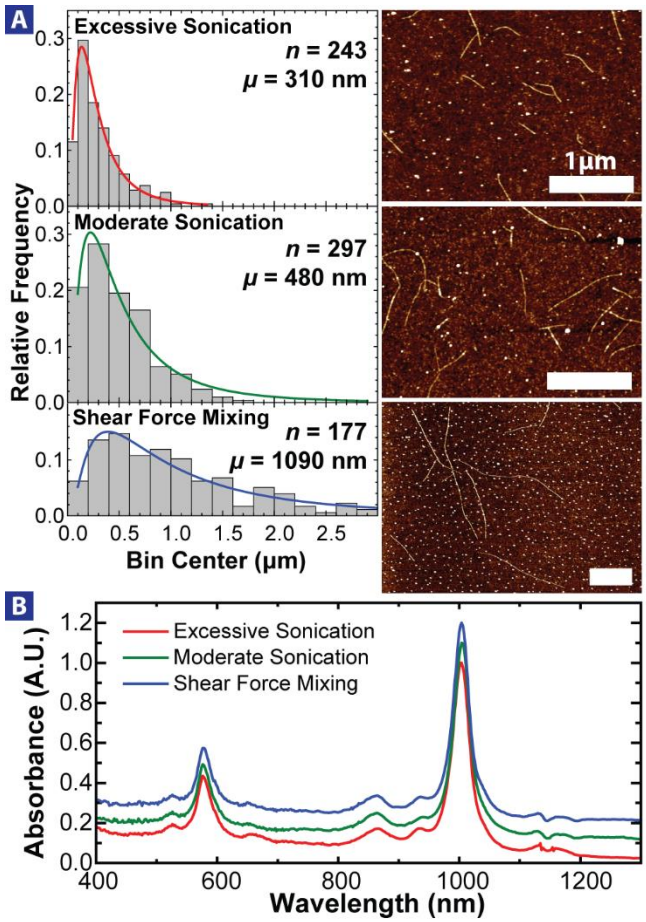

Figure 6-1. (A) Length distributions of solutions which have undergone excessive sonication (red), moderate sonication (green), and shear force mixing (blue) measured by AFM. (right) **(B)** Optical absorption spectra of s-SWCNT solutions in toluene offset by 0.1 units. The chirality distributions of the three solutions are nearly identical, and contain 95% (6,5) nanotubes. The feature near 1150 nm is due to convolution with an absorption peak of toluene.

LENGTH EFFECTS ON S-SWCNT EQE

We fabricate s-SWCNT/C_{60} photovoltaic devices using techniques described in our prior work.[14] Briefly, solutions of s-SWCNTs are blade-cast onto clean ITO substrates, and fullerene-C_{60} is evaporated as the exciton dissociating and electron transporting layer. Bathocuprione and silver make up the top contact. We measure the EQE of these devices as a function of wavelength (**Figure 6-2A**) and nanotube layer thickness. (**Figure 6-2B**) EQE peaks at the S_{11} of the (6,5) s-SWCNT near 1000 nm, and is modulated by the C_{60} thickness. We chose a C_{60} thickness of 75 nm to maximize the optical intensity at the (6,5) S_{11}.[14, 80, 86] The plot of EQE versus device thickness, measured by optical absorption using the cross sections of

Sanchez et al.,[136] is observed to increase rapidly to a maximum, usually around 5 nm, then decrease slowly. We attribute this behavior to the interplay between increasing optical absorbance in thicker films, and decreasing exciton diffusion.[80] Short, defective nanotubes are known to reduce exciton diffusion length by trapping or quenching excitons before they can reach the heterointerface and dissociate.[17, 20] Devices fabricated from the shear force mixed solution, which contains the longest nanotubes, display the highest peak EQE, approaching 50%, which decreases to 38% and 28% as sonication intensity increases. Since the starting material, chiral distribution, (**Figure 6-2B**) and polymer content (**Figure 6-S1**) of these films are identical, we ascribe the improvement in EQE to the longer, lower defect density nanotubes purified by shear force mixing. In addition, we observe that the slope of the EQE versus thickness in the thin film regime is lower in the excessively sonicated sample, indicating that the exciton dissociation efficiency is lower in this sample. Wang et al. note a similar trend in highly defective s-SWCNTs, and attribute this behavior to exciton quenching at nanotube ends and defects that occurs on faster timescales than even exciton dissociation.[20]

In our previous work, we developed a model to describe exciton transport through a s-SWCNT film and predict EQE as a function of defect density.[20] When we apply that model to the peak EQE observed in **Figure 6-2A**, we predict that for EQE to drop by the factor of two that we observe, the total defect density must increase by a factor of four. (**Figure 6-S2**) The total defect density n_d is the sum of the number of end defects n_e and the number of sidewall defects n_s. Since the number of s-SWCNT ends is inversely proportional to the mean nanotube length, we expect that the density of end defects increases by a factor of three in the shortest ensemble as compared to the shear force mixed sample. The model therefore suggests that excessive sonication not only shortens nanotubes, but increases the number of sidewall defects as well.[20]

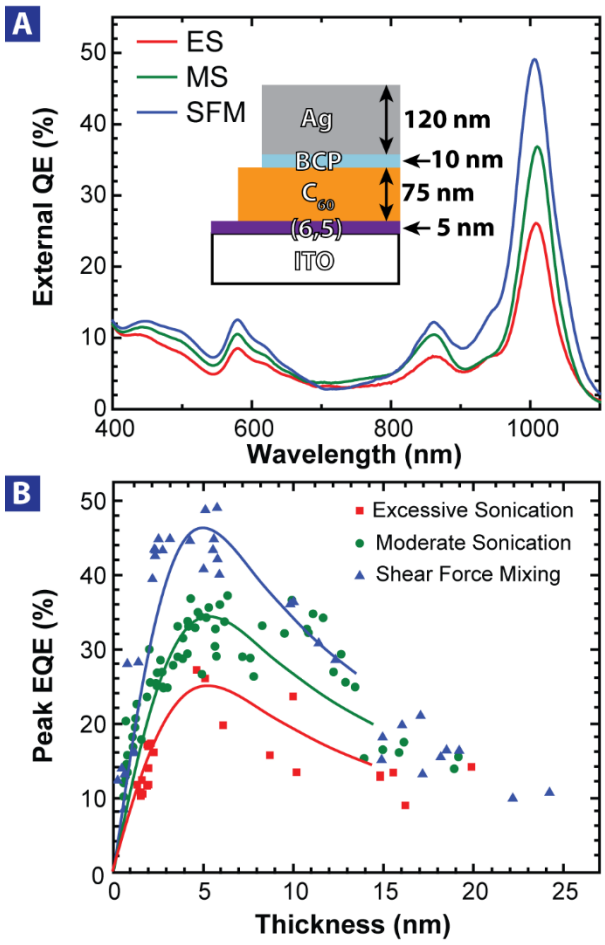

Figure 6-2. (A) EQE as a function of wavelength for representative devices fabricated from solutions that underwent excessive sonication (red), moderate sonication (green), and shear force mixing (blue). Inset: Schematic of devices fabricated for this study. **(B)** Measured peak EQE at 1000 nm as a function of thickness. The lines are guides for the eye. The maximum EQE occurs near 5 nm for all samples, but decreases as processing intensity increases.

OPTICAL METHODS TO QUANTIFY DEFECT DENSITY

Precisely measuring the defect density, however, remains a challenge. We use Raman spectroscopy, transient absorption, and photoluminescence to attain information about the defect density. While Raman spectroscopy is often used to qualitatively identify defects present in carbon nanomaterials, quantifying defect density using Raman is difficult when defects are sparse.[20] We measure nearly identical I_D/I_G ratios of 0.04±0.01, 0.06±0.02, and 0.05±0.01 for the excessively sonicated, moderately sonicated, and shear-force mixed nanotubes, respectively. (**Table 6-1**) Even when the defect density is too low to quantify *via* Raman, the effect on EQE is significant. Instead, we conduct transient absorbance (TA)

measurements on the three solutions to observe the rate of exciton decay in each nanotube ensemble. The measured change in optical density (ΔOD) of a solution with optical density OD_0 decays according to a stretched exponential with characteristic time τ_0 according to the relation

$$\Delta OD(t) = OD_o \exp\left(-\left(\frac{t}{\tau_0}\right)^{\frac{1}{2}}\right). \quad \textbf{[6-1]}$$

We fit equation **(1)** to the data in **Figure 6-3A**, and extract values of τ_0 of 4.2±0.1, 3.0±0.1, and 2.1±0.2 ps, respectively. This behavior is consistent with diffusion-limited quenching kinetics, in which longer exciton lifetime corresponds with fewer defects, longer lengths, or both.[21, 113] When diffusion to, and quenching at, defects is the dominant exciton recombination mechanism, and defects are randomly distributed, the exciton population decreases according to

$$\varphi(t) = \int_0^\infty n_d \exp(-n_d x) \exp(-n_d \pi^2 D t)\, dx \quad \textbf{[6-2]}$$

where n_d is the defect density and D is the diffusion coefficient.[21]. Using a diffusion coefficient of 8 cm^2/s, and we estimate total defect densities (including ends) that decreases from 12.1±0.6 to 9.9±0.2 to 8.3±0.1 μm^{-1} as processing intensity decreases. Integrating equation **(2)** as a function of time gives a measure of the relative photoluminescence quantum yield (QY), which matches favorably with the measured QY discussed next.

Another approach to assess defect density is photoluminescence QY. We show photoluminescence spectra of solutions excited at the (6,5) S_{22} at 580 nm in **Figure 6-3B**. The photoluminescence is corrected for absorbance and represents the relative QY of each solution. We observe a strong trend of increasing QY with increasing length, also noted by Graf et al. for nanotubes separated using shear-force mixing.[132] In addition, we observe changing peak structure away from the main S_{11} emission peak, often attributed to doping,[137] phonon sidebands,[138] or defects.[139] When normalized to the main S_{11} emission these peaks are strongest in the shortened samples, suggesting that these samples have higher levels of defects and/or doping, both of which are known to decrease exciton diffusion length in photovoltaic devices.[17] Specifically, the X_1 peak, located roughly 1050 cm^{-1} below the S_{11}.[140] may be used to identify the presence

of defects associated with the defect-induced D-band with much greater precision than Raman spectroscopy. (See **Figure 6-S4**) We find that the X_1/S_{11} ratio decreases from 0.22 to 0.13 to 0.09 as the processing intensity decreases. A summary of the optical and optoelectronic properties for each solution is given in **Table 1**. While neither transient absorbance nor PL provide a direct measure of defect density, both show that defect density is lowest in samples purified *via* shear force mixing, establishing a qualitative link between EQE and sample preparation method.

In a recent report, Mallajosyula et al. described the performance of devices incorporating PFO-BPy-wrapped (6,5) nanotubes in comparison to poly(9,9-dioctylfluorene-2,7-diyl) (PFO)-wrapped (7,5), and suggested that PFO-BPy inhibits charge transfer within the device. Since the highest peak EQE we measure here outpaces even the best PFO-wrapped (7,5) nanotube devices to date,[14] we believe that the choice of wrapping polymer, once maximally removed,[84] does not limit device performance. On the other hand, we observe somewhat lower peak EQE from the (6,5) nanotubes of solution **2** in this study (~38%) compared to the (7,5) nanotubes purified by the same method in our prior work (~43%).[14] It is possible that (6,5) nanotubes in the mixed starting material from which both PFO-BPY-(6,5) and PFO-(7,5) are isolated are simply shorter or have more defects on average.

Table 6-1. Summary of s-SWCNT optical and optoelectronic properties.

Method	Time	$\langle L \rangle$ (nm)	I_D/I_G	n_d (T.A.) (μm^{-1})	$\int \frac{\Delta OD}{OD} dt$ *normalized*	S_{11} PLQY *relative*	X_1/S_{11} (PL)	peak EQE (%)
sonication	1 hour	310	0.04	12.1	0.56	0.62	0.22	28
sonication	10 min	480	0.06	9.9	0.79	0.72	0.13	38
shear force	20 hour	1090	0.05	8.3	1	1	0.09	50

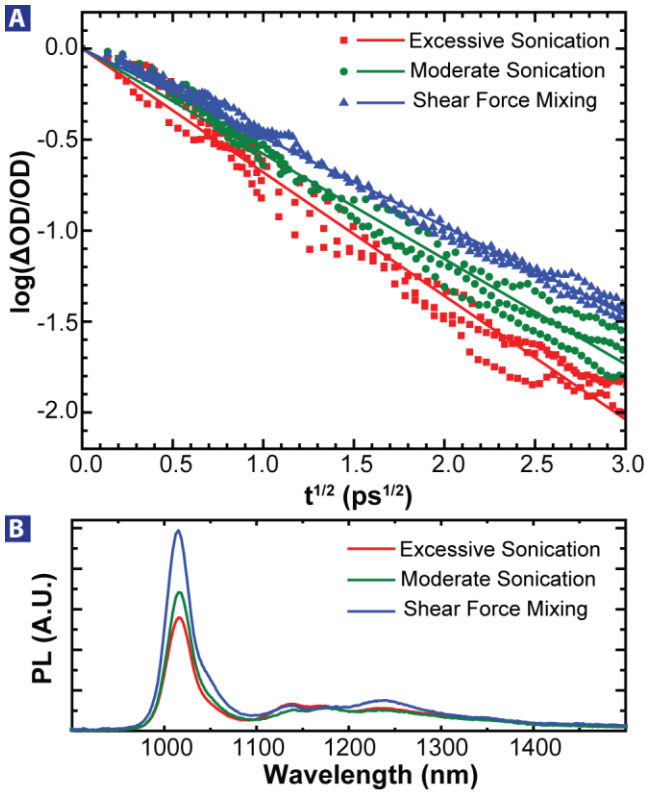

Figure 6-3. (A) Transient absorption of solutions 1, 2, and 3 in ortho-dichlorobenzene is plotted as a function of $t^{1/2}$. Faster decay is indicative of shorter mean defect free paths for excitons. **(B)** Photoluminescence spectra of toluene solutions of 1, 2, and 3 from excitation at (6,5) S_{22} at 580 nm.

LENGTH EFFECTS ON PV PERFORMANCE

Next, we measure current density versus voltage (*J*-*V*) curves for these devices under illumination of a near-infrared light source with wavelength range 800-1200 nm. We chose this range to avoid complication due to the absorbance of C_{60} below 650 nm. Under this illumination, excitons are solely generated in the s-SWCNT film, allowing us to study more carefully the role of preparation method on the open circuit voltage (V_{OC}) and fill factor (*FF*). We plot the *FF* and *Voc* versus log-J_{SC} for devices with s-SWCNT thickness near the optimum (~5 nm) over a wide range of light intensity in **Figure 6-4A-B**. At all J_{SC}, the devices from excessively sonicated s-SWCNTs have lower *FF*. Though there is significant spread in the data for the moderately sonicated and shear force mixed nanotubes, at low J_{SC} the devices from shear force mixed nanotubes display higher *FF* and V_{OC}. The V_{OC} dependence on J_{SC} is given by

$$V_{OC} = nk_BT \ln\left(\frac{J_{SC}}{J_S}\right), \quad \textbf{[6-3]}$$

where n is the ideality factor, k_B is Boltzman's constant, T is absolute temperature, and J_S is the saturation current density. Since the slope $dV_{OC}/d(\ln J_{SC})$ is constant between device sets, the offset causing lower V_{OC} in device set **1** may be attributed to an increase in J_S for these devices. J_S may be expressed as a function of the energy offset ΔE_{HL} between donor highest occupied molecular orbital (HOMO) and acceptor lowest unoccupied molecular orbital (LUMO),

$$J_S \approx J_{S0} \exp\left(-\frac{\Delta E_{HL}}{k_BT}\right), \quad \textbf{[6-4]}$$

where J_{S0} is a temperature-independent term related to the density of states and recombination rate constant. An increase in J_{S0} or a decrease in the effective ΔE_{HL} due to interfacial disorder or traps leads to an increase in J_S and a decrease in V_{OC}. Though equation (**3)** is often cited in literature, it relies on the assumption that photocurrent generation is constant with voltage. This is not always the case in real devices, as we next show. The fill factor of photovoltaic cells under illumination depends on series and shunt resistance, as well as charge generation, recombination, and collection. We plot the current density normalized to the short circuit current density (J_{SC}) versus the voltage normalized to open circuit voltage in **Figure 6-4C**.(See **Figure 6-S6**) The series resistance is consistently small, typically 0.5 to 2 Ω-cm^2; furthermore, the zero-bias slopes are low, indicating that shunt resistance is large and does not vary between data sets. However, under forward bias, we observe a significant difference in the normalized photocurrent between the three devices. Devices fabricated with short nanotubes have photocurrent that significantly degrades as V approaches V_{OC}, giving rise to a poor fill factor in these devices.

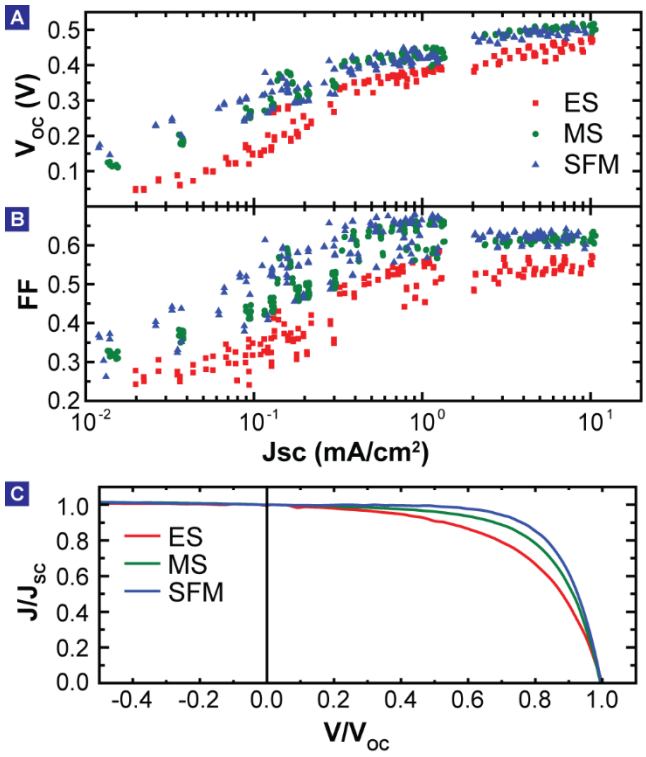

Figure 6-4. (A) *FF* and **(B)** V_{OC} are plotted versus the log of J_{SC} for near-infrared illumination of devices. **(C)** Normalized J-V plot showing decrease of forward bias photocurrent in short ensembles.

The relationship between the degradation of photocurrent under forward bias and the behavior of excitons and free charges at donor/acceptor interfaces has been the focus of several recent studies. Giebink et al. provide a description of voltage-dependent polaron pair dissociation efficiency which decreases photocurrent under forward bias.[94, 141] When excitons reach the C_{60} interface, they form a transitional polaron pair spanning the interface. Splitting the polaron pair into free charges is a dynamic process that depends on the mobility of the charges and the local electric field. In short, higher mobility improves the extraction of charges from the polaron pair, while the local electric field under forward bias may weaken the driving force for dissociation, even reversing to favor recombination at sufficiently high bias. A similar relationship between charge extraction and recombination was studied by Bartesaghi et al., who found that the fill factor of a wide range of organic solar cells is related to the ratio of recombination to charge extraction.[142] Fill factor is highest when the ratio of recombination to charge extraction is small, and mobilities are high. While we expect the electron mobility in C_{60} to be independent of s-SWCNT ensemble,

the mobility of holes in the s-SWCNT film is decreased by the presence of scattering sites[143] in the form of defects and tube-tube crossings[22, 144] both of which are expected to increase in the short, heavily sonicated ensembles.

In conclusion, we have used shear force mixing to separate monochiral (6,5) carbon nanotubes with mean length 1090 nm, and compared to equivalent s-SWCNT solutions separated using tip sonication with mean lengths of 480 and 310 nm. We observe that excited state lifetimes increase and photoluminescence brightens as the length increases. In addition, we fabricate donor/acceptor planar heterojunction devices using fullerene-C_{60} as an electron acceptor and measure device characteristics for each s-SWCNT ensemble. We find that peak EQE increases from 28% to 38% to 50% as average length increases from 310 to 480 to 1090 nm. Furthermore, we describe the effect of s-SWCNT length on fill factor and open circuit voltage, and show that devices fabricated from short s-SWCNTs exhibit decreased fill factor and open circuit voltage. This work exhibits the need for long, pure, defect free s-SWCNTs in photovoltaic devices, and suggests that shear force mixing is a viable method for achieving higher EQE in s-SWCNT/C_{60} photovoltaic devices.

SUPPORTING INFORMATION

s-SWCNT preparation.

Solutions of (6,5) s-SWCNTs were prepared using a method adapted from those of Ozawa et al.[30] and Graf et al.,[132] in which the copolymer poly[(9,9-dioctylfluorenyl-2,7-diyl)-alt-co-bipyridine)] (PFO-BPy) (American Dye Source, Inc.) is dissolved in hot toluene at 2 mg/mL. Raw nanotubes (Sigma, SG65i) are added to the solution at 0.5 mg/mL. The mixture is horn-tip sonicated (Fisher Model 500, 400W) at 40% amplitude for 1 hour (**Sample 1**) or 10 minutes (**Sample 2**). Alternatively, the mixture is shear force mixed (Silverson L5M-A) at 10,000 rpm for 20 hours (**Sample 3**). Typical volumes were 70 mL for the sonicated and 600 mL for the shear force mixed samples. The sonicated samples (**1** and **2**) were accumulated in 9 batches; the shear force mixed sample (**3**) was completed in a single batch. The resulting slurries were centrifuged at 300,000 g for 10 minutes to remove soot and large bundles. The supernatant was collected

and rotary evaporated to concentrate the solutions to 60 mL. Sample 1 was further centrifuged at 150,000 g for 20 hours, to remove long nanotubes, leaving very short nanotubes in the supernatant. The resulting solutions were mixed with tetrahydrofuran (THF) at 1:1 and centrifuged for 24 hours, at which point the nanotubes were collected from the pellet. These nanotubes were redispersed in THF and centrifuged three more times, to remove excess polymer. The final ratio of the PFO-BPy to nanotubes is near 1:1. (See Supporting Information) Finally, the nanotubes are dispersed in ortho-dicholorobenzene at a concentration of roughly 100 μg/mL.

Photoluminescence.

Photoluminescence spectra were taken with a Horiba NanoLog Fluorimeter. The nanotube solutions were placed in a microcuvette (2 mm path length) and excited at 580 nm. Emission spectra cover the region from 900 to 1500 nm.

Transient absorption.

Transient absorption measurements were taken using a home-built two-dimensional white-light spectrometer, described in greater detail elsewhere.[1] Briefly, the output of a Ti:Sapphire regenerative amplifier (800 nm, 150 fs, 1 kHz, 300 uJ; Spectra Physics Spitfire) was split into pump and probe beams. A white light supercontinuum is generated on each path by attenuating the beams to ~1 uJ using a neutral density filter and an iris and then focusing into a 4 mm thick YAG crystal. The polarization of the pump beam was set parallel to the probe beams using a broadband polarizer (Meadowlark). The time delay between the pump and probe pulse was controlled using a retroreflector on a mechanical delay stage (Newport). A prism compressor was used on the pump beam path to cut out residual fundamental 800 nm light and to correct for dispersion. Both the pump and the probe pulses were ~100 fs in duration. The pump fluence is controlled to remain in the single exciton regime (~10^{13} photons/cm^2). The pump and probe pulses were overlapped on the sample using a f=5cm, 90° off-axis parabolic mirror. The probe spectrum was

dispersed with a 150 mm focal length spectrometer (Acton SP-2150) and recorded using an InGasAs photodiode array (Princeton Instruments, OMA-V:512-17). The transient absorption signal was calculated by chopping the pump pulse at 500 Hz (Newport 3501) and measuring the intensity of the probe when the pump is blocked/unblocked. We calculated $\Delta OD = -\log \frac{I_{pump\ unblocked}}{I_{pump\ blocked}}$ on a shot-to-shot basis at each time point in the transient absorption measurement.

Raman Spectroscopy.

Raman spectra are measured with Thermo Scientific DXRxi Raman Imaging Microscope with a 4mW laser (λ = 532 nm) focused on a spot size of 700 nm. The spectra are collected at 100 points and averaged over a 10 μm × 10 μm area. The intensity ratio between the disorder-induced Raman D peak (~1300 cm^{-1}) and tangential stretching of sp^2 carbon lattice G peak (~1590 cm^{-1}) is used to compare the defect density of SWCNTs with different lengths.

Device fabrication.

Devices were fabricated on UV-ozone cleaned indium tin oxide substrates by blade casting. Thicker films were achieved by consecutive casting. Subsequently, devices were submerged in a toluene bath at 120°C for 15 minutes to remove excess PFO-BPy. A 75 nm thick layer of fullerene-C_{60} (Sigma) was thermally evaporated at 10^{-7} Torr. 10 nm of bathocuproine was evaporated as an exciton blocking layer, and 120 nm of silver was evaporated through a shadow mask as a cathode, forming circular devices each with an area of 0.007854 cm^2. External quantum efficiency was measured as detailed in our previous works.[14, 80]

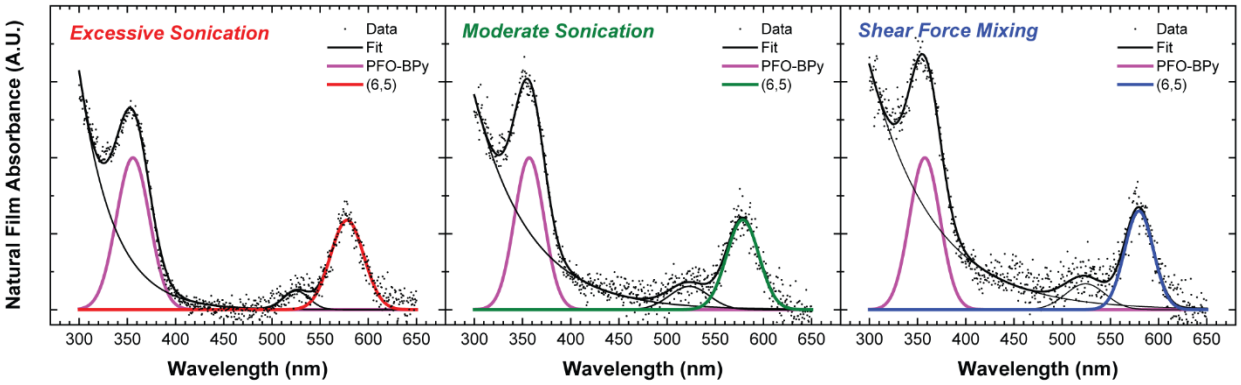

Figure 6-S1. We deposit thin films of PFO-BPy wrapped (6,5) s-SWCNTs on quartz and measure optical absorption spectra. We fit peaks corresponding to the (6,5) S_{22} and PFO-BPy for each sample. The constant S_{22}/PFO-BPy peak ratio indicates that PFO-BPy concentration does not significantly vary between samples.

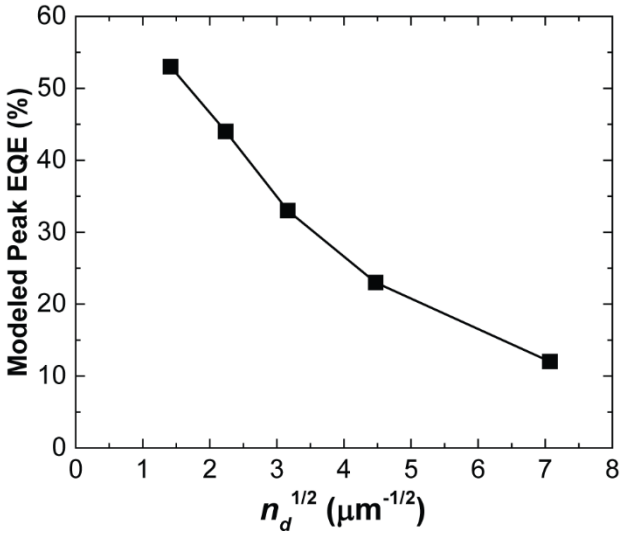

Figure 6-S2. Using the model described in our previous work,[20] we plot the peak EQE versus the square root of defect density. The model predicts that halving the EQE requires quadrupling the defect density. Relevant parameters for this model are: D = 8 cm^{2}s^{-1}, τ_{trans} = 1000 fs, τ_{diss} = 120 fs.

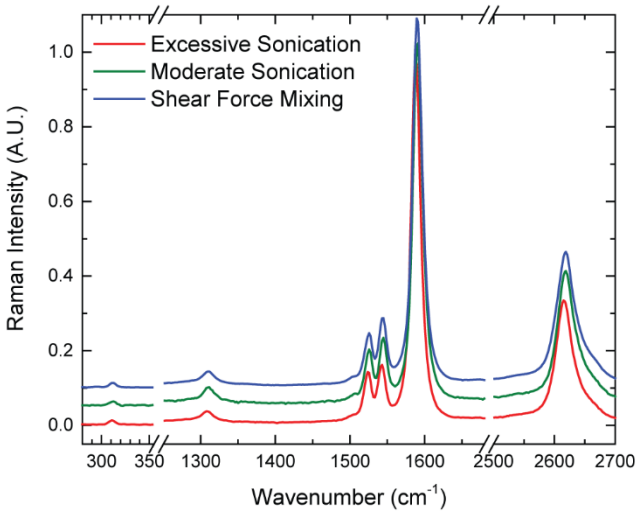

Figure 6-S3. Raman spectrum averaged over 1225 points taken over 35×35 μm^2. The I_D/I_G ratios for all three ensembles are small, ranging from 0.04±0.01 to 0.06±0.02.

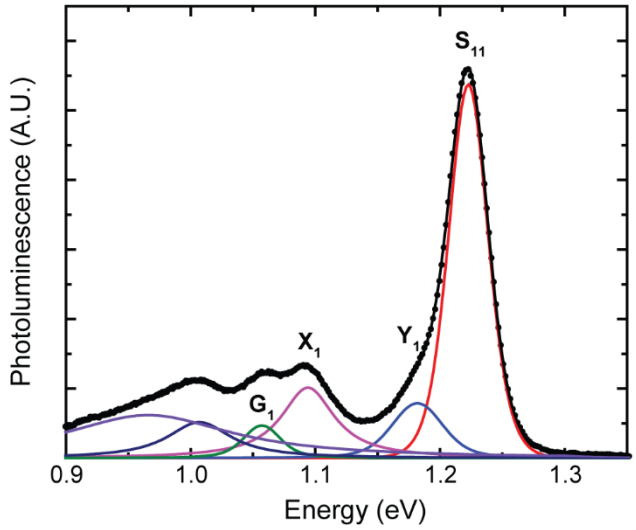

Figure 6-S4. Example PL spectrum with assigned peaks[140] used for determining X_1/S_{11} ratio.

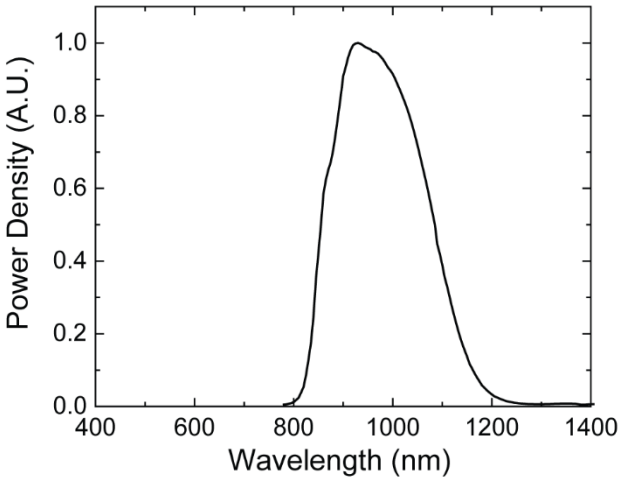

Figure 6-S5. Spectral power density of the NIR illumination used to characterize V_{OC} and *FF*. The spectrum was generated with a tungsten incandescent lamp, 1150 nm short pass filter and 800 nm long pass filter.

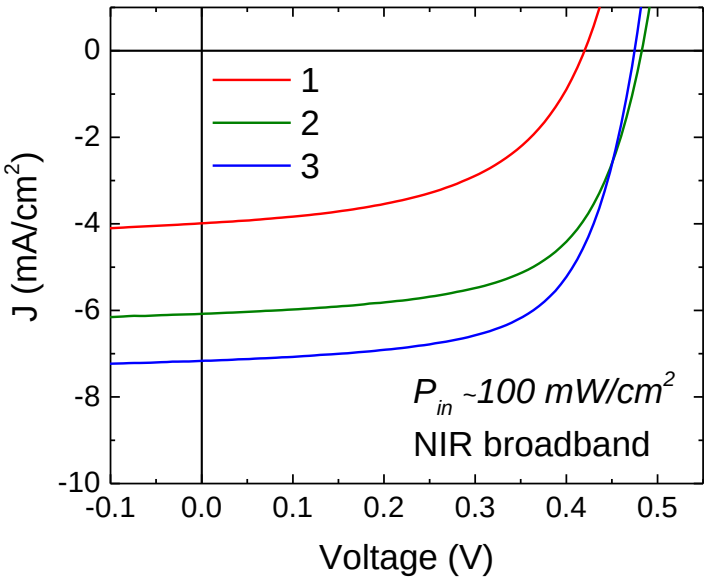

Figure 6-S6. Representative *J-V* curves for devices from solutions **1**, **2**, and **3** near 100 mW/cm^2. The intensity is approximated using a calibrated photodiode and the known spectrum of **Fig S5**.

APPENDIX A: MONOCHROMATOR

SECTION A1. HARDWARE

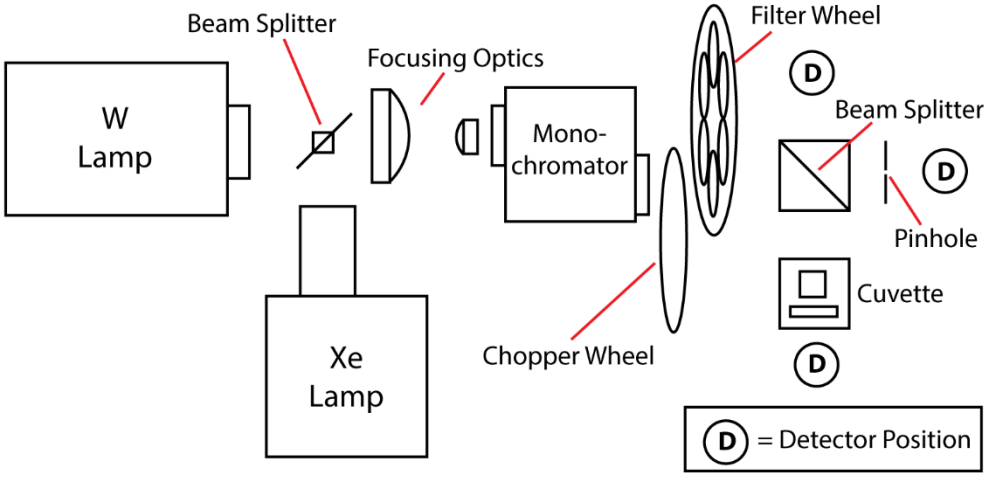

Figure A1-1. Diagram of monochromator setup with two source lamps, chopper wheel, and filter wheel used for absorbance, reflectance, and external QE measurements.

All optical and optoelectronic measurements were taken with a home-built monochromator/two-source solar simulator (See Appendix 3) setup, a diagram of which is shown in **Figure A1-1**. In this apparatus, beams from the two light sources are combined with a 50/50 aluminum polka dot beam splitter, and focused into the inlet slit of a Horiba Jobin Yvon MicroHR monochromator, with a USB interface connected to the instrument computer (henceforth referred to as "MC-Hammer") for user-defined wavelength scanning. Light emitting from the output slit is nearly monochromatic, with full width at half maximum between 5 and 8 nm. A chopper wheel cuts the light into an AC signal, controlled by the chopper wheel frequency control module. Typical frequencies are between 340 and 350 Hz. The chopped light is sent through an automatic filter wheel, containing four long-pass filters at 420 nm, 680 nm, 1090 nm, and 1600 nm. These filters are controlled through the software on MC-Hammer to automatically advance as the

wavelength is scanned through their range. Long pass filters are necessary to prevent the doubles (or triples) of the wavelength the monochromator is emitting from also being passed through the slit. The chopped, filtered light is split using a second 50/50 aluminum polka dot beam splitter, with half being sent through a 1 cm cuvette holder, for absorbance of solutions, and the other half through an aperture for film measurements of absorbance, reflectance, and external quantum efficiency. Signal is acquired using silicon ("Si"), UV-sensitized silicon ("UV"), or germanium ("Ge") photodetector and a Stanford Instruments lock-in amplifier. An Agilent L4410A multiplexer is used as an electronic switch for automatic multi-channel scanning.

SECTION A2. SOFTWARE

MATLAB software is used to communicate with and control the monochromator, filter wheel, and lock-in amplifier. A custom graphical user interface (GUI), based in part on a GUI written by Prof. Michael Arnold, but heavily modified by the author, allows users to communicate with and control the entire monochromator/filter wheel/lock-in/multiplexer system. The GUI allows users to save and load scan methods, as well as automatically display derived values like absorbance, reflectance, or external QE during the scan. Automatic batch processing allows the same (or different) scans to be repeated in loops, for time-dependent measurements.

SECTION A3. MEASUREMENT METHODS

Absorbance.

Absorbance spectra of both films and solutions are taken in the same way. A reference scan, consisting of a pure solvent, or plain glass/quartz substrate, is taken. Then, without changing optics or placement of detector(s), the same scan is taken, but with the sample solution or film placed in the beam line. The absorbance, A, of a material or solution is generally displayed in terms of "natural" absorbance, using the natural logarithm to calculate A:

$$A = -\ln\left(\frac{I}{I_0}\right)$$

where I is the current registered by the detector when the sample is in place, and I_0 is the signal from the reference scan. Sometimes, absorbance is presented in optical density (OD); in this case, it is calculated using the base-10 logarithm:

$$OD = -\log_{10}\left(\frac{I}{I_0}\right)$$

Either way, the absorbance of a material is proportional to its mass density, or concentration, in the beam line, and can be used to calculate the concentration in solution, or thickness on a substrate. (See **Appendix B:** Peak fitting and concentration)

Reflectance.

Reflectance measurements require a slight change in detector orientation; in reflectance, the detector is placed at a right angle to the monochromator outlet beam path. Light striking the sample is reflected into the polka-dot beam splitter, and half of that beam is reflected into the detector. Due to the typically small spot size and partial reflection at the beam splitter, reflectance measurements tend to be noisier than absorbance. However, with careful control over the optics and detector position, information can be gained through reflectance that is not accessible using absorption alone. Reflectance spectra are taken with two reference scans. First, a mirror is placed where the sample will be, and a scan is taken. Then, the mirror is removed, and the scan is retaken; this is the "blank," and corrects for internal reflections within the system. Finally, the sample scan is taken, and the reflectance R may be calculated:

$$R = \frac{I - I_b}{I_m - I_b}$$

where I is the sample current, I_b is the "blank" current, and I_m is the mirror current. Reflectance is useful when appraising optical interference within a device stack. (See **Appendix F**: Device Modeling)

External Quantum Efficiency.

External quantum efficiency (QE) is defined as the ratio of current to photon flux. To measure external QE, it is vital to know the number of photons impinging upon the device. To do this, a calibrated photodetector

is used. Si, UV, and Ge detectors that are factory calibrated are used to measure the current from the illumination of a 1 mm diameter pinhole in the beam path. The pinhole and detector are moved around in the beam path until a maximum current is registered on the lock-in amplifier. Finding a maximum prevents accidental over-estimation of the external QE. A scan is taken over the range of calibration of the detector. The detector ranges are listed in **Table A-1**.

Table A-1. Common detectors used in monochromator measurements, along with calibration ranges.

Detector Name	Abbrev.	Min. cal. λ *(nm)*	Max. cal. λ *(nm)*
Silicon	Si	400	1100
UV-sensitized silicon	UV	280	1100
Germanium	Ge	780	1800

If the device to be scanned has a larger wavelength range than any single detector, two detectors with overlapping ranges may be used. Whatever the case, one or more reference scans are taken of the illumination through the pinhole. Using the calibration file for the detector, given as responsivity $\Re$, in units of A/W, the photon flux impinging upon the pinhole may be calculated:

$$\Phi = \frac{I_0 \lambda}{\Re h c A}$$

where Φ is the photon flux, I_0 is the detector current, λ is the wavelength, h is Planck's constant, c is the speed of light, and A is the area of the pinhole. A 1 mm diameter pinhole has an area of 0.007854 cm^2. If two detectors are used, the flux for each is calculated, and the region of spectral overlap between the two is used to normalize the flux, so that one continuous photon flux is calculated over the entire spectrum. Normalizing the flux may be accomplished by scaling the smaller flux to the larger flux, so that if any error exists, it will cause the underestimation of the external QE. Finally, the external QE of the device may be measured:

$$EQE = \frac{I}{q\Phi}$$

where q is the fundamental charge, 1.6×10^{-19} C.

APPENDIX B: PEAK FITTING AND CONCENTRATION

Accurately measuring the concentration of s-SWCNT solutions is vital to many aspects of this thesis; therefore it is important to understand the methods involved. The optical cross section of a material, σ, often reported in units of cm^2/g, is the ratio of the absorptivity and concentration:

$$\alpha = \sigma C$$

When a material's absorption peaks shift or change shape based on the environment, often an integrated optical cross section is used:

$$\int \alpha \, dE = C \int \sigma \, dE$$

Streit et al.[56] measure the integrated optical cross sections in units of cm C^{-1}, using wavenumber ν as the variable of integration. As long as the variable of integration is in units of energy, this method may be used. Absorbance spectra are converted into energy units and fit with voigt lineshapes for solutions, or gaussian lineshapes for thin films, using the freeware Fityk. Sometimes, a background may be removed prior to fitting; in this case, a "blank" film may be measured and the absorbance subtracted from the sample absorbance. In either case, each peak is assigned to a nanotube (n,m) and the relevant cross section is divided into the area of the peak to yield the concentration. For films, a density is required to calculate thickness; in our work we have used a film density of 1.2 g cm^{-3}. Dividing by the density yields the thickness:

$$t = \frac{\int \alpha \, dE}{\rho \int \sigma \, dE}.$$

APPENDIX C: PHOTOLUMINESCENCE

All photoluminescence spectra were obtained using a Horiba Nanolog Fluorimeter. When quantifying photoluminescence, especially of dense solutions, it is necessary to account for the attenuated penetration of both the excitation beam and the emission beam by the film itself. To apply the corrections, we calculate the ratio of the PL intensity that would be expected in the absence of absorption losses, PL_{corr}, to the PL intensity that is actually measured, PL_{meas}. We use measured absorption coefficients of the sample solutions at the excitation and emission wavelengths to determine this ratio. The excitation beam propagates in the *x*-direction and illuminates the sample solution with an incident intensity I_0 at the excitation wavelength. The intensity within the solution drops off according to Beer's Law,

$$I(x,y) = I_0 \exp(-A_{ex}x),$$

where A_{ex} is the measured natural absorbance of the sample solution at the excitation wavelength, and x is the distance into the solution. The excited state distribution, $D(x,y)$, will be proportional to the intensity of the light,

$$D(x,y) = I_0 c\sigma_{ex} \exp(-A_{ex}x).$$

where σ_{ex} is the absorption cross-section of the emitter at the excitation wavelength and *c* is concentration. The emitted and detected photon distribution, $\Phi(x,y)$, will be proportional to the excited state distribution, according to a factor φ_{PL}which accounts for the PL quantum yield and another factor φ_{coll}which accounts for the solid fraction of PL that is detected, according to

$$\Phi(x,y) = I_0 \varphi_{PL} \varphi_{coll} c\sigma_{ex} \exp(-A_{ex}x).$$

The emitted photons of wavelength λ_{em} will exit the solution, which has a measured natural absorbance of A_{em} at λ_{em}. The fraction emerging from depth y (collection is along the *y*-axis) will be

$$f(y) = \exp(-A_{em}y).$$

The measured intensity of PL will be the integral over the depths L_x and L_y in the directions parallel and perpendicular to the excitation beam, respectively:

$$I_{PL,meas} = I_0 \int_{y=0}^{y=L_y} \int_{x=0}^{x=L_x} I_0 \varphi_{PL} \varphi_{coll} c\sigma_{ex} \exp(-A_{ex}x) \exp(-A_{em}y)\ dy;$$

$$I_{PL,meas} = I_0 \varphi_{PL} c\sigma_{ex} \frac{1-\exp(-L_x A_{ex})}{A_{ex}} \frac{1-\exp(-L_y A_{em})}{A_{em}}.$$

Since the PL spectra are normalized by the intensity of the excitation beam, the I_0 term is already taken into account, i.e. $PL_{meas} = I_{PL,meas}/I_0$. The measured signal must be corrected by multiplying by the reciprocal of the other side, yielding an equation for the corrected photoluminescence intensity.

$$PL_{corr} = \varphi_{PL} \varphi_{coll} c\sigma_{ex} = PL_{meas} \frac{A_{ex}}{1-\exp(-L_x A_{ex})} \frac{A_{em}}{1-\exp(-L_y A_{em})}.$$

APPENDIX D: JV CHARACTERISTICS AND SOLAR SIMULATOR

SECTION D1. MEASURING JV CHARACTERISTICS

We use a Keithley 2636 sourcemeter to sweep voltage and measure current. For current-voltage characteristics, the voltage is swept from -1.5 to 1.5 V (typical; +3 for some samples) and current at each voltage is measured. The area of the device (0.007854 cm^2 for circular devices, 0.0121 cm^2 for rectangular patterned devices) is divided into the current to yield the current density, usually expressed in units of mA/cm^2. When a device is illuminated, an open circuit voltage (V_{OC}) and short-circuit current density (J_{SC}) is produced. The maximum power density (P_{out}^{max}) generated in a device is the maximum product of -*J* and *V* under forward bias. The fill factor is the ratio of the maximum power density to the product of V_{OC} and J_{SC}:

$$FF = \frac{P_{out}^{max}}{V_{OC} J_{SC}}.$$

The power conversion efficiency, η_P, is the product of fill factor, open circuit voltage, and short circuit current density, divided by the incident power, P_{in},

$$\eta_P = \frac{FF\ V_{OC}\ J_{SC}}{P_{in}}.$$

SECTION D2. SOLAR SIMULATOR

Broadband incident power that approximates the solar spectrum is vital to testing solar cell characteristics under real-world conditions. Most commercial solar simulators use xenon arc discharge lamps to generate a strong white light for solar simulation. However, xenon produces strong emission lines in the near-infrared, which interfere with and may obfuscate characterization of nanotube absorption peaks in the same region. Therefore, I developed and constructed a two-source solar simulator, using a tungsten incandescent lamp to supply infrared, and a 350-750 nm bandpass filter in front of the xenon lamp to remove unwanted near-infrared emission lines. The two light beams are combined in a 50/50 polkadot beam splitter, and focused using a Galilean telescope lens arrangement onto a sample mount.

APPENDIX E: CRYOSTAT

A Janis ST-100 Cryostat with 4 optical windows was integral to obtaining low temperature measurements. The author rewired it to include up to 10 output channels, accessible using the L4421A multiplexer. The channel positions in the 10-pin PCB internal port are labeled in **Figure E1** below.

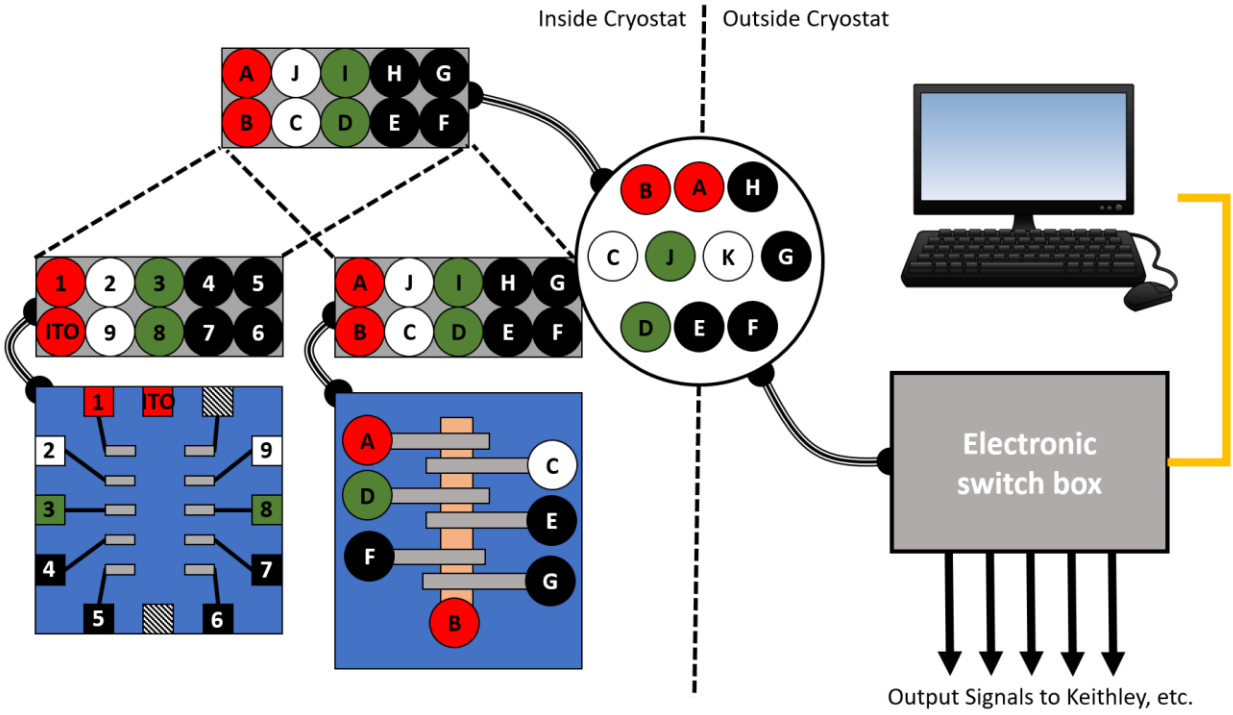

Figure E1-1. Schematic view of 10-pin PCB port, with external channel letters labeled.

APPENDIX F: MATLAB PROGRAMS

Over the last 6 years, the author has written many MATLAB programs for data analysis, instrument control, or modeling. The following list of programs will be made available through the University of Wisconsin.

Name		Version
Absorption Analysis & Fitting	Fits absorption spectra to gaussians and estimates s-SWCNT concentration	1.1
AutoPCE	Power conversion efficiency, J_{SC}, V_{OC}, and FF are generated from a JV curve in txt format.	2.1
Batch Abs and EQE fitting	Fits Absorption and EQE peaks to Gaussians and reports the amplitude and integrated area	1.0
Defect Modeling	Adds defects randomly to nanotubes of known length, resulting in length distributions used in Chapter 5.	1.0
Device Builder	Suite of 4 GUIs used to build a film, vary one or two parameters, calculate TARIQ matrix, and evaluate EQE	2.0
JV Analysis	A batch JV curve evaluation tool in the style of AutoPCE	1.0
Monte Carlo Modeling	Uses TARIQ file output from TARIQ GUI contained in Device Builder suite and known parameters of the Monte Carlo model developed in Chapter 5 to calculate IQE and EQE for a device or set of devices.	1.0
PLE Mapper	Displays a PLE map from a text file and allows inspection at various excitation/emission wavelengths	1.0
SolarSim	Takes inputs of current from calibrated detectors and outputs solar simulator spectrum	1.0
Monochromator Control Center	Control of monochromator, including Absorbance, Reflectance, EQE, and Time-resolved measurements	5.1
KE2636 Solar Control w/Multiplexer Plugin	Keithley control with multiplexer plugin to measure JV curves semi-automatically	3.0
Temperature Controller	Interfaces with temperature controller to document temperature changes	1.0
PFO Wrapping Simulator	Simulates the wrapping of PFO around carbon nanotubes of known (n,m) and outputs a file for LAMMPS input.	1.0

REFERENCES

1. Iijima, S.; Ichihashi, T., Single-Shell Carbon Nanotubes of 1-Nm Diameter. *Nature* **1993**, *363*, 603-605.
2. Yu, M. F.; Files, B. S.; Arepalli, S.; Ruoff, R. S., Tensile Loading of Ropes of Single Wall Carbon Nanotubes and Their Mechanical Properties. *Phys. Rev. Lett.* **2000**, *84*, 5552-5555.
3. Yi, J. H.; Aissa, B.; El Khakani, M. A., Ultra-High Oxidation Resistance of Suspended Single-Wall Carbon Nanotube Bundles Grown by an "All-Laser" Process. *Journal of Nanoscience and Nanotechnology* **2007**, *7*, 3394-3399.
4. Durkop, T.; Getty, S. A.; Cobas, E.; Fuhrer, M. S., Extraordinary Mobility in Semiconducting Carbon Nanotubes. *Nano Lett* **2004**, *4*, 35-39.
5. Kataura, H.; Kumazawa, Y.; Maniwa, Y.; Umezu, I.; Suzuki, S.; Ohtsuka, Y.; Achiba, Y., Optical Properties of Single-Wall Carbon Nanotubes. *Synthetic Metals* **1999**, *103*, 2555-2558.
6. Weisman, R. B.; Bachilo, S. M., Dependence of Optical Transition Energies on Structure for Single-Walled Carbon Nanotubes in Aqueous Suspension: An Empirical Kataura Plot. *Nano Lett* **2003**, *3*, 1235-1238.
7. Nish, A.; Hwang, J. Y.; Doig, J.; Nicholas, R. J., Highly Selective Dispersion of Singlewalled Carbon Nanotubes Using Aromatic Polymers. *Nature Nanotechnology* **2007**, *2*, 640-646.
8. Lebedkin, S.; Hennrich, F.; Kiowski, O.; Kappes, M. M., Photophysics of Carbon Nanotubes in Organic Polymer-Toluene Dispersions: Emission and Excitation Satellites and Relaxation Pathways. *Phys Rev B* **2008**, *77*, 8.
9. Blackburn, J. L.; Holt, J. M.; Irurzun, V. M.; Resasco, D. E.; Rumbles, G., Confirmation of K-Momentum Dark Exciton Vibronic Sidebands Using C-13-Labeled, Highly Enriched (6,5) Single-Walled Carbon Nanotubes. *Nano Lett* **2012**, *12*, 1398-1403.
10. Shea, M. J.; Mehlenbacher, R. D.; Zanni, M. T.; Arnold, M. S., Experimental Measurement of the Binding Configuration and Coverage of Chirality-Sorting Polyfluorenes on Carbon Nanotubes. *Journal of Physical Chemistry Letters* **2014**, *5*, 3742-3749.
11. Brady, G. J.; Joo, Y.; Wu, M. Y.; Shea, M. J.; Gopalan, P.; Arnold, M. S., Polyfluorene-Sorted, Carbon Nanotube Array Field-Effect Transistors with Increased Current Density and High on/Off Ratio. *ACS Nano* **2014**, *8*, 11614-11621.
12. O'Connell, M. J.; Bachilo, S. M.; Huffman, C. B.; Moore, V. C.; Strano, M. S.; Haroz, E. H.; Rialon, K. L.; Boul, P. J.; Noon, W. H.; Kittrell, C., et al., Band Gap Fluorescence from Individual Single-Walled Carbon Nanotubes. *Science* **2002**, *297*, 593-596.
13. Lebedkin, S.; Hennrich, F.; Skipa, T.; Kappes, M. M., Near-Infrared Photoluminescence of Single-Walled Carbon Nanotubes Prepared by the Laser Vaporization Method. *Journal of Physical Chemistry B* **2003**, *107*, 1949-1956.
14. Shea, M. J.; Arnold, M. S., 1% Solar Cells Derived from Ultrathin Carbon Nanotube Photoabsorbing Films. *Appl Phys Lett* **2013**, *102*, 5.
15. Bindl, D. J.; Safron, N. S.; Arnold, M. S., Dissociating Excitons Photogenerated in Semiconducting Carbon Nanotubes at Polymeric Photovoltaic Heterojunction Interfaces. *ACS Nano* **2010**, *4*, 5657-5664.
16. Shulaker, M. M.; Hills, G.; Patil, N.; Wei, H.; Chen, H. Y.; PhilipWong, H. S.; Mitra, S., Carbon Nanotube Computer. *Nature* **2013**, *501*, 526-+.
17. Wu, M.-Y.; Jacobberger, R. M.; Arnold, M. S., Design Length Scales for Carbon Nanotube Photoabsorber Based Photovoltaic Materials and Devices. *Journal of Applied Physics* **2013**, *113*, 204504.
18. Bahr, J. L.; Tour, J. M., Highly Functionalized Carbon Nanotubes Using in Situ Generated Diazonium Compounds. *Chemistry of Materials* **2001**, *13*, 3823-3824.

19. Bahr, J. L.; Tour, J. M., Covalent Chemistry of Single-Wall Carbon Nanotubes. *J. Mater. Chem.* **2002**, *12*, 1952-1958.
20. Wang, J. L.; Shea, M. J.; Flach, J. T.; McDonough, T. J.; Way, A. J.; Zanni, M. T.; Arnold, M. S., Role of Defects as Exciton Quenching Sites in Carbon Nanotube Photovoltaics. *J Phys Chem C* **2017**, *121*, 8310-8318.
21. Harrah, D. M.; Swan, A. K., The Role of Length and Defects on Optical Quantum Efficiency and Exciton Decay Dynamics in Single-Walled Carbon Nanotubes. *ACS Nano* **2011**, *5*, 647-655.
22. Rouhi, N.; Jain, D.; Zand, K.; Burke, P. J., Fundamental Limits on the Mobility of Nanotube-Based Semiconducting Inks. *Adv. Mater.* **2011**, *23*, 94-+.
23. Chen, F. M.; Ye, J.; Teo, M. Y.; Zhao, Y.; Tan, L. P.; Chen, Y.; Chan-Park, M. B.; Li, L. J., Species-Dependent Energy Transfer of Surfactant-Dispersed Semiconducting Single-Walled Carbon Nanotubes. *J Phys Chem C* **2009**, *113*, 20061-20065.
24. Zheng, M.; Jagota, A.; Semke, E. D.; Diner, B. A.; McLean, R. S.; Lustig, S. R.; Richardson, R. E.; Tassi, N. G., DNA-Assisted Dispersion and Separation of Carbon Nanotubes. *Nature Materials* **2003**, *2*, 338-342.
25. Giulianini, M.; Waclawik, E. R.; Bell, J. M.; De Crescenzi, M.; Castrucci, P.; Scarselli, M.; Motta, N., Regioregular Poly(3-Hexyl-Thiophene) Helical Self-Organization on Carbon Nanotubes. *Appl Phys Lett* **2009**, *95*, 3.
26. Arnold, M. S.; Stupp, S. I.; Hersam, M. C., Enrichment of Single-Walled Carbon Nanotubes by Diameter in Density Gradients. *Nano Lett* **2005**, *5*, 713-718.
27. Arnold, K.; Hennrich, F.; Krupke, R.; Lebedkin, S.; Kappes, M. M., Length Separation Studies of Single Walled Carbon Nanotube Dispersions. *Physica Status Solidi B-Basic Solid State Physics* **2006**, *243*, 3073-3076.
28. Arnold, M. S.; Green, A. A.; Hulvat, J. F.; Stupp, S. I.; Hersam, M. C., Sorting Carbon Nanotubes by Electronic Structure Using Density Differentiation. *Nat Nanotechnol* **2006**, *1*, 60-65.
29. Mistry, K. S.; Larsen, B. A.; Blackburn, J. L., High-Yield Dispersions of Large-Diameter Semiconducting Single-Walled Carbon Nanotubes with Tunable Narrow Chirality Distributions. *Acs Nano* **2013**, *7*, 2231-2239.
30. Ozawa, H.; Ide, N.; Fujigaya, T.; Niidome, Y.; Nakashima, N., One-Pot Separation of Highly Enriched (6,5)-Single-Walled Carbon Nanotubes Using a Fluorene-Based Copolymer. *Chemistry Letters* **2011**, *40*, 239-241.
31. Bolinger, M.; Seel, J.; LaCommare, K. H. *Utility-Scale Solar 2016: An Empirical Analysis of Project Cost, Performance, and Pricing Trends in the United States*; Lawrence Berkeley National Lab.(LBNL), Berkeley, CA (United States): 2017.
32. Bachilo, S. M.; Strano, M. S.; Kittrell, C.; Hauge, R. H.; Smalley, R. E.; Weisman, R. B., Structure-Assigned Optical Spectra of Single-Walled Carbon Nanotubes. *Science* **2002**, *298*, 2361-2366.
33. Maultzsch, J.; Pomraenke, R.; Reich, S.; Chang, E.; Prezzi, D.; Ruini, A.; Molinari, E.; Strano, M. S.; Thomsen, C.; Lienau, C., Exciton Binding Energies in Carbon Nanotubes from Two-Photon Photoluminescence. *Phys Rev B* **2005**, *72*, 4.
34. Bindl, D. J.; Arnold, M. S., Efficient Exciton Relaxation and Charge Generation in Nearly Monochiral (7,5) Carbon Nanotube/C60 Thin-Film Photovoltaics. *The Journal of Physical Chemistry C* **2013**, *117*, 2390-2395.
35. Wildoer, J. W. G.; Venema, L. C.; Rinzler, A. G.; Smalley, R. E.; Dekker, C., Electronic Structure of Atomically Resolved Carbon Nanotubes. *Nature* **1998**, *391*, 59-62.
36. Avouris, P., Carbon Nanotube Electronics. *Chemical Physics* **2002**, *281*, 429-445.
37. Liu, J.; Hersam, M. C., Recent Developments in Carbon Nanotube Sorting and Selective Growth. *Mrs Bulletin* **2010**, *35*, 315-321.
38. Zhang, H. L.; Wu, B.; Hu, W. P.; Liu, Y. Q., Separation and/or Selective Enrichment of Single-Walled Carbon Nanotubes Based on Their Electronic Properties. *Chemical Society Reviews* **2011**, *40*, 1324-1336.

39. Hwang, J. Y.; Nish, A.; Doig, J.; Douven, S.; Chen, C. W.; Chen, L. C.; Nicholas, R. J., Polymer Structure and Solvent Effects on the Selective Dispersion of Single-Walled Carbon Nanotubes. *Journal of the American Chemical Society* **2008**, *130*, 3543-3553.
40. Gomulya, W.; Costanzo, G. D.; de Carvalho, E. J. F.; Bisri, S. Z.; Derenskyi, V.; Fritsch, M.; Frohlich, N.; Allard, S.; Gordiichuk, P.; Herrmann, A., et al., Semiconducting Single-Walled Carbon Nanotubes on Demand by Polymer Wrapping. *Adv. Mater.* **2013**, *25*, 2948-2956.
41. Brady, G. J.; Yongho, J.; Roy, S. S.; Gopalan, P.; Arnold, M. S., High Performance Transistors Via Aligned Polyfluorene-Sorted Carbon Nanotubes. *Appl Phys Lett* **2014**, *104*, 083107 (083105 pp.)-083107 (083105 pp.).
42. Jakubka, F.; Backes, C.; Gannott, F.; Mundloch, U.; Hauke, F.; Hirsch, A.; Zaumseil, J., Mapping Charge Transport by Electroluminescence in Chirality-Selected Carbon Nanotube Networks. *ACS Nano* **2013**, *7*, 7428-7435.
43. Bisri, S. Z.; Gao, J.; Derenskyi, V.; Gomulya, W.; Iezhokin, I.; Gordiichuk, P.; Herrmann, A.; Loi, M. A., High Performance Ambipolar Field-Effect Transistor of Random Network Carbon Nanotubes. *Adv. Mater.* **2012**, *24*, 6147-6152.
44. Xu, F.; Wu, M. Y.; Safron, N. S.; Roy, S. S.; Jacobberger, R. M.; Bindl, D. J.; Seo, J. H.; Chang, T. H.; Ma, Z. Q.; Arnold, M. S., Highly Stretchable Carbon Nanotube Transistors with Ion Gel Gate Dielectrics. *Nano Lett* **2014**, *14*, 682-686.
45. Xu, W. Y.; Zhao, J. W.; Qian, L.; Han, X. Y.; Wu, L. Z.; Wu, W. C.; Song, M. S.; Zhou, L.; Su, W. M.; Wang, C., et al., Sorting of Large-Diameter Semiconducting Carbon Nanotube and Printed Flexible Driving Circuit for Organic Light Emitting Diode (Oled). *Nanoscale* **2014**, *6*, 1589-1595.
46. Wang, H. L.; Mei, J. G.; Liu, P.; Schmidt, K.; Jimenez-Oses, G.; Osuna, S.; Fang, L.; Tassone, C. J.; Zoombelt, A. P.; Sokolov, A. N., et al., Scalable and Selective Dispersion of Semiconducting Arc-Discharged Carbon Nanotubes by Dithiafulvalene/Thiophene Copolymers for Thin Film Transistors. *ACS Nano* **2013**, *7*, 2659-2668.
47. Lu, R. T.; Christianson, C.; Kirkeminde, A.; Ren, S. Q.; Wu, J. D., Extraordinary Photocurrent Harvesting at Type-Ii Heterojunction Interfaces: Toward High Detectivity Carbon Nanotube Infrared Detectors. *Nano Lett* **2012**, *12*, 6244-6249.
48. Kazaoui, S.; Minami, N.; Nalini, B.; Kim, Y.; Hara, K., Near-Infrared Photoconductive and Photovoltaic Devices Using Single-Wall Carbon Nanotubes in Conductive Polymer Films. *Journal of Applied Physics* **2005**, *98*, 6.
49. Ramuz, M. P.; Vosgueritchian, M.; Wei, P.; Wang, C.; Gao, Y.; Wu, Y.; Chen, Y.; Bao, Z., Evaluation of Solution-Processable Carbon-Based Electrodes for All-Carbon Solar Cells. *ACS Nano* **2012**, *6*, 10384-10395.
50. Wang, H.; Koleilat, G. I.; Liu, P.; Jimenez-Oses, G.; Lai, Y.-C.; Vosgueritchian, M.; Fang, Y.; Park, S.; Houk, K. N.; Bao, Z., High-Yield Sorting of Small-Diameter Carbon Nanotubes for Solar Cells and Transistors. *ACS Nano* **2014**, *8*, 2609-2617.
51. Svrcek, V.; Cook, S.; Kazaoui, S.; Kondo, M., Silicon Nanocrystals and Semiconducting Single-Walled Carbon Nanotubes Applied to Photovoltaic Cells. *Journal of Physical Chemistry Letters* **2011**, *2*, 1646-1650.
52. Gao, J.; Loi, M. A.; de Carvalho, E. J. F.; dos Santos, M. C., Selective Wrapping and Supramolecular Structures of Polyfluorene-Carbon Nanotube Hybrids. *ACS Nano* **2011**, *5*, 3993-3999.
53. Lee, H. W.; Yoon, Y.; Park, S.; Oh, J. H.; Hong, S.; Liyanage, L. S.; Wang, H. L.; Morishita, S.; Patil, N.; Park, Y. J., et al., Selective Dispersion of High Purity Semiconducting Single-Walled Carbon Nanotubes with Regioregular Poly(3-Alkylthiophene)S. *Nature Communications* **2011**, *2*, 8.
54. Lemasson, F. A.; Strunk, T.; Gerstel, P.; Hennrich, F.; Lebedkin, S.; Barner-Kowollik, C.; Wenzel, W.; Kappes, M. M.; Mayor, M., Selective Dispersion of Single-Walled Carbon Nanotubes with Specific Chiral Indices by Poly(N-Decyl-2,7-Carbazole). *Journal of the American Chemical Society* **2011**, *133*, 652-655.

55. Chen, Y. S.; Xu, Y. Q.; Wang, Q. M.; Gunasinghe, R. N.; Wang, X. Q.; Pang, Y., Highly Selective Dispersion of Carbon Nanotubes by Using Poly(Phenyleneethynylene)-Guided Supermolecular Assembly. *Small* **2013**, *9*, 870-875.
56. Streit, J. K.; Bachilo, S. M.; Ghosh, S.; Lin, C.-W.; Weisman, R. B., Directly Measured Optical Absorption Cross Sections for Structure-Selected Single-Walled Carbon Nanotubes. *Nano Lett* **2014**.
57. Green, A. A.; Hersam, M. C., Nearly Single-Chirality Single-Walled Carbon Nanotubes Produced Via Orthogonal Iterative Density Gradient Ultracentrifugation. *Adv. Mater.* **2011**, *23*, 2185-+.
58. Nish, A.; Hwang, J. Y.; Doig, J.; Nicholas, R. J., Direct Spectroscopic Evidence of Energy Transfer from Photo-Excited Semiconducting Polymers to Single-Walled Carbon Nanotubes. *Nanotechnology* **2008**, *19*, 6.
59. Naumov, A. V.; Ghosh, S.; Tsyboulski, D. A.; Bachilo, S. M.; Weisman, R. B., Analyzing Absorption Backgrounds in Single-Walled Carbon Nanotube Spectra. *ACS Nano* **2011**, *5*, 1639-1648.
60. Haroz, E. H.; Bachilo, S. M.; Weisman, R. B.; Doorn, S. K., Curvature Effects on the E-33 and E-44 Exciton Transitions in Semiconducting Single-Walled Carbon Nanotubes. *Phys Rev B* **2008**, *77*, 9.
61. Liu, K. H.; Hong, X. P.; Choi, S.; Jin, C. H.; Capaz, R. B.; Kim, J.; Wang, W. L.; Bai, X. D.; Louie, S. G.; Wang, E. G., et al., Systematic Determination of Absolute Absorption Cross-Section of Individual Carbon Nanotubes. *Proceedings of the National Academy of Sciences of the United States of America* **2014**, *111*, 7564-7569.
62. Garrot, D.; Langlois, B.; Roquelet, C.; Michel, T.; Roussignol, P.; Delalande, C.; Deleporte, E.; Lauret, J. S.; Voisin, C., Time-Resolved Investigation of Excitation Energy Transfer in Carbon Nanotube-Porphyrin Compounds. *J Phys Chem C* **2011**, *115*, 23283-23292.
63. Roquelet, C.; Garrot, D.; Lauret, J. S.; Voisin, C.; Alain-Rizzo, V.; Roussignol, P.; Delaire, J. A.; Deleporte, E., Quantum Efficiency of Energy Transfer in Noncovalent Carbon Nanotube/Porphyrin Compounds. *Appl Phys Lett* **2010**, *97*, 3.
64. Tamai, Y.; Ohkita, H.; Benten, H.; Ito, S., Singlet Fission in Poly(9,9 '-Di-N-Octylfluorene) Films. *J Phys Chem C* **2013**, *117*, 10277-10284.
65. Hill, A. V., Proceedings of the Physiological Society: January 22, 1910. *The Journal of Physiology* **1910**, *40*, i-vii.
66. Gather, M. C.; Bradley, D. D. C., An Improved Optical Method for Determining the Order Parameter in Thin Oriented Molecular Films and Demonstration of a Highly Axial Dipole Moment for the Lowest Energy Pi-Pi Optical Transition in Poly(9,9-Dioctylfluorene-Co-Bithiophene). *Advanced Functional Materials* **2007**, *17*, 479-485.
67. Liem, H. M.; Etchegoin, P.; Whitehead, K. S.; Bradley, D. D. C., Raman Anisotropy Measurements: An Effective Probe of Molecular Orientation in Conjugated Polymer Thin Films. *Advanced Functional Materials* **2003**, *13*, 66-72.
68. Deria, P.; Von Bargen, C. D.; Olivier, J. H.; Kumbhar, A. S.; Saven, J. G.; Therien, M. J., Single-Handed Helical Wrapping of Single-Walled Carbon Nanotubes by Chiral, Ionic, Semiconducting Polymers. *Journal of the American Chemical Society* **2013**, *135*, 16220-16234.
69. Gerstel, P.; Klumpp, S.; Hennrich, F.; Poschlad, A.; Meded, V.; Blasco, E.; Wenzel, W.; Kappes, M. M.; Barner-Kowollik, C., Highly Selective Dispersion of Single-Walled Carbon Nanotubes Via Polymer Wrapping: A Combinatorial Study Via Modular Conjugation. *Acs Macro Lett* **2014**, *3*, 10-15.
70. Stevens, M. A.; Silva, C.; Russell, D. M.; Friend, R. H., Exciton Dissociation Mechanisms in the Polymeric Semiconductors Poly(9,9-Dioctylfluorene) and Poly(9, 9-Dioctylfluorene-Co-Benzothiadiazole). *Phys Rev B* **2001**, *63*, 18.
71. Schoppler, F.; Mann, C.; Hain, T. C.; Neubauer, F. M.; Privitera, G.; Bonaccorso, F.; Chu, D. P.; Ferrari, A. C.; Hertel, T., Molar Extinction Coefficient of Single-Wall Carbon Nanotubes. *J Phys Chem C* **2011**, *115*, 14682-14686.

72. Rowell, M. W.; Topinka, M. A.; McGehee, M. D.; Prall, H. J.; Dennler, G.; Sariciftci, N. S.; Hu, L. B.; Gruner, G., Organic Solar Cells with Carbon Nanotube Network Electrodes. *Appl Phys Lett* **2006**, *88*.
73. Pasquier, A. D.; Unalan, H. E.; Kanwal, A.; Miller, S.; Chhowalla, M., Conducting and Transparent Single-Wall Carbon Nanotube Electrodes for Polymer-Fullerene Solar Cells. *Appl Phys Lett* **2005**, *87*, 3.
74. Pavasupree, S.; Suzuki, Y.; Kitiyanan, A.; Pivsa-Art, S.; Yoshikawa, S., Synthesis and Characterization of Vanadium Oxides Nanorods. *J. Solid State Chem.* **2005**, *178*, 2152-2158.
75. Brown, P.; Takechi, K.; Kamat, P. V., Single-Walled Carbon Nanotube Scaffolds for Dye-Sensitized Solar Cells. *J Phys Chem C* **2008**, *112*, 4776-4782.
76. Li, Z. R.; Kunets, V. P.; Saini, V.; Xu, Y.; Dervishi, E.; Salamo, G. J.; Biris, A. R.; Biris, A. S., Light-Harvesting Using High Density P-Type Single Wall Carbon Nanotube/N-Type Silicon Heterojunctions. *Acs Nano* **2009**, *3*, 1407-1414.
77. Ulbricht, R.; Lee, S. B.; Jiang, X. M.; Inoue, K.; Zhang, M.; Fang, S. L.; Baughman, R. H.; Zakhidov, A. A., Transparent Carbon Nanotube Sheets as 3-D Charge Collectors in Organic Solar Cells. *Sol. Energy Mater. Sol. Cells* **2007**, *91*, 416-419.
78. Jia, Y.; Wei, J. Q.; Wang, K. L.; Cao, A. Y.; Shu, Q. K.; Gui, X. C.; Zhu, Y. Q.; Zhuang, D. M.; Zhang, G.; Ma, B. B., et al., Nanotube-Silicon Heterojunction Solar Cells. *Adv. Mater.* **2008**, *20*, 4594-4598.
79. Kongkanand, A.; Dominguez, R. M.; Kamat, P. V., Single Wall Carbon Nanotube Scaffolds for Photoelectrochemical Solar Cells. Capture and Transport of Photogenerated Electrons. *Nano Lett* **2007**, *7*, 676-680.
80. Bindl, D. J.; Wu, M. Y.; Prehn, F. C.; Arnold, M. S., Efficiently Harvesting Excitons from Electronic Type-Controlled Semiconducting Carbon Nanotube Films. *Nano Lett* **2011**, *11*, 455-460.
81. Jain, R. M.; Howden, R.; Tvrdy, K.; Shimizu, S.; Hilmer, A. J.; McNicholas, T. P.; Gleason, K. K.; Strano, M. S., Polymer-Free near-Infrared Photovoltaics with Single Chirality (6,5) Semiconducting Carbon Nanotube Active Layers. *Adv. Mater.* **2012**, *24*, 4436-4439.
82. Ren, S. Q.; Bernardi, M.; Lunt, R. R.; Bulovic, V.; Grossman, J. C.; Gradecak, S., Toward Efficient Carbon Nanotube/P3ht Solar Cells: Active Layer Morphology, Electrical, and Optical Properties. *Nano Lett* **2011**, *11*, 5316-5321.
83. Arnold, M. S.; Zimmerman, J. D.; Renshaw, C. K.; Xu, X.; Lunt, R. R.; Austin, C. M.; Forrest, S. R., Broad Spectral Response Using Carbon Nanotube/Organic Semiconductor/C-60 Photodetectors. *Nano Lett* **2009**, *9*, 3354-3358.
84. Bindl, D. J.; Shea, M. J.; Arnold, M. S., Enhancing Extraction of Photogenerated Excitons from Semiconducting Carbon Nanotube Films as Photocurrent. *Chemical Physics* **2013**, *413*, 29-34.
85. Ando, T., Environment Effects on Excitons in Semiconducting Carbon Nanotubes. *Journal of the Physical Society of Japan* **2010**, *79*.
86. Peumans, P.; Yakimov, A.; Forrest, S. R., Small Molecular Weight Organic Thin-Film Photodetectors and Solar Cells. *Journal of Applied Physics* **2003**, *93*, 3693-3723.
87. Osterwald, C. R., Translation of Device Performance-Measurements to Reference Conditions. *Solar Cells* **1986**, *18*, 269-279.
88. Lefebvre, J.; Finnie, P.; Homma, Y., Temperature-Dependent Photoluminescence from Single-Walled Carbon Nanotubes. *Phys Rev B* **2004**, *70*, 8.
89. Htoon, H.; O'Connell, M. J.; Cox, P. J.; Doorn, S. K.; Klimov, V. I., Low Temperature Emission Spectra of Individual Single-Walled Carbon Nanotubes: Multiplicity of Subspecies within Single-Species Nanotube Ensembles. *Phys. Rev. Lett.* **2004**, *93*, 027401.
90. Mortimer, I. B.; Nicholas, R. J., Role of Bright and Dark Excitons in the Temperature-Dependent Photoluminescence of Carbon Nanotubes. *Phys. Rev. Lett.* **2007**, *98*, 027404.
91. Bisri, S. Z.; Derenskyi, V.; Gomulya, W.; Salazar-Rios, J. M.; Fritsch, M.; Frohlich, N.; Jung, S.; Allard, S.; Scherf, U.; Loi, M. A., Anomalous Carrier Transport in Ambipolar Field-Effect

Transistor of Large Diameter Single-Walled Carbon Nanotube Network. *Adv Electron Mater* **2016**, *2*, 7.

92. Ihly, R.; Mistry, K. S.; Ferguson, A. J.; Clikeman, T. T.; Larson, B. W.; Reid, O.; Boltalina, O. V.; Strauss, S. H.; Rumbles, G.; Blackburn, J. L., Tuning the Driving Force for Exciton Dissociation in Single-Walled Carbon Nanotube Heterojunctions. *Nature Chemistry* **2016**, *8*, 603-609.
93. Jeong, W. I.; Lee, Y. E.; Shim, H. S.; Kim, T. M.; Kim, S. Y.; Kim, J. J., Photoconductivity of C60 as an Origin of Bias-Dependent Photocurrent in Organic Photovoltaics. *Advanced Functional Materials* **2012**, *22*, 3089-3094.
94. Giebink, N. C.; Wiederrecht, G. P.; Wasielewski, M. R.; Forrest, S. R., Ideal Diode Equation for Organic Heterojunctions. I. Derivation and Application. *Phys Rev B* **2010**, *82*, 12.
95. Rand, B. P.; Burk, D. P.; Forrest, S. R., Offset Energies at Organic Semiconductor Heterojunctions and Their Influence on the Open-Circuit Voltage of Thin-Film Solar Cells. *Phys Rev B* **2007**, *75*, 11.
96. Yoo, S.; Domercq, B.; Kippelen, B., Intensity-Dependent Equivalent Circuit Parameters of Organic Solar Cells Based on Pentacene and C-60. *Journal of Applied Physics* **2005**, *97*, 9.
97. Riedel, I.; Parisi, J.; Dyakonov, V.; Lutsen, L.; Vanderzande, D.; Hummelen, J. C., Effect of Temperature and Illumination on the Electrical Characteristics of Polymer-Fullerene Bulk-Heterojunction Solar Cells. *Advanced Functional Materials* **2004**, *14*, 38-44.
98. Kao, K. C.; Hwang, W., *Electrical Transport in Solids: With Particular Reference to Organic Semiconductors*; Pergamon Press, 1981.
99. Scott, J. C., Metal-Organic Interface and Charge Injection in Organic Electronic Devices. *J. Vac. Sci. Technol. A* **2003**, *21*, 521-531.
100. Wolf, U.; Arkhipov, V. I.; Bassler, H., Current Injection from a Metal to a Disordered Hopping System. I. Monte Carlo Simulation. *Phys Rev B* **1999**, *59*, 7507-7513.
101. Cheyns, D.; Poortmans, J.; Heremans, P.; Deibel, C.; Verlaak, S.; Rand, B. P.; Genoe, J., Analytical Model for the Open-Circuit Voltage and Its Associated Resistance in Organic Planar Heterojunction Solar Cells. *Phys Rev B* **2008**, *77*, 10.
102. Gao, F.; Tress, W.; Wang, J.; Inganas, O., Temperature Dependence of Charge Carrier Generation in Organic Photovoltaics. *Phys. Rev. Lett.* **2015**, *114*, 128701.
103. Cowan, S. R.; Roy, A.; Heeger, A. J., Recombination in Polymer-Fullerene Bulk Heterojunction Solar Cells. *Phys Rev B* **2010**, *82*, 10.
104. Ye, Y.; Bindl, D. J.; Jacobberger, R. M.; Wu, M. Y.; Roy, S. S.; Arnold, M. S., Semiconducting Carbon Nanotube Aerogel Bulk Heterojunction Solar Cells. *Small* **2014**, *10*, 3299-3306.
105. Dowgiallo, A.-M.; Mistry, K. S.; Johnson, J. C.; Blackburn, J. L., Ultrafast Spectroscopic Signature of Charge Transfer between Single-Walled Carbon Nanotubes and C60. *ACS Nano* **2014**, *8*, 8573-8581.
106. Dowgiallo, A.-M.; Mistry, K. S.; Johnson, J. C.; Reid, O. G.; Blackburn, J. L., Probing Exciton Diffusion and Dissociation in Single-Walled Carbon Nanotube–C60 Heterojunctions. *The Journal of Physical Chemistry Letters* **2016**, *7*, 1794-1799.
107. Ferguson, A. J.; Dowgiallo, A.-M.; Bindl, D. J.; Mistry, K. S.; Reid, O. G.; Kopidakis, N.; Arnold, M. S.; Blackburn, J. L., Trap-Limited Carrier Recombination in Single-Walled Carbon Nanotube Heterojunctions with Fullerene Acceptor Layers. *Phys Rev B* **2015**, *91*, 245311.
108. Wang, F.; Dukovic, G.; Brus, L. E.; Heinz, T. F., The Optical Resonances in Carbon Nanotubes Arise from Excitons. *Science* **2005**, *308*, 838.
109. Ma, Y.-Z.; Valkunas, L.; Bachilo, S. M.; Fleming, G. R., Exciton Binding Energy in Semiconducting Single-Walled Carbon Nanotubes. *The Journal of Physical Chemistry B* **2005**, *109*, 15671-15674.
110. Bindl, D. J.; Brewer, A. S.; Arnold, M. S., Semiconducting Carbon Nanotube/Fullerene Blended Heterojunctions for Photovoltaic near-Infrared Photon Harvesting. *Nano Res* **2011**, *4*, 1174-1179.

111. Avery, A. D.; Zhou, B. H.; Lee, J.; Lee, E.-S.; Miller, E. M.; Ihly, R.; Wesenberg, D.; Mistry, K. S.; Guillot, S. L.; Zink, B. L., et al., Tailored Semiconducting Carbon Nanotube Networks with Enhanced Thermoelectric Properties. *Nature Energy* **2016**, *1*, 16033.
112. Siitonen, A. J.; Tsyboulski, D. A.; Bachilo, S. M.; Weisman, R. B., Surfactant-Dependent Exciton Mobility in Single-Walled Carbon Nanotubes Studied by Single-Molecule Reactions. *Nano Lett* **2010**, *10*, 1595-1599.
113. Hertel, T.; Himmelein, S.; Ackermann, T.; Stich, D.; Crochet, J., Diffusion Limited Photoluminescence Quantum Yields in 1-D Semiconductors: Single-Wall Carbon Nanotubes. *ACS Nano* **2010**, *4*, 7161-7168.
114. Crochet, J. J.; Duque, J. G.; Werner, J. H.; Lounis, B.; Cognet, L.; Doorn, S. K., Disorder Limited Exciton Transport in Colloidal Single-Wall Carbon Nanotubes. *Nano Lett* **2012**, *12*, 5091-5096.
115. Liu, Z. Y.; Gao, X. D.; Zhu, Z. W.; Qiu, Z. J.; Wu, D. P.; Zhang, Z. B.; Zhang, S. L., Solution-Processed Logic Gates Based on Nanotube/Polymer Composite. *Ieee Transactions on Electron Devices* **2013**, *60*, 2542-2547.
116. Grechko, M.; Ye, Y.; Mehlenbacher, R. D.; McDonough, T. J.; Wu, M. Y.; Jacobberger, R. M.; Arnold, M. S.; Zanni, M. T., Diffusion-Assisted Photoexcitation Transfer in Coupled Semiconducting Carbon Nanotube Thin Films. *ACS Nano* **2014**, *8*, 5383-5394.
117. Mehlenbacher, R. D.; McDonough, T. J.; Grechko, M.; Wu, M. Y.; Arnold, M. S.; Zanni, M. T., Energy Transfer Pathways in Semiconducting Carbon Nanotubes Revealed Using Two-Dimensional White-Light Spectroscopy. *Nat Commun* **2015**, *6*, 6732.
118. Mehlenbacher, R. D.; Wang, J. L.; Kearns, N. M.; Shea, M. J.; Flach, J. T.; McDonough, T. J.; Wu, M. Y.; Arnold, M. S.; Zanni, M. T., Ultrafast Exciton Hopping Observed in Bare Semiconducting Carbon Nanotube Thin Films with Two-Dimensional White-Light Spectroscopy. *Journal of Physical Chemistry Letters* **2016**, *7*, 2024-2031.
119. Cognet, L.; Tsyboulski, D. A.; Rocha, J.-D. R.; Doyle, C. D.; Tour, J. M.; Weisman, R. B., Stepwise Quenching of Exciton Fluorescence in Carbon Nanotubes by Single-Molecule Reactions. *Science* **2007**, *316*, 1465.
120. Piao, Y. M.; Meany, B.; Powell, L. R.; Valley, N.; Kwon, H.; Schatz, G. C.; Wang, Y. H., Brightening of Carbon Nanotube Photoluminescence through the Incorporation of Sp(3) Defects. *Nature Chemistry* **2013**, *5*, 840-845.
121. Hartmann, N. F.; Velizhanin, K. A.; Haroz, E. H.; Kim, M.; Ma, X.; Wang, Y.; Htoon, H.; Doorn, S. K., Photoluminescence Dynamics of Aryl Sp(3) Defect States in Single-Walled Carbon Nanotubes. *ACS Nano* **2016**, *10*, 8355-8365.
122. Rajan, A.; Strano, M. S.; Heller, D. A.; Hertel, T.; Schulten, K., Length-Dependent Optical Effects in Single Walled Carbon Nanotubes. *Journal of Physical Chemistry B* **2008**, *112*, 6211-6213.
123. Miyauchi, Y.; Matsuda, K.; Yamamoto, Y.; Nakashima, N.; Kanemitsu, Y., Length-Dependent Photoluminescence Lifetimes in Single-Walled Carbon Nanotubes. *J Phys Chem C* **2010**, *114*, 12905-12908.
124. Knight, D. S.; White, W. B., Characterization of Diamond Films by Raman-Spectroscopy. *J Mater Res* **1989**, *4*, 385-393.
125. Dresselhaus, M. S.; Jorio, A.; Souza, A. G.; Saito, R., Defect Characterization in Graphene and Carbon Nanotubes Using Raman Spectroscopy. *Philos T R Soc A* **2010**, *368*, 5355-5377.
126. Nish, A.; Hwang, J.-Y.; Doig, J.; Nicholas, R. J., Highly Selective Dispersion of Single-Walled Carbon Nanotubes Using Aromatic Polymers. *Nat Nano* **2007**, *2*, 640-646.
127. Guillot, S. L.; Mistry, K. S.; Avery, A. D.; Richard, J.; Dowgiallo, A. M.; Ndione, P. F.; van de Lagemaat, J.; Reese, M. O.; Blackburn, J. L., Precision Printing and Optical Modeling of Ultrathin Swcnt/C-60 Heterojunction Solar Cells. *Nanoscale* **2015**, *7*, 6556-6566.
128. Fagan, J. A.; Simpson, J. R.; Bauer, B. J.; Lacerda, S. H. D.; Becker, M. L.; Chun, J.; Migler, K. B.; Walker, A. R. H.; Hobbie, E. K., Length-Dependent Optical Effects in Single-Wall Carbon Nanotubes. *Journal of the American Chemical Society* **2007**, *129*, 10607-10612.

129. Koyama, T.; Asaka, K.; Hikosaka, N.; Kishida, H.; Saito, Y.; Nakamura, A., Ultrafast Exciton Energy Transfer in Bundles of Single-Walled Carbon Nanotubes. *Journal of Physical Chemistry Letters* **2011**, *2*, 127-132.
130. Qian, H. H.; Georgi, C.; Anderson, N.; Green, A. A.; Hersam, M. C.; Novotny, L.; Hartschuh, A., Exciton Energy Transfer in Pairs of Single-Walled Carbon Nanotubes. *Nano Lett* **2008**, *8*, 1363-1367.
131. Mehlenbacher, R. D.; Wu, M. Y.; Grechko, M.; Laaser, J. E.; Arnold, M. S.; Zanni, M. T., Photoexcitation Dynamics of Coupled Semiconducting Carbon Nanotube Thin Films. *Nano Lett* **2013**, *13*, 1495-1501.
132. Graf, A.; Zakharko, Y.; Schiessl, S. P.; Backes, C.; Pfohl, M.; Flavel, B. S.; Zaumseil, J., Large Scale, Selective Dispersion of Long Single-Walled Carbon Nanotubes with High Photoluminescence Quantum Yield by Shear Force Mixing. *Carbon* **2016**, *105*, 593-599.
133. Dresselhaus, M. S.; Dresselhaus, G.; Saito, R.; Jorio, A., Raman Spectroscopy of Carbon Nanotubes. *Physics Reports* **2005**, *409*, 47-99.
134. Cancado, L. G.; Takai, K.; Enoki, T.; Endo, M.; Kim, Y. A.; Mizusaki, H.; Jorio, A.; Coelho, L. N.; Magalhaes-Paniago, R.; Pimenta, M. A., General Equation for the Determination of the Crystallite Size L-a of Nanographite by Raman Spectroscopy. *Appl Phys Lett* **2006**, *88*, 163106.
135. Vichchulada, P.; Cauble, M. A.; Abdi, E. A.; Obi, E. I.; Zhang, Q. H.; Lay, M. D., Sonication Power for Length Control of Single-Walled Carbon Nanotubes in Aqueous Suspensions Used for 2-Dimensional Network Formation. *J Phys Chem C* **2010**, *114*, 12490-12495.
136. Sanchez, S. R.; Bachilo, S. M.; Kadria-Vili, Y.; Lin, C. W.; Weisman, R. B., (N,M)-Specific Absorption Cross Sections of Single-Walled Carbon Nanotubes Measured by Variance Spectroscopy. *Nano Lett* **2016**, *16*, 6903-6909.
137. Brozena, A. H.; Leeds, J. D.; Zhang, Y.; Fourkas, J. T.; Wang, Y., Controlled Defects in Semiconducting Carbon Nanotubes Promote Efficient Generation and Luminescence of Trions. *ACS Nano* **2014**, *8*, 4239-4247.
138. Murakami, Y.; Lu, B.; Kazaoui, S.; Minami, N.; Okubo, T.; Maruyama, S., Photoluminescence Sidebands of Carbon Nanotubes Below the Bright Singlet Excitonic Levels. *Phys Rev B* **2009**, *79*, 5.
139. Harutyunyan, H.; Gokus, T.; Green, A. A.; Hersam, M. C.; Allegrini, M.; Hartschuh, A., Defect-Induced Photoluminescence from Dark Excitonic States in Individual Single-Walled Carbon Nanotubes. *Nano Lett* **2009**, *9*, 2010-2014.
140. Kadria-Vili, Y.; Bachilo, S. M.; Blackburn, J. L.; Weisman, R. B., Photoluminescence Side Band Spectroscopy of Individual Single Walled Carbon Nanotubes. *J Phys Chem C* **2016**, *120*, 23898-23904.
141. Giebink, N. C.; Lassiter, B. E.; Wiederrecht, G. P.; Wasielewski, M. R.; Forrest, S. R., Ideal Diode Equation for Organic Heterojunctions. Ii. The Role of Polaron Pair Recombination. *Phys Rev B* **2010**, *82*, 8.
142. Bartesaghi, D.; Perez, I. D.; Kniepert, J.; Roland, S.; Turbiez, M.; Neher, D.; Koster, L. J. A., Competition between Recombination and Extraction of Free Charges Determines the Fill Factor of Organic Solar Cells. *Nature Communications* **2015**, *6*, 10.
143. Zhou, X. J.; Park, J. Y.; Huang, S. M.; Liu, J.; McEuen, P. L., Band Structure, Phonon Scattering, and the Performance Limit of Single-Walled Carbon Nanotube Transistors. *Phys. Rev. Lett.* **2005**, *95*, 4.
144. Topinka, M. A.; Rowell, M. W.; Goldhaber-Gordon, D.; McGehee, M. D.; Hecht, D. S.; Gruner, G., Charge Transport in Interpenetrating Networks of Semiconducting and Metallic Carbon Nanotubes. *Nano Lett* **2009**, *9*, 1866-1871.